DESCRIPTION OF A PULSATILE FLOWFIELD DOWNSTREAM FROM AN ORIFICE-LIKE STENOSIS

A Dissertation

Presented to

The Faculty of the Department of Civil Engineering

The University of Houston

In Partial Fulfillment

of the Requirements for the Degree

Doctor of Philosophy

---

by

John Thomas Cox

December 1977

ACKNOWLEDGEMENTS

The author wishes to express his sincere appreciation to the following individuals and organizations whose support and assistance made possible the completion of this dissertation:

Dr. Ned H. C. Hwang for supervising the research and reviewing the manuscript.

Dr. James van Hoften for turbulence data analysis advice and patient review of each manuscript revision.

Dr. A. K. M. F. Hussain for his advice and consultation concerning vortex shedding under pulsatile flow conditions.

Mr. Louis Feldmen for machining the orifice modules and fabricating several mock circulation loop components.

Laboratory Technicians Ben Dunn, Ralph King, and Murphy Pickard for their assistance in assembling, modifying, and operating the data collection equipment.

Miss Connie Turner and Miss Sandra Lewis for patience and perserverance in transforming the many handwritten pages into the final typed copy and its several revisions.

Mr. Stephen G. Van Horn for preparing the plot formats and illustrations used in the final manuscript.

Wife, Mary Lu, for her continuous patience, encouragement, and understanding throughout the research; and her assistance in collecting and reducing the raw data.

Children, Lisa Ann and Juli Lynn, for their patience and understanding.

University of Houston, Department of Civil Engineering, and the Baylor College of Medicine Department of Surgery for providing equipment and laboratory space.

The Flight Operations Directorate and the Data Systems and Analysis Directorate of the National Aeronautics and Space Administration for financial assistance, encouragement, and computational services.

Portions of this research were supported by the United States Public Health Service Grant HE-01330 and North Atlantic Treaty Organization Scientific Affairs Division Grant RG734.

DESCRIPTION OF A PULSATILE FLOWFIELD
DOWNSTREAM FROM AN ORIFICE-LIKE STENOSIS

An Abstract

Presented to

The Facility of the Department of Civil Engineering

The University of Houston

In Partial Fulfillment

of the Requirements for Degree

Doctor of Philosophy

---

by

John Thomas Cox

December 1977

ABSTRACT

The mechanisms of generation and propagation of acoustic murmurs in the cardiovascular system are studied in an in-vitro, bench-top model using a confined pulsatile jet. The stenosis geometry suggested by the isthmic form of coarctation of the aorta has been modeled to examine the distal flowfield velocity profiles. Excised coarctation segments and corresponding pre-operative aortograms were carefully examined to develop the flow model. The aortograms recorded under physiological pressures indicated the presence of a small jet that persisted through systole and diastole. Several model stenoses were constructed from clear plastic. Clear water at room temperature was propelled through the models with a pneumatically driven pulsatile pump. Comparisons were also made to steady flow. Quasi-steady state conditions were maintained throughout each of the pulsatile experiment runs. Observations were made for both the systolic and diastolic phases. During systole a jet develops which grows and decays in a manner similar to steady flow predictions. Frequency analysis shows that the Strouhal number predictions for orifice flow are valid for the quasi-steady state systolic flow. This relationship suggests a non-invasive technique which may be used to determine stenosis size and mean velocity.

TABLE OF CONTENTS

Page

LIST OF TABLES

LIST OF FIGURES

LIST OF SYMBOLS

A	Cross-Sectional Area
C	Orifice Coefficient
d	Diameter
D^*	Characteristic Length
E	Energy
E_1	Euler Number
f	Frequency
F	Body Force
g	Gravitational Acceleration
G	Correlation Function
i,j,k	Unit Vectors
h	Height in a Gravitational Field
J	Momentum Flux
K	Constant
l	Liter
n	Nikuradse's Constant
p	Pressure
Q	Volumetric Rate of Flow
r	Measurement in Radial Direction
R	Tube Radius
R_e	Reynolds' Number
S	Strouhal Number
t	Time
u	Velocity in Longitudinal Direction
v^*	Friction Velocity

x Cartesian Component in Longitudinal Direction i

y Cartesian Component Perpendicular to x in Direction j

z Cartesian Component Perpendicular to x and y in Direction k

α Frequency Parameter

γ Specific Weight

δ Boundary Layer Thickness

ξ Vorticity

λ Friction Coefficient

λ_s Small Scale of Turbulence

μ Dynamic Viscosity

ν Kinematic Viscosity

ρ Density

τ Shear Rate

ω Angular Frequency

THE PROBLEM AND THE MODEL

1.1 Introduction

The bounded pulsatile jet is a flow condition that is present in many practical engineering applications. It commonly occurs in the flow passages of reciprocating engines, pumps and compressor systems. It may also be present in the diseased human cardiovascular system. In each of these cases fluid is passed through an inline obstruction such as a valve or orifice. Mathematical analyses of these flow conditions is very difficult because of the nonlinearity of the governing equations. Exact solutions have only been developed for the steady, submerged axisymmetric and planar jets (Schlichting, 1968). Empirical relationships have been developed for steady confined orifice flows which relate orifice geometry, pressure tap locations and fluid flowrate (Ture and Sprenkle, 1935; and Lea, 1938).

The bounded pulsatile jet brings together several classical fluid mechanical flow cases which simultaneously interact with each other. These cases are submerged jet flow, orifice flow and oscillating and steady pipe flow. These flows may be either laminar or turbulent.
The steady orifice or jet flows can usually be characterized by a vortex shedding frequency that is related to the fluid velocity and orifice geometry.

This work examines the bounded pulsatile jet by relating model observations to classical steady flow observations and analyses. The model selected is a physiological flow obstruction or stenosis. A stenosis is any stricture or narrowing of a flow passageway. The particular stenosis of aortic coarctation was selected for modeling because of its normally well behaved geometry.

Over the years physicists and engineers have accumulated knowledge of fluid flow in pipes, orifices and jets. On the other hand, physiologists and clinicians have observed and described blood flow conditions in the human cardiovascular system. Certain similarities have been identified between the engineering pipe-flow problems and cardiovascular blood flow anomalies. Attempts have been made in recent years to relate certain pathological findings of the clinician to the theory and empirical experiences of the engineering disciplines. A class of problems of interest to both the clinician and the engineer concerns the flow through an obstruction. In physiological systems, this type of flow may occur downstream from diseased heart valves, arterial bifurcations and stenoses of arterial or valvular origin. Fluid flow mechanisms have been invoked to describe normal and abnormal blood flow conditions and to assist in development of techniques to diagnose vascular flow anomalies. These mechanisms have also been blamed for or related to murmur production, post-stenotic dilatation, aneurysm development, and atherosclerotic deposition.

The isthmic form of coarctation of the aorta, a congenital vascular disease, represents a typical subset of obstructed flow cases which readily lends itself to physical modeling. The fluid flow field suggested by coarctation of the aorta has been reproduced in an in-vitro, bench-top model for detailed flow investigation. In the present work, experiments were conducted on the modeled obstruction by reproducing pulsatile fluid flow through the model which was placed in a mock circulation loop. This investigation seeks to examine the case of a strong pulsatile jet confined in a pipe. The flow which develops downstream from the modeled obstruction is spatially and temporarily described. It is expected that the experimental results may suggest a method for predicting the degree of obstruction and the accompanying flow rate using noninvasive techniques. It is hoped that the flow mechanisms described herein will be of use as the basis for understanding several engineering and cardiovascular obstructed pulsatile flow conditions. It is also hoped that these described mechanisms will be useful in providing fundamental information for the development of new noninvasive techniques which can be used for qualitative and/or quantitative diagnosis of many valvular and stenotic cardiovascular anomalies.

1.2 Basic Physical Modeling Considerations

A properly designed physical model is a powerful tool for analyzing and understanding certain physical phenomenon in a prototype. The advantages of selecting a physical model over a mathematical or animal model are twofold: (1) direct observations can be made on the model as the control parameters are varied within desirable ranges and (2) experiments can be reproduced under exact conditions at any desirable duration and frequency. In all modeling cases, it is important to remember the fact that a model can never be made to reproduce exactly all of the functions of the prototype, thus the information obtained from the model study is limited by the assumptions and restrictions involved in the design and construction of the analog.

The selection of model parameters is the most critical phase in the model design. As a common "rule of thumb", a model is best designed to study one particular phenomenon of the prototype. A second model may likely be needed for investigating a different or secondary phenomenon in the same prototype.

The phenomenon investigated in this work is the flow field produced by a strong pulsatile jet issuing from an orifice in a confined pipe flow. This flow condition has been suggested by a range of documented vascular diseases, but it is found to be most closely related to the isthmic form of coarctation of the aorta.

1.3 Selection of the Experimental Model

Model selection involves careful consideration of the advantages and disadvantages of using various model types. The models applicable for this type of investigation may include animal models, mathematical models and physical, in-vitro models. Animal models have the advantages of providing the entire intact circulation system and are readily available to provide the proper fluid and material characteristics for physiological analogy. The disadvantages are that parameters such as pulse rate, obstruction diameter, pulse wave shape, measurement probe location, vessel geometry, vascular resistance and compliance cannot be accurately determined or controlled from one run to the next on the same animal or from one animal to the next. To accurately describe the bounded pulsatile jet, it is important that these parameters are well known and controlled, hence the animal model was discarded.

Mathematical models have the advantage that each parameter discussed above can be controlled exactly and the model can be examined over a wide range of operating conditions which apply to the cardiovascular as well as the engineering cases. The disadvantages are that the governing equations are highly nonlinear and require many limiting assumptions to obtain solutions. Yellin (1966) and Womerseley (1955b) have examined pulsatile flow. Macagno and Hung (1967) and Hung (1968) have examined steady and pulsatile flow through an orifice at low (less than 2000) orifice Reynolds numbers. These solutions are informative, yet do not describe the bounded pulsatile flow considered here.

An in-vitro, bench-top, clear plastic model was selected because the parameters discussed above could easily be controlled from one run to the next and from one model size to the next. The model consisted of clear plastic square edged orifices which were placed in a mock circulation loop. Water was selected as the system fluid to permit Reynolds number variations that fell within the laminar, transition and turbulent flow regimes. The flow observations would thus be informative for both the cardiovascular and the engineering applications. The disadvantages of the physical model are that limiting assumptions must be made in material selection, vessel distensibility, fluid viscosity, model shape and circulation loop response. Careful selection of the assumptions in each of these areas yields experimental results that are useful in understanding the bounded pulsatile jet.

1.3.1 Model Similarity

Physical modeling results are inevitably limited by the assumptions and the simplifications which are invoked in the design, construction, and operation of a model. The application of a model requires that certain similarity conditions be observed when the model system is designed. When these conditions are properly adhered to, model limitations can be eliminated permitting the model system to provide the information desired.

Model design must consider similarity relationships to the prototype geometry, materials, and the kinematic and dynamic behavior of the flow field. Geometry considerations involve similarity of scale and shape. For the present study a one-to-one scale was conveniently assumed and several orifice sizes were selected. Material considerations involve properties of both the testing fluid homogeneity, density and viscosity; and the model wall distensibility, response to static and dynamic loading, and wall smoothness. Water at room temperature was used as the fluid analog to provide a wide Reynolds number variation. Plexiglass pipe was chosen as the wall material since coarctation sites are relatively stiff as are most engineering flows, and distal flows exhibit relatively small pulse pressures. Kinematic and dynamic similarity is governed by the ratio of the inertia forces to the viscous forces in the model chamber. The testing fluid was propelled through the model by a pneumatically powered pump. An adjustable resistance and compliance were provided to afterload the model to simulate the systemic circulation distal to the obstruction. Preload resistance and compliance were also simulated through the pulse wave shape adjustments.

1.3.2 Geometry

Geometric similarity between the prototype and the model exists if the model ratios of all corresponding dimensions in both are equal. The human aorta is of sufficient size that conventional instrumentation can be readily applied without rescaling. Hence, a one-to-one scale factor was selected for model sizing. The human aorta actually varies in size from one individual to another. Normally the thoracic aorta diameter varies from one to three centimeters (McDonald, 1974). Hence, a typical value of 1.59 cm was selected for the experimental model. Similar sized plexiglass and tygone tubes were used in the circulation loop.

In general, arterial lesions, or stenoses, may take on a variety of cross-sectional shapes and longitudinal dimensions which are difficult to replicate. The case of coarctation of the aorta also takes on a variety of shapes, however, the variations are somewhat better behaved and are thus used as a modeling guide. Aortograms, pressure waves, and excised pathological segments from child patients (Simpson, 1972) were examined and are summarized in Figure I.1. The excised segments indicated that flow area blockages from 85% to full occlusion necessitated surgical correction. The aortograms indicated that the flow which issued from the blockage during systole resembled the pattern of a pulsatile jet. This profile is best simulated with an orifice model. The orifice simulation applies to coarctation cases as well as valvular regurgitation, vessel bifurcations, and stenotic lesions that terminate in an orifice shape on the distal side of the obstruction. Square edge orifice sizes of 11, 20, 30, and 50 percent (percent of full lumen area) were selected to systematically investigate the confined pulsatile jet behavior downstream from the blockage.

1.3.3 Materials

The material considerations involve the properties of the analog fluid used to simulate the blood, and the wall which should reproduce shape and distensibility of both the aorta and the lesion itself.

1.3.3.1 Fluid Properties

Whole blood is comprised of a relatively homogeneous plasma and a suspension of small sized deformable particles. These particles are red blood cells or erythrocytes (approximately 8-micron diameter by 2-micron thick biconcave discs), slightly larger white blood cells or leukocytes (approximately 8-micron to 16-micron diameter), and smaller platelets and thrombocytes. Typically, these particles track the flow of the plasma and are much smaller in size than the smallest scale

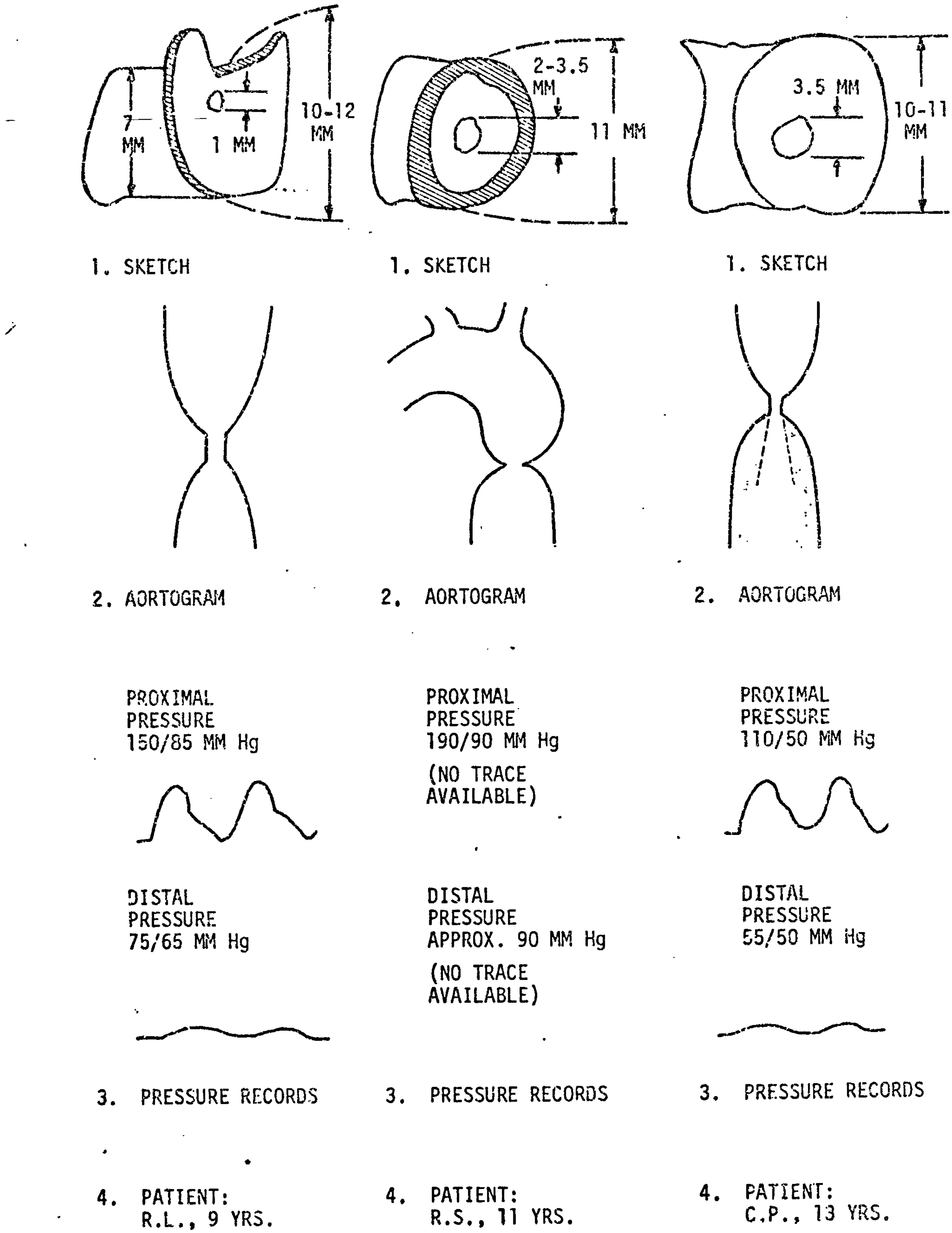

FIGURE I.1 AORTIC COARCTATION PATIENT RECORDS (SIMPSON, 1972) eddies observed in turbulent blood flow (Hussain, 1977). Therefore, it is justified to assume that blood behaves as a homogeneous fluid for the flow dynamics being considered.

Viscosity is a measure of flow resistance exhibited by a fluid as a function of an applied force or pressure gradient. A fluid is said to be Newtonian if the absolute or dynamic viscosity, μ, is a proportionality constant between the shear stress, τ, and shear rate, $\partial u/\partial y$, where u is the longitudinal velocity and y is a coordinate perpendicular to the flow. Kinematic viscosity, ν, is the ratio of the dynamic vicosity to the fluid density, ρ. The fluid viscosity has the effect of adjusting the relationship between the inertia forces and viscous forces in the flow. Bounded pulsatile flows could involve: fluids with very low viscosities, such as air and other gases; liquids of moderate viscosities, such as light petrochemical products and water; and finally fluids of larger viscosities, such as blood, oil and other heavier petrochemical products. The flow similarity parameter of interest is the Reynolds number, which is the ratio of the inertia forces to the viscous forces. Fluid flow regimes in pipes have been defined for steady flow to be laminar, transitional and turbulent. Laminar flow regimes are generally considered to include steady flow Reynolds number values below 2000-2300. Fully turbulent flows are generally characterized by Reynolds number values above 7000-7500. The range of flows between these regions is considered to be transitional. Since it is desired to develop bounded pulsatile jet descriptions that are useful in understanding both the engineering flows and the physiological flows; water, a fluid of moderate viscosity, has been selected. The pulsatile behavior of the flow and the Reynolds number comparison to the physiological case are considered later when kinematic and dynamic similarity conditions are examined.

Blood viscosity increases linearly with hematocrit up to the value of 45-50% normally reported in humans. Beyond this, it increases in a nonlinear manner. Kinematic viscosity values for humans have been reported over a range of 2 to 6 times that of water. Usually accepted values are approximately 0.7×10^{-2} stokes for water and 4.0×10^{-2} stokes for whole blood (McDonald, 1974). Basically, whole blood is non-Newtonian at low shear rates where μ has little meaning. However, in large arterial flow with relatively high shear rates, blood behaves in a Newtonian manner (Merril and Pelletier, 1967). The expected maximum wall shear rates are from 500 to 10,000 sec^{-1} for the cases to be considered. Merril and Pelletier showed that blood behaves in a transition manner between shear rates of 20 and 100 sec^{-1}. Below shear rates of 20 sec^{-1} the Casson relationship is used to relate shear stress to strain rate. The Casson expression adds a blood yield stress term to the linear Newtonian shear stress to strain rate relationship. Above 100 sec^{-1} a Newtonian relationship exists.

1.3.3.2 Wall Properties

The properties of elastin in the circumferential direction of the aorta wall stores portions of the ejection energy as potential energy and releases it to the blood during diastole to move the blood continuously in a downstream direction. After the arterial system has branched several times, the distensibility, which is a function of the amount of elastin in the arterial wall, decreases and the arterial walls are then characterized by more rigid smooth muscle.

Distension during a cardiac cycle occurs as a function of fluid pressure exerted on the vessel walls. A sudden variation in the wall geometry changes the longitudinal pressure distribution in the vessel. For severe aortic stenoses very little pulse pressure can be observed downstream of the obstruction. It is thus assumed that the effect of pulsation on vessel distension is small and insignificant in this study.

Typically, arterial stenoses are built up of layers of deposited materials or result from vessel wall fabric thickening from various causes. These layering or thickening conditions tend to reduce the vessel lumen, thicken the walls and greatly decrease the lesion distensibility. Excised coarctation specimens were also found to be thick and fairly rigid compared to surrounding vascular tissue. It therefore is concluded that the orifice model can also be constructed of a rigid material with little loss of fluid flow accuracy.

1.3.4 Flowfield Similarity

Flowfield similarity is achieved by relating kinematic and dynamic fluid motion. To obtain kinematic similitude the fluid must move in geometrically similar paths and the fluid velocity ratios must be equal. To achieve dynamic similitude, the ratios of the acting forces must be kept equal to that of the prototype. These considerations are examined below.

1.3.4.1 Kinematic Relationships

The geometric relations concerning modeling of obstruction size and tube diameter have been discussed earlier and a one-to-one model scale factor was selected. Stenotic lesions may be located along any major artery in the arterial tree. Most commonly atherosclerotic lesions are found at bifurcations, branches, and bends (Schwartz and Michell, 1962;

Brech and Bellhouse, 1973; Roach, 1977). The isthmic form of coarctation of the aorta is usually located distal to the left subclavian artery. Flow through the obstruction usually enters a relatively straight section of aorta. Lower thoracic and abdominal coarctations are also found located in relatively straight aorta sections (Onat and Zeren, 1969; Riemenschneider et al, 1969) It therefore is concluded that straight tubes may be used with small flow impact. If the pulsatile jet spreads and dissipates rapidly, then the straight tube assumption may also be extended to bifurcation cases and stenoses where relatively straight short arterial segments persist beyond the blockage.

Kinematic similarity must also consider the velocity ratios at different flow locations. Blood velocities through various lesions are usually reported in terms of volumetric flow rate such as liters per minute. Flow rates may vary from zero to two or three liters per minute depending upon the location of the arterial branch exhibiting the blockage and the size of the obstruction. Lauridsen (1968) reported coarctation flow rates from 0 to 2.76 liters/minute in thirteen cases of aortic coarctation prior to surgical correction using an electromagnetic flow meter. Flow rates from one to four liters/minute were selected for use in the present study. These flowrates assure Reynolds numbers below, in and above the transition region which are of interest to both the clincian and the engineer.

1.3.4.2 Dynamic Relationships

Dynamic considerations involve similarity relationships between forces and force gradients present in the prototype and in the model. The gravitational force can be ignored because of its small magnitude compared to the other forces (gravity approximately one order or magnitude smaller). The effects of elasticity have already been discussed for the vessel and lesion site. It was concluded that downstream from the blockage the distensibility effects are small because of the thickened vessel wall and the small pulse pressure amplitude which persists distal to the stenosis.

Fluid elasticity or compressibility may be neglected since the speed of sound in blood is two orders of magnititude higher than the blood velocities being examined. Blood flow in arteries exhibits little or no compressibility variations and does exhibit a relatively high modulus of elasticity.

The pressure forces are compared by use of the Euler number E_1, defined as

$$E_1 = \frac{\rho \bar{u}^2}{p} \qquad (1.1)$$

where $\bar{u}$ is average fluid velocity and p is local fluid pressure. Since the density variation between blood and water is on the order of 10%, with blood having the greater density, the Euler number variations indicates that the inertia forces in the model will be approximately 10% less than in the prototype compared to the pressure forces. For the mean pressures obtained from Karnal (1968) variations of this size (5-10 mmHg) are well within one standard deviation of 33 pre- and post-erativive cases of aortic coarctation.

The inertia and viscous forces are related by their ratio, the Reynolds number, defined as

$$R_e = \frac{\rho \bar{u} D^*}{\mu} \qquad (1.2)$$

where D* is a characteristic dimension. For flow through pipes, orifices or arteries, this value is taken as the lumen diameter. Previous discussion has shown that the density, velocity, and diameter values are similar between prototype and model. The difference in viscosity between whole blood and water will yield a model Reynolds number approximately four times greater than the prototype. This difference is reconciled in two ways: (1) the phenomenon being investigated is that of a strong pulsatile jet in a confined pipe flow and as such has not been modeled after a specific engineering flow condition or a select case of vascular disease and (2) the range of orifice sizes used in the investigation will provide some Reynolds number flows which are applicable to vascular and engineering flows. Actual vascular flow cases may later be analyzed based upon the techniques developed in the present work.

Aortic Reynolds numbers have been reported up to 15,000 (McDonald, 1974; Lighthill, 1972, 1974; Rushmur, 1970). For selected flow rates of 1 to 4 liters/min through the range of orifice sizes selected, the Reynolds number (based upon orifice diameter) upper limit was found to be between 15,000 and 18,000. Reynolds numbers below the critical Reynolds number, approximately 2300, were also produced. The critical Reynolds number is the threshold below which the fluid flow is described as parallel and viscous forces are significant. It was, therefore, concluded that water serves as a suitable fluid for the investigation,however, if particular vascular flow anomalies are to be explored later, based upon this work, then corresponding fluid viscosity adjustments must be considered.

Dynamic similarity is complete if the periodic pressure wave produced in the model is related to the prototype wave by the frequency parameter, α, defined as

$$\alpha = r\sqrt{\frac{\omega}{\nu}} \tag{1.3}$$

where ω is the angular pulsation frequency and r is vessel radius. Since α does not include terms which define the shape of the wave, similarity is not guaranteed. The best similarity check is performed by simultaneously monitoring the pressure wave form and comparing and adjusting it to agree with published profiles representative of prototype lesions. Values for α have been reported by Clark (1967). Human ranges vary from 13.35 to 16.7. For the geometry and fluid selected, the frequency parameter, α, ranges from 6.5 to 16.8 based upon orifice radius and equal to 23.8 based upon tube radius at a pulse rate of once per second. These values encompass the human observations by Clark.

1.4 Problem Summary and Experimental Approach

The phenomenon of a strong pulsatile jet in a confined pipe flow has been selected for flow field investigation. Steady flow and some oscillatory flow mathematical models are available which describe selected aspects of the flow phenomena. These mathematical descriptions, to be reviewed later, are compared to the experimental flow field observations. Variations in orifice size, pulse frequency and flow rate are produced. The flow effects from these variations are described in terms of cross-sectional profiles at various flow field locations and velocity fluction frequency distributions produced by the disturbed flow. Specific experimental objectives were to:

1. Describe spatially and temporarily the pulsatile jet flow field distal to the orifice.
2. Examine the size, shape, growth, and decay of the pulsatile jet.
3. Describe flow field variations resulting from changes in orifice size and pulse frequency and magnitude.
4. Compare pulsatile flow observations to steady flow measurements obtained from with the same model.
5. Describe velocity fluctuation frequency variations which result from changes in orifice size, flow rate, and measurement location.

CHAPTER II

THE BACKGROUND PHYSIOLOGY AND FLUID MECHANISMS

2.1 Background

Arterial stenoses are usually related to the presence of disturbed pulsatile blood flow (Roach, 1977; Kline et al, 1962). Flow disturbances were found to be exaggerated during systole and relaxed during disatole. Audible murmurs are often present and are usually related to the apparent turbulence or flow disturbance found distal to the blockage. The arterial stenoses may exist at a multitude of sites along the trunk and major branches of the cardiovascular tree. Symptoms produced are usually undetected until the disease has progressed to an advanced stage, approximately 85% area occlusion or greater (Berguer and Hwang, 1974). The symptoms are usually related to the organs downstream from the obstruction. Several fluid flow mathematical models have been developed over the years which describe and predict flow conditions that may be relevant to the pathological conditions. Their review aids in developing a better understanding of the patho-physiological problem and the model limitation

2.2 Arterial Stenoses

Stenoses are usually found in the high flow rate sections of the major arteries and at or near the origin of the first or second generation branches off of the aorta. They may result from congenital defects or from athrogeneses. If the degree of blockage is sufficient, the resulting problem is manifested by insufficient blood supplied to organs distal to the obstruction and usually hypertensive conditions proximal to the blockage. The stenoses are classified by location and common symptom groups. Often they produce audible mumurs commonly believed to be indicative of the disturbed flow.

Stenoses of athrogenic origin are characterized by intimal and subintimal thickening and lipid deposition on the arterial wall. If the formation is severe, deformation and fragmentation of the elastic membrane may occur along with fibrosis and calcification (Galambos, 1966). Stenoses may also have congenital origins such as the lesion found in the isthmic form of coarctation of the aorta which is characterized by a deformity involving a constriction or folding of the anterior, superior and posterior walls of the aorta (Eliot and Edwards, 1966). Coarctation may occur well beyond the arch along the thoracic aorta. Classification is generally concerned with the presence or absence of a patent ductus arteriosis and position along the aorta.

Stenoses are generally classified by their relative location along the aorta (Olson, 1966). Arch stenoses may include obstructions near the brachiocephalic, left common carotid or left subclavean arteries and are usually short or segmented in character. Arch stenoses may also occur at the vertebrals from the subclavian origins. Abdominal stenoses occur along the aorta or in the primary branches and are classified as to whether their location results in renal hypertension. Terminal abdominal stenoses are classified by the arteries that they occlude: illiac, femoral, or popliteal. They are generally more perfuse and are not well described by pulsatile jet flow, however, certain dimensions and obstruction exit conditions could be related to the present work.

If the stenosis is relatively large and occurs along the aorta, several common symptoms occur. These include an unusually high upper-body blood pressure accompanied by a very low pulse pressure taken below the blockage (often taken at the femoral artery, as in aortic coarctation diagnosis). The patient may exhibit headaches, left heart hypertrophy, cerebral hemorage, aortic aneurysms, and mid to late systolic murmurs. Patient complaints are usually related to the reduced blood flow to regions beyond the blockage unless sufficient collateral circulation has developed to resupply the restricted areas.

Stenoses and coarctations, if severe enough, are corrected surgically by either resectioning the affected site or by inserting dacron grafts in an end-to-end anastemosis (DeBakey, 1966; Noon, 1977). Stenosis surgery at infancy is usually the result of a coarctation. It is avoided or delayed to late childhood, if at all possible, to improve the recovery potential and to avoid a repeated surgery at adulthood resulting from the restricted flow from the infant sized graft.

Murmurs accompany most of the severe stenoses occurring along the aorta. They are described as consisting of either turbulant noise or of related frequency sounds as indicated by such descriptors as high pitched, musical, rumbling, coarse, etc. Burns (1959), Fruehan (1962), and Delman (1967) have suggested that eddy formation or vortex shedding might be related to the musical type of murmurs and might be the general mechanism in most murmurs. Yellin (1966) combined the techniques of flow visualization and phonocardiography to investigate the genesis of murmurs under controlled steady state conditions of wall turbulence and free turbulence in a bounded jet. He showed that wall turbulence is an inefficient source of acoustic energy, while the jet-induced free turbulence was able to vibrate the surrounding tissues and act as an acoustic generator in addition to the orifice-shed vortices.

Murmur classification is difficult because it relies upon the experience of the clinician to consistently classify the findings. Murmurs are usually classified by the (1) timing and duration as related to the cardiac cycle; (2) intensity and intensity variations; and (3) pitch, quality, and location of measurement of maximum intensity. The intensity is often reported as one of six possible Levine and Harvy Grades (von Basch, 1904-1905). Grade I is the faintest sound detectable and Grade IV is of sufficient intensity to be detected just off of the chest wall. The shape of the phonocardiogram tracing is also used as a descripter. Terms such as crescendo, decrescendo, crescendo/decrescendo or diamond shaped are often used to describe the shape of the phonocardiogram tracing. A typical description of the murmur of coarctation of the aorta might be a Grade II midsystolic murmur with a harsh or rumbling quality.

2.3 Fluid Mechanics Considerations

Several aspects of fluid motion should be considered to better understand and interpret the data resulting from the model experiment. The differential equations which describe the continuity of the fluid motion, the energy balance, and the conservation of momentum together with the appropriate boundary conditions, will adequately specify any fluid flow problem. Generally closed form solutions to most of the pulsatile flow situations cannot be obtained because of the nonlinearity of the governing equations and the general complexity of the boundary conditions. Usually, to obtain a mathematical closed form solution, simplifying assumptions must be made. As in the physical model case, these assumptions limit the universal application of the results. Turbulent flow, turbed flow which is neither laminar nor fully turbulent, and confined pulsatile jet flow are particularly difficult flow situations. Relationships, familiar to the fluid mechanician, which are applicable to the present work are reviewed below.

2.3.1 General Observations

The expected experimental Reynolds number variations range from just within the laminar region (Reynolds number approximately less than 2300 based on tube diameter) to well into the turbulent region (Reynolds number in excess of 7000 for pipe flow as found by Attinger et al, 1966). For flow to be characterized as laminar or turbulent, the flow must be steady and fully developed. Blood flow in the major arteries is obviously unsteady. For steady flow to be described as fully developed, the fluid must travel 150 pipe diameters (R_e = 5000) for laminar flow inlet conditions and from 50 to 100 diameters for turbulent flow entry conditions (Schlichting, 1965). Kuchar and Ostrach (1966) determined that the elastic entrance length may be nearly an order of magnitude smaller for pulsatile flow in elastic tubes. Since stenoses generally occur at either bifrications or valves, it is clear that flow conditions to be considered will exhibit wall entrance affects and still cannot be described as fully developed.

2.3.2 The Basic Mathematical Model of Free Fluid Motion

The continuity relationship specifies that there is a balance between the mass entering, leaving, and changing in a control volume per increment of time. If the density is constant then the fluid is incompressible. The continuity equation can be written as the divergence of the velocity vector specifying no increase or decrease in mass per unit time. It is expressed as the dot product of the del operator and the velocity vector:

$$\nabla \cdot \bar{U} = \frac{\partial u}{\partial x} + \frac{\partial v}{\partial y} + \frac{\partial w}{\partial z} = 0 \qquad (2.1)$$

where x, y, and z are coordinates in the $\hat{i}$, $\hat{j}$, and $\hat{k}$ directions and u, v, and w are the velocity components in the $\hat{i}$, $\hat{j}$, and $\hat{k}$ directions.

The equations of motion are derived from Newton's second law which states that the sum of the external forces is equal to the rate of change of momentum. The external forces of interest in fluid motion are those caused by gravity, pressure, and friction. The equation of motion can be thought of as a balance between the local and convective change of momentum in the fluid as brought on by the effects of pressure and friction surface forces and the gravitational body force. For fluid at rest, the normal surface forces are found to be the result of the applied pressure. For fluid in motion, the friction surface forces or stresses are found to be related to the rates of strain of the fluid motion. Stokes, 1845, assumed a linear or Hooke type of relationship between the stresses and strain rate. If an incompressible fluid is assumed, then the governing equations of motion for an incompressible fluid are written as the celebrated Navier - Stokes equation

$$\frac{Du_i}{Dt} = F_i - \frac{1}{\rho}\frac{\partial p}{\partial x_i} + \upsilon \frac{\partial^2 u_i}{\partial x_j \partial x_j} \qquad (2.2)$$

where D/Dt is the substantive derivative, F_i, is the gravitational or body force and the subscripts i and j refer to tensor notation (repeated subscripts imply summation). If the fluid is assumed to be ideal (no viscosity), then the right hand term can be dropped and the resulting equation referred to as as Euler's equations of motion for a nonviscous fluid. Steady laminar flow problems are not the usual fluid flow cases encountered in pipe flow or arterial blood flow. The other end of the flow spectrum considers fully developed turbulent flow. The Navier-Stokes equations can be invoked as an analysis starting point if fluctuation components are included in u, v, w, and p. The fluctuation components can be viewed as being composed of both organized and random components (see Figure II.1):

$$u = \bar{u} + u' + \tilde{u}, \tag{2.3}$$

$$v = \bar{v} + v' + \tilde{v} \tag{2.4}$$

$$w = \bar{w} + w' + \tilde{w} \tag{2.5}$$

$$p = \bar{p} + p' + \tilde{p} \tag{2.6}$$

where the (') notation implies random turbulent contribution and ($\sim$) implies periodic disturbance contribution. These quantities, when substituted into equation 2.2 and time and phase averaged, as described by Hussain (1977), yield a new set of equations of motion for turbulent flow as

$$\frac{Du_i}{Dt} = F - \frac{1}{\rho}\frac{\partial p}{\partial x_i} + \nu \frac{\partial^2 u_i}{\partial x_j \partial x_j} - \frac{\partial}{\partial x_j}\left(\overline{u_i' u_j'}\right) - \frac{\partial}{\partial x_j}\left(\widetilde{\tilde{u}_i \tilde{u}_j}\right), \tag{2.7}$$

where the $\overline{u_i' u_j'}$ term is the familiar Reynolds stresses resulting from fluctuating turbulent motion and the $\overline{\tilde{u}_i \tilde{u}_j}$ terms represent the modification of the flow field from the induced periodic motion. Time averages are taken over large time intervals and phase averages are taken over identical ensemble portions of each repeating periodic pulse. The time period for phase averaging is sufficient if it is much larger than the integral or time scale of the largest eddies in a stationary flow. In practice this is determined by showing that the average values remain unchanged over large time intervals. The utility of the tensor notation is evident since the new random motion and periodic terms are quite complex, commposed of nine components each.

The Bernoulli form of the energy equation is obtained by integrating each term of the equation of motion and summing the respective components. If incompressible steady flow of an ideal fluid is assumed, then the resulting energy equation takes the familiar Bernoulli form

$$\frac{P}{\gamma} + \frac{u^2}{2g} + h = \text{Constant}, \tag{2.8}$$

where γ is the specific weight, g is the gravitational acceleration and h is height or elevation in the gravitational field.

2.3.3 Boundary Effects

When equations 2.2 or 2.7 are examined for a specific flow condition, the effects of confining boundaries need to be considered. These vary according to the presence of laminar or turbulent motion, entrance effects, and oscillatory or moving walls. Blood flow is significantly

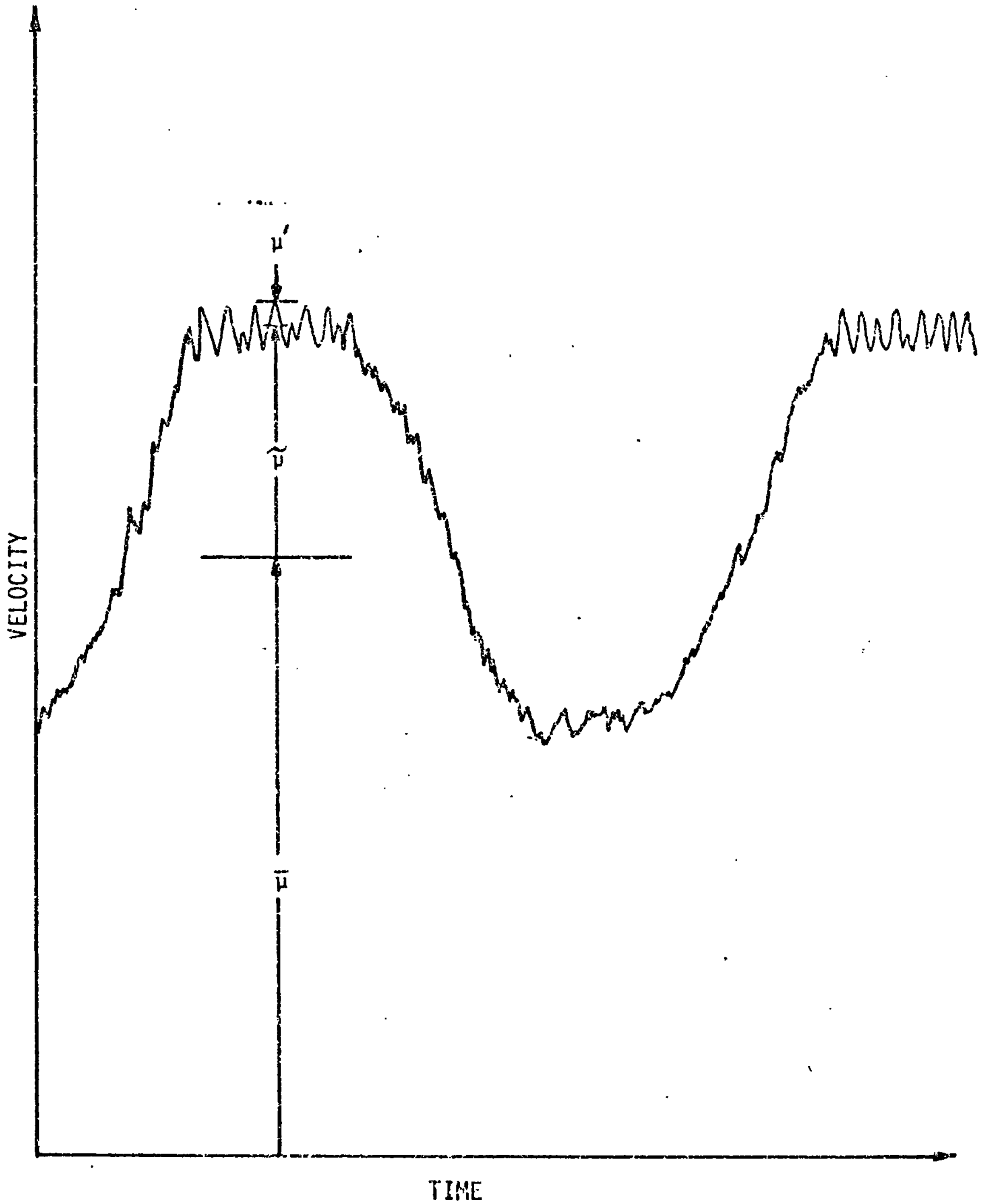

FIGURE II.1 VELOCITY HISTORY DECOMPOSED INTO MEAN, $\bar{\mu}$; PERIODIC, $\tilde{\mu}$; AND RANDOM, μ′ COMPONENTS.

influenced by the confining arterial boundaries. Nearly all arterial flows exhibit strong entrance effects, oscillating fluid motion, disturbance production and dissipation. These boundary effects can be appreciated by examining a few classical boundary treatments for laminar flow plus looking at differences that occur because of the presence of turbulence. The boundary effect discussions are concerned with the "no slip condition" present at the wall. It specifies that fluid particles at the wall do not move with the flow. This causes a velocity gradient and corresponding shear stress resulting from the fluid viscosity.

The boundary layer is the region in the fluid adjacent to the boundary where the fluid velocity is reduced from the free stream value to the zero velocity at the wall. The boundary layer is characterized by the production of vorticity brought upon by viscous shearing. It is also characterized by the reduction of momentum. Vorticity, ξ, is defined as the curl of velocity. The rate of vorticity production is found by taking the curl of the momentum equation 2.2 and thus obtaining the vorticity transport equation,

$$\frac{D\xi}{Dt} = \xi_i \frac{\partial u_i}{\partial x_j} + \nu \frac{\partial^2 \xi}{\partial x_j \partial x_j} \qquad (2.9)$$

The first term on the right hand side shows the vorticity changes which result from eddy tilting and stretching brought about by directional velocity gradients acting upon vorticity already present in the flow. The second term on the right hand side is the vorticity production or dissipation through viscous friction.

When fluid enters a pipe or meets a flat sharp edged plate parallel to the initial fluid direction, the boundary layer effects can be visualized. The particles along the surface remain stationary. Near the leading edge, viscous shear is present and each particle tends to reduce the velocity of the particle adjacent to it. The boundary layer grows in this manner along the length of the pipe or sharp plate. At sufficiently high Reynolds numbers, a transition region is reached where the fluid begins to breakup into a disorganized motion. The transition region occurs downstream from the leading edge. The distance to the transition point is a function of the free flow Reynolds number. Still further downstream fully turbulent flow develops in the boundary layer away from the wall. However, in the immediate vicinity of the wall, the laminar or viscous effects are still present in a laminar sublayer. Beyond this thin region, the fluid may be treated as inviscid.

Closed form solutions to the Navier - Stokes equations are available for parallel flow in a pipe, flow starting at a wall or in a pipe, and flow near an oscillating plate. Some exact solutions obtained either empirically or numerically are also available for the circular jet and for oscillating flow in a pipe.

2.3.3.1 Parallel Flow

Parallel flow assumes that steady fluid motion only occurs in one direction. Motion in the other two orthogonal directions are identically equal to zero. This also implies that the pressure gradient is only present along the flow direction. For steady flow between two parallel walls (Couette flow), equation 2.2 is reduced to

$$\frac{dp}{dx} = \mu \frac{d^2u}{dy^2} \quad , \qquad (2.10)$$

with the accompanying boundary conditions that the velocity is zero at the walls ($\pm$ b). The pressure gradient is constant if the flow is steady and no velocity is present in the y and z directions. Therefore the solution,

$$u = -\frac{1}{2\mu}\frac{dp}{dx}\left(b^2 - y^2\right), \tag{2.10}$$

is seen as a parabolic velocity profile which reaches a peak at the center of the stream where b = 0.

In a similar manner, parallel pipe flow was examined by Hagen (1839) and Poiseuille (1840), a physiologist. The flow axis is taken as the center line of the pipe and the velocity is zero along the pipe wall (r = R). Also, velocity gradients in the radial direction are assumed equal to zero (steady parallel flow). The Navier-Stokes equations in cylindrical coordinates are reduced to

$$\frac{dp}{dx} = \mu\left(\frac{d^2u}{dr^2} + \frac{1}{r}\frac{du}{dr}\right), \tag{2.12}$$

where x is the coordinate direction along the pipe axis and r is the radial direction. The solution is

$$u(r) = -\frac{1}{4\mu}\frac{dp}{dx}\left(R^2 - r^2\right). \tag{2.13}$$

This again indicates that parallel flow is represented by a parabolic profile (parabolid of revolution). The velocity is linearly related to the constant pressure gradient. In addition, the velocity varies inversely with the product of pipe length and viscosity which is thus considered as a resistance term.

2.3.3.2 Flow at a Wall Started from Rest

Stokes (1901) examined flow at a wall which is suddenly started from rest and moves at a constant velocity U_0. At time zero there are no velocity components in the fluid. After time zero, the wall moves, with the no slip condition, at a constant velocity equal to U_0. At an infinite distance from the wall, all velocity components are equal to zero. For this case, the Navier-Stokes equations reduce to

$$\frac{du}{dt} = \upsilon \frac{d^2 u}{dy^2} \quad . \tag{2.14}$$

Equation 2.14 is reduced to an ordinary differential equation by substituting

$$\eta = \frac{y}{2\sqrt{\upsilon t}} \quad . \tag{2.15}$$

The solution is then found to be

$$u = V_o \operatorname{erfc} \eta \ . \tag{2.16}$$

The boundary layer velocity is equal to 99% of the free stream velocity at a thickness, δ, where

$$\delta = 4\sqrt{\upsilon t} \quad . \tag{2.17}$$

Therefore, the boundary layer thickness grows as the one-half power of time, t, from which the fluid was exposed to the constant motion.

2.3.3.3 Flow in a Pipe Started from Rest

Symanski (1932) examined a similar problem for flow started in a pipe. All fluid is at rest at time zero. After time zero, a constant pressure gradient is applied along the pipe axis. The no slip condition applies at the walls. The Navier-Stokes equation reduces to equation 2.12 with the addition of a $\partial u/\partial t$ term. The solution takes the form of Bessel equations which show a relatively flat initial profile which asymptotically approaches the parabolic profile found in equation 2.13.

2.3.3.4 Flow at an Oscillating Wall

Stokes (1901) also examined the boundary flow next to an oscillating plate. Again the Navier-Stokes equations reduce to equation 2.14. Assuming that the plate motion is described as

$$u(o,t) = V_o \cos \omega t, \tag{2.18}$$

then the solution to equation 2.14 is

$$u(y,t) = V_o \, e^{-y\sqrt{\frac{\omega}{2\nu}}} \cos\left(nt - y\sqrt{\frac{\omega}{2\nu}}\right). \tag{2.19}$$

The exponential term shows that the velocity is damped with y, or distance from the plate, and that the fluid away from the plate has a phase lag $y\sqrt{\omega/2\nu}$ behind the wall motion. The boundary layer thickness is found to vary as

$$\delta \simeq \sqrt{\frac{\nu}{\omega}} \,. \tag{2.20}$$

This shows that thickness and kinematic viscosity vary in the same direction, while increased frequency results in a thinner boundary layer.

2.3.3.5 Oscillating Flow in a Pipe

Oscillatory flow in pipes has been examined by Sexl (1930) and Uchida (1956). The solution has been developed in a similar manner by Womerseley (1955b) for artery flow when the pressure gradient is known. The Navier-Stokes equation for the unsteady axial flow takes the form

$$\frac{du}{dt} = -\frac{1}{\rho}\frac{dp}{dx} + \upsilon\left(\frac{\partial^2 u}{\partial r^2} + \frac{1}{r}\frac{\partial u}{\partial r}\right). \tag{2.21}$$

The no slip condition applies at the wall and the pressure gradient is assumed as

$$-\frac{1}{\rho}\frac{dp}{dx} = K_o \operatorname{Cos} \omega t , \tag{2.22}$$

where K is a constant. If the velocity, as a function of the radial position and time is assumed to be of the form

$$u(r,t) = f(r)\, e^{i\omega t} , \tag{2.23}$$

then an equation of f (r) is obtained whose sollution takes a Bessel form as

$$u(r,t) = -i\frac{K_o}{n} e^{i\omega t}\left[1 - \frac{J_o\left(r\sqrt{-\frac{i\omega}{\upsilon}}\right)}{J_o\left(R\sqrt{-\frac{i\omega}{\upsilon}}\right)}\right] \tag{2.24}$$

where J_0 is the zero order Bessel function of the first kind. The solutions of this equation can be superimposed for several frequencies, ω, or specific ranges or values of ω can be examined. For small values of the frequency parameter, α, only the quadratic terms of the Bessel function expansion need to be retained yielding

$$u(r,t) = \frac{K_o}{4\upsilon}\left(R^2 - r^2\right) \cos \omega t \; . \tag{2.25}$$

If ω is large, then the asymptotic expansion of the Bessel function can be used which yields

$$u(r,t) = \frac{K}{n}\left\{ \sin \omega t - \sqrt{\frac{R}{r}}\; e^{-\sqrt{\frac{\omega}{2\upsilon}}(R-r)} \sin\left[\omega t - \frac{\omega}{2\upsilon}(R-r)\right]\right\} \tag{2.26}$$

From the low frequency solution, it can be seen that the flow is the typical parabolic profile for $(\omega t) = 0, 2\pi$, etc. The profile is also in phase with the pressure gradient. For the high frequency case, the phase is shifted by 90^{o} and a damping term is shown which suggests the same interpretation as with the oscillating plate, i.e., the oscillating boundary layer effect damps out faster as the frequency increases. Hwang and Chao (1974) described relationships between pressure and flowrate by examining the hydraulic transmission line equations for a distensible tube where fluid at the wall moves with the velocity of the wall. For pulsatile flow these equations also yield a Bessel function solution which is somewhat similar to the expressions above.

2.3.3.6 Turbulent Pipe Flow

The case of turbulent pipe flow is a special case. No standard closed form or truly exact solution is available. Solutions which are quite accurate over a wide range of Reynolds numbers have been developed by Prandtl (1935), Nikuradse (1932, 1933), Blasius (1913) and others (Herman, 1930; Nusselt, 1910; and Stanton, 1911). It has been observed by these investigators that turbulent flow was characterized by a mean velocity which varies as the square root of the pressure gradient. A general form was adapted to group terms into a constant that could then be empirically evaluated. The pressure gradient - velocity relation was assumed as

$$-\frac{dp}{dx} = \frac{\lambda}{4R}\rho\bar{u}^2, \qquad (2.27)$$

where λ is a constant, the coefficient of resistance to be evaluated; and $\bar{u}$ is the average velocity computed from the flow rate. Since the wall shear stress, τ_o, is

$$\tau_o = \frac{dp}{dx}\frac{R}{2}, \qquad (2.28)$$

then λ can be rewritten as

$$\lambda = \frac{8\tau_o}{\rho\bar{u}^2}. \qquad (2.29)$$

If λ is determined, then the average velocity and the pressure gradient can be evaluated. Blasius found

$$\lambda = 0.3164\, R_e^{-\frac{1}{4}} \qquad (2.30)$$

for smooth pipes and Reynolds numbers below 100,000. Prandtl had suggested a form

$$\frac{1}{\sqrt{\lambda}} \approx 2.0 \log(R_e\sqrt{\lambda}) - 0.8. \qquad (2.31)$$

White (1974), upon examining many approximation schemes, suggests

$$\lambda = 1.02(\log R_e)^{-2.5}, \qquad (2.32)$$

which is good to $\pm$ 3 percent over all turbulent Reynolds numbers. It should also be noted that λ can be approximated for laminar flow even though the general relationship between velocity and pressure gradient is inappropriate. For laminar flow

$$\lambda = \frac{64}{R_e} \quad . \tag{2.32}$$

Other emperical solutions for turbulent pipe flow describe the shape of the velocity profile as a function of radius. Nikuradse developed a relation,

$$\frac{u}{U} = \left(\frac{r}{R}\right)^{\frac{1}{m}} \quad , \tag{2.34}$$

where U is the mainstream value and m is a constant that varies with Reynolds number. The value for m is 6 for R_e = 4000, 7 for R_e = 100,000 and 10 for R_e values up to 3,240,000. The 1/7 power law can be developed by substituting Blasius' value for λ, into equation 2.28, solving for τ_o and equating that to v^*,

$$v^* = \sqrt{\frac{\tau_o}{\rho}} \quad , \tag{2.35}$$

where v* denotes the friction velocity. If $\bar{u}$ is eliminated by selecting a Blasius value of m = 7 corresponding to a $\bar{u}/u$ =0.8 and by writing R_e as a function of r, any distance from the centerline; then the power law can be written as

$$\frac{u}{v^*} = 8.74 \left(\frac{r v^*}{\upsilon}\right)^{\frac{1}{7}} \quad . \tag{2.36}$$

Many more solutions of the form of equation 2.31 are available for various pipe roughness assumptions and will not be covered here.

2.3.4 Jet and Orifice Flows

The circular jet flow field descriptions have been developed by Schlichting (1968), Reichardt (1942), Prandtl (1926), and Abramovich (1963). Prandtl argued, with his mixing length concept, that the width of the jet varied as the mixing length; also that the transverse velocity, and hence the width of the jet, varies linearly with the distance from the jet source. Observations also showed that the center line velocity decayed as the inverse of the distance from the jet source. Schlichting developed a circular jet solution for the Navier-Stokes equation by assuming a constant pressure gradient and a constant jet momentum flux. These relations are written as:

$$J = 2\pi \rho \int_0^\infty u^2 r \, dr, \qquad \text{constant momentum flux;} \qquad (2.37)$$

$$u \frac{\partial u}{\partial x} + v \frac{\partial u}{\partial r} = \nu \frac{1}{r} \frac{\partial}{\partial r}\left(r \frac{\partial u}{\partial r}\right), \qquad \text{equation of motion;} \qquad (2.38)$$

$$\frac{\partial u}{\partial x} + \frac{\partial v}{\partial r} + \frac{v}{r} = 0, \qquad \text{continuity equation;} \qquad (2.39)$$

where J is the momentum flux. Along the jet axis, the radial component of velocity, v, is zero. The centerline axial velocity component is a maximum (whose derivative with respect to r is equal to zero). Additionally, far from the jet centerline, there is no flow in the axial direction. Schlichting assumed the jet width to be proportional to x^n and that a stream function, whose derivatives yield the velocity functions, also existed as a power function of x. Judging by order of magnitude he argued that the stream function, Ψ , exists and takes the form

$$\Psi = \upsilon x \, f(\eta), \quad \text{where} \quad \eta = \frac{r}{x} , \tag{2.40}$$

which yields velocity components:

$$u = \frac{\upsilon}{x} \frac{f'}{\eta} \quad \text{and} \quad v = \frac{\upsilon}{x} \left(f' - \frac{f}{\eta} \right) , \tag{2.41}$$

where the (') notation indicates the derivative of f. Equations 2.41 are then substituted into equation 2.38 which is written in terms of f and integrated. The constants of integration are evaluated using the boundary conditions and the momentum flux equation 2.37. The expressions for u and v are then expressed as

$$u = \frac{3J}{8\pi \mu x} \frac{1}{\left(1 - \frac{1}{4} e^2\right)^2} \quad \text{and} \tag{2.42}$$

$$v = \frac{1}{4} \sqrt{\frac{3}{\pi}} \frac{\sqrt{\frac{J}{\rho}}}{x} \frac{e - \frac{1}{4} e^3}{\left(1 + \frac{1}{4} e^2\right)^2} , \tag{2.43}$$

$$\text{where} \quad e = \sqrt{\frac{3}{16x}} \frac{\sqrt{\frac{J}{\rho}}}{\upsilon} \frac{r}{x} . \tag{2.44}$$

It is, therefore, seen that u varies as the inverse of x along the jet centerline. The solution for the turbulent jet case takes the same form where a virtual kinematic viscosity replaces μ in equation 2.42. The centerline velocity decay and jet width develops in the same manner for both the laminar and turbulent submerged circular jet cases.

When the jet is placed in an axially symmetric pipe, the flow field is characterized as orifice flow. Orifice structures are used in this work to simulate stenoses or coarctations. The flow head losses for various orifice sizes and shapes are well documented (Tuve and Sprenkle, 1935; and Lea, 1938).

Various orifice shapes may be represented by their orifice coefficients, C, which specify losses, which must be considered, to achieve a balance of energy as predicted by the Bernoulli energy equation (2.8). For steady pipe flow, the orifice coefficient C is defined by

$$Q = CA\sqrt{2g\left(\frac{P_1}{\gamma} + h_1 - \frac{P_2}{\gamma} - h_2\right)}\,, \tag{2.45}$$

where A is the orifice lumen cross-sectional area, Q is the total flow rate, g is the gravitational acceleration, γ is the specific weight of the fluid and h is the height above a datum in the gravitational field. Subscripts 1 and 2 refer to upstream and downstream stations from the orifice respectively. Mills (1968) and Macagno and Hung (1967) have examined orifice flow fields for orifice Reynolds numbers up to 200. They have observed a trapped eddy or vortex ring just distal to the orifice. In steady flow, this vortex ring does not contribute to the actual flow, but it does tend to shape the jet flow vena contracta. As the Reynolds number increases, the shape of the vortex ring distorts and elongates. When the jet subsides in pulsatile flow, this vortex ring should expand and enter the main flow.

2.4 Energy and the Frequency Spectrum

Statistical analysis techniques have been employed to examine the structure of turbulent flows and hence provide insight into transition flows. The scales of turbulence have been described by Hinze (1969), Bradshaw (1971), and Tennekes and Lumley (1972). The integral scale relates the largest eddy size to the scale of the flow boundaries such as the radius or diameter of a pipe. Eddies of this size interact with the main stream motion. A microscale describes the small eddies which show no directional, properties, and participate in viscous dissipation of energy. Eddy sizes can be thought of as small fluctuation waves with corresponding wave numbers. The energy balance of the flow across various wave lengths yields an energy frequency distribution for idealized isotropic turbulent flow which suggests the relative role played by the mean fluid, the Reynolds stresses, and viscosity. The energy balance is maintained between the main stream kinetic energy source and the dissipating effects found in the turbulent motion and viscous interaction.

2.4.1 Turbulence Scales

The scales of turbulent motion are developed through the use of autocorrelation concepts. The turbulent velocity components at one point are compared to those at another point and their spatial correlation is developed as

$$G(x) = \frac{(u_a)(u_b)}{\sqrt{\overline{u_a^2} \cdot \overline{u_b^2}}}, \tag{2.46}$$

where the bar above the velocity term(s) implies time averaging. It is obvious that the greatest value any correlation type relationship can take on is unity, when $u_a = u_b$. Points a and b can be pictured as moving ever closer together. Some point is reached where the velocity fluctuations at a and b will be identical as they are influenced by the same eddy or eddy wave. If a correlation function is developed over all distances between points, then a distribution is developed for the correlation function as a function of distance, x, between points. The function will have a maximum at x = 0 and will decline for all larger values of x. The small eddy size or microscale is approximated by writing a Taylor series expansion of the correlation function and retaining terms only up to the second order. This will leave a parabolic approximation for the correlation function which will intersect the distance axis at λ_s, the small scale of turbulence. The integral, or large scale of turbulence, is of the same order as the size of the apparatus containing the fluid. Its value is obtained by integrating the correlation function over all values of point separation, x. The integral size is the value of x beyond which the correlation is essentially equal to zero.

Taylor (1935, 1938) examined temporal correlations made at the same point having time as the variable,

$$G(t) = \frac{\overline{u(t) \cdot u(t-t')}}{u^2(t)} \quad , \tag{2.47}$$

where t' is some time later than t. The correlation function can be examined over all time intervals and expanded in a Taylor series. By retaining terms up to second order another parabolic approximation is developed which intersects the time axis at the time corresponding to the Eulerian time or microscale. This scale is a measure of the most rapid changes or fluctuations which occur in the flow.

2.4.2 Turbulent Kinetic Energy

The energy distribution is obtained by multiplying the Navier-Stokes equations, containing turbulent and periodic terms, by the decomposed velocity expressions in equations 2.3 through 2.6. Hussain (1977) performed this substitution, time, and phase averaged the resultant expressions and obtained energy distribution for the mean flow, periodic fluctuations and turbulent contributions. Each of the three resulting energy expressions had similar terms. The Reynolds stress terms appeared in the organized flow equation as a negative term representing the loss of main flow kinetic energy because of shear work. In the turbulent expression the similar term is positive and indicative of turbulent energy production. If the periodic terms are neglected and steady state incompressible flow is assumed, then the main stream energy and the turbulent energy expressions are:

Total Motion Energy (time rate per unit mass)

$$\underset{A}{\frac{1}{2}\frac{\partial}{\partial t}(u_i u_i)} = \underset{B}{-\frac{\partial}{\partial x_i} U_i\left(\frac{p}{\rho} + \frac{u_i u_i}{2}\right)} + \nu\left[\underset{D}{\frac{\partial}{\partial x_i} U_j\left(\frac{\partial u_i}{\partial x_j} + \frac{\partial u_j}{\partial x_i}\right)} - \underset{E}{\frac{\partial u_j}{\partial x_i}\left(\frac{\partial u_i}{\partial x_j} + \frac{\partial u_j}{\partial x_i}\right)}\right] \tag{2.48}$$

Turbulent Motion Energy (time rate per unit mass)

$$\underset{A'}{\frac{1}{2}\frac{d}{dt}\overline{u_i'^2}} = \underset{B'}{-\frac{\partial u_i'}{\partial x_i}\overline{\left(\frac{p}{\rho} + \frac{u_i'u_i'}{2}\right)}} - \underset{C'}{\overline{u_i'u_j'}\,\overline{\frac{\partial u_j'}{\partial x_i}}} + \nu\left[\underset{D'}{\frac{\partial}{\partial x_i}\overline{u_j'\left(\frac{\partial u_i'}{\partial x_j} + \frac{\partial u_j'}{\partial x_i}\right)}} - \underset{E'}{\frac{\partial u_j'}{\partial x_i}\left(\frac{\partial u_i}{\partial x_j} + \frac{\partial u_j}{\partial x_i}\right)}\right] \tag{2.49}$$

The A and A' terms are the change in kinetic energy for the total flow and the turbulent flow respectively. The B and B' terms are the convective transport or diffusion by turbulence of the total or turbulent energy. The D and D' terms are the work done by viscous shear stress on the total motion and turbulent motion. The E and E' terms are the dissipation terms. The C' term is the energy transferred from the mean motion to the turbulent motion through turbulent shear stresses. This is effectively the turbulence production term and is made up of Reynolds stresses. These separate terms give an idea of the type of mechanisms which may be simultaneously involved in any turbulent flow. Certain terms have a varying effect with eddy size. The dissipation terms are significant at the small eddy sizes while they can often be neglected in the main fluid motion if viscous forces are small compared to inertia forces. In pulsatile flow the dissipative effects may not be as pronounced since the flow never reaches a fully developed steady condition.

The energy of isotropic turbulence can be examined over a frequency range by taking a Fourier transform of the correlation function. By selectively using appropriate eddy scales over various wave number or frequency ranges, Hinze (1959) found that power laws can be developed which show that the energy, as a function of frequency, decays as wave number to the -5/3 power for the Kolmogorov inertial subrange. Here energy cascades from the large vortices to smaller vortices with little energy dissipation. Energy also decays as wave number to the -7 power for the upper wave number range where viscous dissipative effects are strong. For nonisotropic eddies, Tchen (1953) examined a case where vorticity was large and interacted significantly with the main motion while eddy energy cascade and viscous effects were small. By order of magnitude arguments, he developed a -1 power law for strong viscous interaction with the main flow stream in the low wave number range.

Portions of these mechanisms may come into play in the production and dissipation of the modeled pulsatile jet. Each of these relationships were developed for steady flow, however, their interpretations may provide insight into understanding the downstream pulsatile stenosis flow field. For pulsatile flow it is expected that the -7 power law will not come into play in any dominant manner the pulsatile cycle will not allow sufficient time for the flow to become fully developed. The -1 and -5/3 ranges should occur since they are related to eddy production (-1) and energy cascade (-5/3). In some cases where production is strong (high R_e jet) the -1 slope should be dominant across most frequencies of interest.

2.5 Vortex Shedding

Vortices may be shed because of the presence of any obstruction in a flow field. The vortex street that sheds behind a cylinder explains the aeolean tone and wire singing effects noticeable along telephone lines on windy days. The vortices which are shed from a jet nozzle have been studied by Anderson (1956), Crow and Champagne (1971), Becker and Massaro (1968), Rockwell and Niccolls (1972), and Maxworthy (1972). They show that vortex rings are shed from the orifice at frequencies that are predictable by the Strouhal number, S, defined as

$$S = \frac{fd}{\bar{u}} , \tag{2.50}$$

where the orifice size, d, and the mean velocity, $\bar{u}$, are known. Hussain and Ramjee (1975, 1976) have shown that as the jet is pulsed with up to 10% velocity magnitude fluctuations the jet shedding frequency does not change significantly and that turbulence of moderate intensities does not affect the vortex shedding.

For the stenosis model, it can be expected that vortices will be shed from the orifice and that measurements made close to the orifice should exhibit shedding frequencies which relate to the orifice size.

The mean velocity in equation 2.50 may cause some concern in the pulsatile flow problem since velocity fluctuations well in excess of 10% would be expected.

CHAPTER III

APPARATUS AND PROCEDURES

3.1 Experiment Overview

A mock circulation loop was built for the experimental investigation. The stenosis model was installed in the loop. Pulsatile waves of water were propelled through the model under physiological pressures. Provisions were added to make steady flow comparisons through the use of a centrifugal pump as a parallel fluid driving source. Run sequences were designed to obtain downstream velocity profiles at various axial locations and along the centerline for several blockage sizes and pulse wave form variations in rate and duration.

3.2 Mock Circulation System

The mock circulation system, shown in Figure III.1, is composed of a flow loop, compliance simulator, resistance simulator, pulsatile pump, and the monitoring and measuring equipment. The loop permitted stenosis model exchange without significant disturbance of the flow setup. The operating parameters of the loop were controlled by the pump adjustments, model size, and probe location. Pressures and flow rates were compared to published physiological data for comparably severe stenoses.

3.2.1 Flow Loop

The flow loop was constructed of tygon tubing, 1.59 cm in diameter, which connected to pressure transducers, a hot film anemometer probe, stenosis model, compliance simulator, rotometer flow meter, reservoir and compliance chamber, and the pulsatile and steady flow pumps. The compliance simulator, located downstream of the model, was a silastic sleeve enclosed in a pneumatically pressurized plastic box. As water flowed through the box, the compliance effect was obtained by adjusting the control pressure on the outside of the silastic sleeve. This pressure and the reservoir chamber proximal pressure were adjusted together for each run sequence.

Peripheral resistance was simulated with a thumb screw clamp around the tygon tubing located distal to the model and compliance simulator. The reservoir chamber and proximal compliance simulator consisted of a 24 liter pressure tank filled two-thirds full of water. Regulated air pressure was supplied to the upper third of the container while the base of the tank was fitted with water inlet and outlet ports. Input and output flow rate was adjusted with thumb screw resistance clamps.

A pneumatic pulser described by Akers et al (1966) and Weiting (1966) was used to provide the pulsatile pressure wave. The pump is composed of two clear plastic domes separated by a silastic membrane. A 1/4 inch I.D. air hose connects the upper dome of the pump to the pulser which electronically controls the input of regulated pressurized and vacuum air to the upper side of the pump membrane (see Figure III.1b). The lower half of the pump is fitted with inflow and outflow passages each having inline ball type check valves to allow one-way pumping and to prevent significant regurgitation. The pulser electronics provided selectable heart rates, systolic duration intervals and regulated air and vacuum pressure controls.

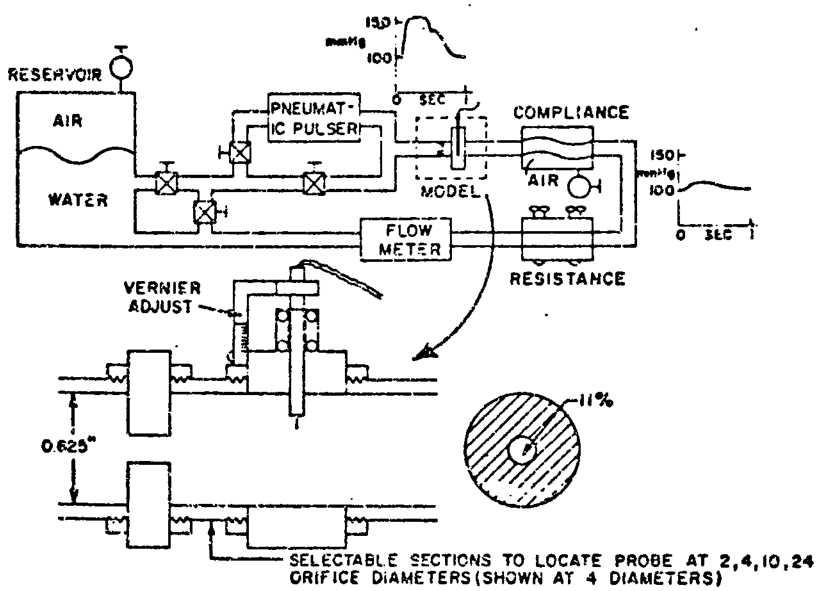

FIGURE III.1 a) COARCTATION FLOW LOOP AND MODEL SHOWN SCHEMATICALLY.

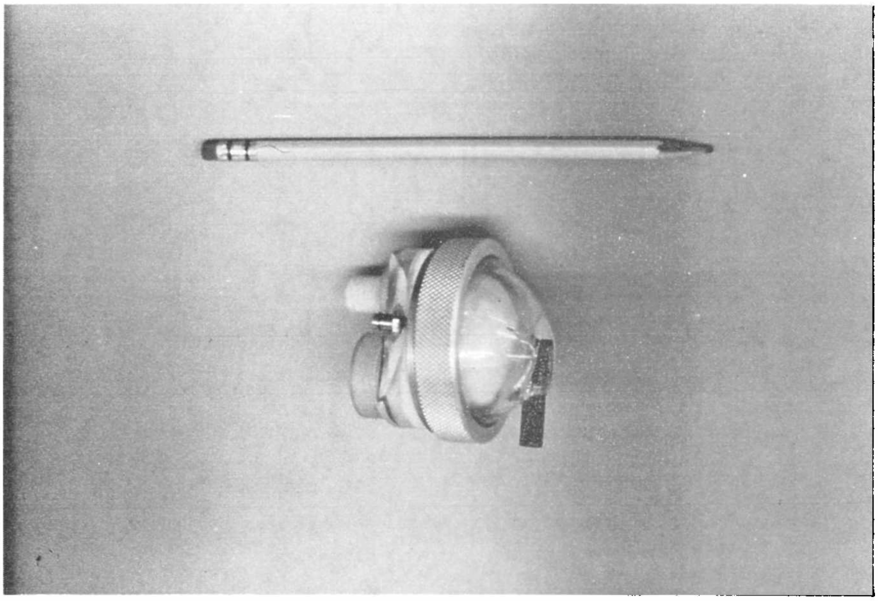

FIGURE III.1 b) PNEUMATIC PULSATILE PUMP

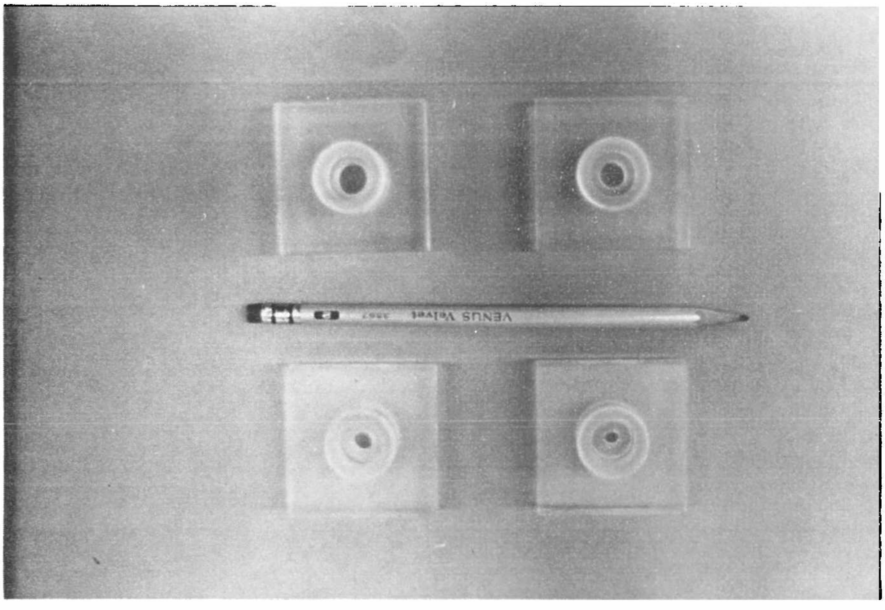

FIGURE III.1 c) COARCTATION ORIFICE MODELS - 10, 20, 30, 50% SIZES SHOWN

Steady flow comparisons were provided by operating a centrifugal pump located in parallel with the pneumatic pulser. The steady flow pump was controlled with a rheostat which could vary flow rate from zero to five liters per minute. The two pumping systems were placed in parallel upstream of the stenosis model and were isolated with manual diverter valves.

3.2.2 Measurement Equipment

Data recorded during the runs consisted of temperature, pressure, probe location, instantaneous axial velocity at a point in the flow, total flow rate, pulse rate, and time (used to identify run sequences for digital processing). The pressures, velocity and time were recorded on both magnetic tape and strip chart recorder paper. All other measurements were recorded on log sheets.

The liquid in the loop was maintained at constant temperature, for all practical purposes, since the fluid was not changed out over several days of recording and the loop was located in an air conditioned laboratory. Each run sequence group was completed during the same recording session. Flow loop pressures were recorded by side mounted pressure taps located proximal to the blockage and distal to the anemometer probe. The pressure signals were signal conditioned, monitored on a scope and recorded on stripchart recorder paper and magnetic tape. The velocity measurements were made with a Thermal Systems Inc. 1050 series anemometer and a hot film cylinderial miniature probe, Thermal Systems Inc. model 1260-10W. Instantaneous values were signal conditioned, displayed on a scope, and recorded on magnetic tape and strip chart recorder paper. An Inter-Range Instrumentation Group type B time code generator placed timing signals on the magnetic tape and the strip chart to facilitate run logging. The probe tip was mounted on a specially designed probe holder that was fitted with "O" rings to prevent leakage. The holder included a micrometer type adjustable probe advance mechanism to locate and identify accurately the radial probe position. Flow rate data were measured by an inline rotometer flowmeter and were recorded on run sequence log sheets. The pulsatile pump control settings were also logged for each run.

3.2.3 Data Processing

The pressure, velocity, and timing data were recorded on an Ampex 1200 recorder. Pressure data were scaled and displayed in the raw form. Velocity data were digitally sampled and frequency analyzed on a Univac 1108 computer.

The velocity signals recorded on FM analog tape were digitized at 2500 samples per second, which yields an expected 1250 Hz upper frequency accuracy according to the Nyquist sampling theorem (Bendat and Piersol, 1971). The frequency analyses were performed by the National Aeronautics and Space Administration supplied VIBAN 3 computer program. This program incorporates a Fast Fourier Transform to compute a power spectral density profile for the input data. Data selection criteria and results are discussed in Chapter 4.

3.3 Data Collection Sequences and Procedures

The data recording sequences were selected to allow the development of a geometric and temporal description of the flow field distal to a stenosis. Variations in stenosis size and pulse shape were also desired. Frequency analysis were required for selected runs for additional flow interpretation and possible murmur correlation. Baseline steady state flow measurements were performed to compare the pulsatile flow to existing orifice flow data. To meet these objectives, three types of run sequences were developed: (1) geometric distal profiles for a select orifice size, (2) centerline velocity comparisons for a range of orifice sizes and flow rates, and (3) pulse pressure variations. For the first two sequences, both steady and pulsatile flow data were recorded without changing the model setup.

3.3.1 General Experimental Procedures

Prior to each data collection sequence, point calibration checks were made on the loop parameters. Setup of the flow loop consisted of replacing the stenosis model and positioning the anemometer probe. The pulser was then activated and the desired pressure pulse wave forms were obtained by adjusting the reservoir and capacitance simulator regulated pressures and the pneumatic pulser electronics. All set conditions were held constant for the geometry runs and were adjusted to achieve desired flow rates for the stenosis size variation runs. The pulse pressure wave variation runs were conducted using the geometry set conditions, except where parameter variations were required to produce the desired wave changes. Run sequence data are summarized in Table IV.1.

3.3.2 Geometric Profiles Downsteam from the Jet

The 11% open lumen orifice was selected for this run sequence as being representative of a relatively severe stenosis. Pressure profiles and stenosis sizes were summarized by Karnel (1968) for up to 250 coarctation cases. The average pressures found by Karnel were used to operate the flow loop. The axial locations for the profiles were selected by examining submerged jet profiles as predicted by Corrisin and Uberoi (1949). It was expected that at less than 4 diameters distal to the orifice, profiles would represent potential core flow conditions. Beyond 4 diameters, the ratio of centerline velocity to mean velocity would decay rapidly reaching a relatively steady state value beyond 20-24 diameters downstream from the orifice.

Confined jet flow should experience an interaction resulting from "no slip" conditions at the wall and therefore the velocity profile decay should be at least as rapid as predicted for the submerged jet above. Therefore, the profile selections were made at 2, 4, 10, and 24 orifice diameters downstream from the orifice. At each axial station velocity histories were recorded at seven radial points from the wall to the centerline. After each pulsatile profile was completed at the given axial location, the profile was repeated for steady flow using the inline flow meter as the control parameter.

The geometric profile data are summarized in Table IV.1. The identification code used in the table is of the form,

AXRY (Gemoetric Profiles).

A refers to axial location, X is the axial position 1,2,3,4 corresponding to 2,4,10, and 24 diameters respectively. R refers to the radial probe position and Y is the radial location from 0 at the wall to 6 at the pipe centerline. A suffix of S is added to indicate steady flow runs.

3.3.3 Centerline Variations Due to Stenosis Size

To examine the effects of orifice or stenosis size, centerline velocity recordings were made for orifice sizes of 11, 20, 30, and 50%. This size range was selected to cover "choked flow" conditions which were expected for the 11% and possibly the 20% sizes (Berguer and Hwang,

1974) as well as non-symptomatic conditions which are present in many undiagnosed stenosis cases (Karnell, 1968).

Since flow rate could have been limited for the severe blockages, it was purposely varied for each of the cases examined. Flow rates were selected from one to four liters per minute when not choke limited. Pulsatile flow rate variations were achieved by increasing the proximal pulse pressure, while maintaining a 1 Hz pulse rate.

The identification code in Table IV.1 used for the stenosis size is

CXYFZ (Orifice Size and Flow Rate).

C identifies the sequence as the orifice size variation sequence; X is the selected orifice size 1, 2, 3, and 4, referring to the 11, 20, 30, and 50% sizes respectively; Y is the centerline axial location 1 or 2 referring to 2 diameters (inside submaged jet potential core) and 10 diameters (well beyond potential core) downstream from orifice respectively; and F refers to flow rate variation where Z is the selected flow rate of 1, 2, 3, or 4 liters per minute, when achievable. Actual flow rates are also shown in the Table IV.1. A suffix of S is added to indicate steady flow runs.

3.3.4 Pulse Wave Variations

The pressure wave for the pulsatile flow was varied by adjusting the systolic time interval of the pulsatile pump electronics and by holding the systolic time interval fixed while varying the pulse rate. The orifice size and flow rate sequence also provided data on amplitude pressure variations. Systolic time interval does not usually vary significantly from beat-to-beat as long as sufficient ventricular filling time is available. A range from 250 to 500 milliseconds was selected as encompassing most physiological cases. The pulse rate runs were performed over a range of 50 to 110 beats per minute which spans most resting heart rates.

The identification codes used in Table IV.1 for these runs are as follows:

SDXXX (Systolic Duration),

where SD is the systolic duration identifier and XXX is the interval selected in milliseconds; and

HRYYY (Heart Rate),

where HR is the heart rate variation identifier and YYY is the selected pulse rate in beats per minute.

CHAPTER IV

EXPERIMENTAL RESULTS AND DISCUSSION

4.1 Summary of Experimental Results

Data are presented for fifty-six geometric and temporal profile runs for the 11% orifice; sixty-four orifice size and flow rate runs for the 11, 20, 30, and 50% orifices; and seventeen pulse wave variation runs for the 11% orifice. Velocity profiles distal to the 11% orifice show a systolic jet pulse and a secondary washing of a disturbed fluid slug. The comparisions to flow conditions which were reviewed earlier indicate that the flow is neither fully laminar nor turbulent, but rather is "disturbed", possessing turbulent jet features during systole and dissipation features in diastole. The pulsatile flow can be reduced to two quasi steady state flows which show fair agreement with steady flow predictions. Frequency analysis indicates that orifice size relationships may be deduced from the systolic phase centerline velocity fluctuation data.

4.2 Data Table Discussion

Table IV.1 summarizes the data obtained for the several run sequences. Each line in the table summarizes one sequence. The sequence identifier appears in the first column. The stenosis size is the percent ratio of orifice area to pipe lumen area. The probe locations are given in terms of downstream orifice diameters and radius percent measured from the wall. The proximal and and distal pressure data are given in mmHg. The mean pressures are obtained by assuming that the systolic pulse occurs over

TABLE IV.1 RUN SEQUENCE SUMMARY DATA TABLE

Run Id.	Stenosis Size % Lumen	Prob. Location AX Diam.	Prob. Location Rad. % R	Prox. Sys/Dia. mm Hg	Prox. PP mm Hg	Prox. MN mm Hg	Distal Sys/Dia. mm Hg	Dist. MN mm Hg	Sys Dur ms	Flow Rate l/min	V Max/min cm/sec	HR bpm	Freq Anal	$\bar{V}_o$ cm/sec	$\bar{V}_t$ cm/sec	R_{e_o} d^o	R_{e_t} D^t
A1R0	11	2D	W	165/95	70	113	110/100	103	300	1.4	40/15	60	*	108	12	5838	1879
A1R1	11	2D	.83R	165/95	70	118	110/100	103	300	1.35	40/15	60	*	104	11	5838	1879
A1R2	11	2D	.67R	165/95	70	118	110/100	103	300	1.35	40/15	60	*	104	11	5838	1879
A1R3	11	2D	.50R	165/95	70	118	110/100	103	300	1.3	80/20	60	*	101	11	5838	1879
A1R4	11	2D	.33R	160/90	70	113	105/95	98	300	1.3	125/25	60	*	101	11	5838	1879
A1R5	11	2D	.167R	165/95	70	118	110/100	103	300	1.35	140/20	60	*	104	11	5838	1879
A1R6	11	2D	C/L	165/95	70	118	110/100	103	300	1.35	143/20	60	*	104	11	5838	1879
A1R0S	11	2D	W	-	--	108	-	103	-	1.35	15	--	*	104	11	5855	1879
A1R1S	11	2D	.83R	-	--	108	-	103	-	1.35	17	--	*	104	11	5855	1879
A1R2S	11	2D	.67R	-	--	108	-	103	-	1.35	25	--	*	104	11	5855	1879
A1R3S	11	2D	.50R	-	--	108	-	103	-	1.35	60	--	*	104	11	5855	1879
A1R4S	11	2D	.33R	-	--	108	-	103	-	1.35	60	--	*	104	11	5855	1879
A1R5S	11	2D	.17R	-	--	108	-	103	-	1.35	75	--	*	104	11	5855	1879
A1R6S	11	2D	C/L	-	--	108	-	103	-	1.35	80	--	*	104	11	5855	1879
A2R0	11	4D	W	160/95	65	117	108/98	101	300	1.4	40/15	60	*	108	12	5833	1879
A2R1	11	4D	.83R	160/95	65	117	108/98	101	300	1.35	55/12	60	*	104	11	5833	1879
A2R2	11	4D	.67R	160/95	65	117	108/98	101	300	1.3	65/18	60	*	101	11	5833	1879
A2R3	11	4D	.50R	160/95	65	117	108/98	101	300	1.33	110/15	60	*	103	11	5833	1879
A2R4	11	4D	.33R	160/95	65	117	108/98	101	300	1.33	135/15	50	*	103	11	5833	1879
A2R5	11	4D	.17R	160/95	65	117	108/98	101	300	1.33	160/20	60	*	103	11	5833	1879
A2R6	11	4D	C/L	160/95	65	117	108/98	101	300	1.33	170/11	60	*	103	11	5833	1879
A2R0S	11	4D	W	-	--	110	-	101	-	1.35	20	--	*	104	11	5945	1879
A2R1S	11	2D	.83R	-	--	110	-	101	-	1.5	25	--	*	116	13	5945	1879
A2R2S	11	2D	.67R	-	--	110	-	101	-	1.35	32	--	*	104	11	5945	1879
A2R3S	11	4D	.50R	-	--	110	-	101	-	1.33	35	--	*	103	11	5945	1879
A2R4S	11	4D	.33R	-	--	110	-	101	-	1.35	50	--	*	104	11	5945	1879
A2R5S	11	4D	.17R	-	--	110	-	101	-	1.35	70	--	*	104	11	5945	1879
A2R6S	11	4D	C/L	-	--	110	-	101	-	1.35	65	--	*	104	11	5945	1879
A3R0	11	10D	W	160/95	65	117	107/95	99	280	1.35	20/5	60	*	104	11	5878	1879
A3R1	11	10D	.83R	160/95	65	117	107/95	99	280	1.35	25/5	60	*	104	11	5878	1879
A3R2	11	10D	.67R	160/95	65	117	107/95	99	280	1.35	30/5	50	*	104	11	5878	1879
A3R3	11	10D	.50R	160/95	65	117	107/95	99	280	1.45	37/5	60	*	108	12	5878	1879
A3R4	11	10D	.33R	160/95	65	117	107/95	99	280	1.35	33/5	60	*	104	11	5878	1879
A3R5	11	10D	.17R	160/95	65	117	107/95	99	280	1.45	35/7	60	*	113	12	5878	1879
A3R6	11	10D	C/L	160/95	65	117	107/95	99	280	1.35	33/7	60	*	104	11	5878	1879

TABLE IV.1 RUN SEQUENCE SUMMARY DATA TABLE (CONTINUED)

Run Id.	Stenosis Size % Lumen	Prob. Location AX Diam.	Prob. Location Rad. % R	Prox. Sys/Dia. mm Hg	Prox. PP mm Hg	Prox. MN mm Hg	Distal Sys/Dia. mm Hg	Dist. MN mm Hg	Sys Dur ms	Flow Rate l/min	V Max/min cm/sec	HR bpm	Freq Anal	$\bar{V}_o$ cm/sec	$\bar{V}_t$ cm/sec	R_{e_o} d	R_{e_t} D
A3R0S	11	10D	W	--	--	114	--	103	-	1.35	12	--	*	104	11	6013	2050
A3R1S	11	10D	.83R	--	--	114	--	103	-	1.4	8	--	*	108	12	6013	2050
A3R2S	11	10D	.67R	--	--	114	--	103	-	1.4	8	--	*	108	12	6013	2050
A3R3S	11	10D	.50R	--	--	114	--	103	-	1.35	7	--	*	104	11	6013	2050
A3R4S	11	10D	.33R	--	--	114	--	103	-	1.4	8	--	*	108	12	6013	2050
A3R5S	11	10D	.17R	--	--	114	--	103	-	1.4	7.5	--	*	108	12	6013	2050
A3R6S	11	10D	C/L	--	--	114	--	103	-	1.4	7.5	--	*	108	12	6013	2050
A4R0	11	24D	W	165/98	67	120	110/95	100	280	1.5	18/5	60	*	116	13	6209	2050
A4R1	11	24D	.83R	165/98	67	120	110/95	100	280	1.45	29/5	60	*	113	12	6209	2050
A4R2	11	24D	.67R	165/98	67	120	110/95	100	280	1.47	30/5	60	*	114	12	6209	2050
A4R3	11	24D	.50R	165/98	67	120	110/95	100	280	1.37	28/4	60	*	106	12	6209	2050
A4R4	11	24D	.33R	165/98	67	120	110/95	100	280	1.45	30/5	60	*	113	12	6209	2050
A4R5	11	24D	.17R	165/98	67	120	110/95	100	280	1.35	28/5	60	*	104	11	6209	2050
A4R6	11	24D	C/L	165/98	67	120	110/95	100	280	1.37	28/3	60	*	106	12	6209	2050
A4R0S	11	24D	W	--	--	115	--	105	-	1.45	7	--	*	113	12	6120	2050
A4R1S	11	24D	.83R	--	--	115	--	105	-	1.5	14	--	*	116	13	6120	2050
A4R2S	11	24D	.67R	--	--	115	--	105	-	1.4	15	--	*	108	12	6120	2050
A4R3S	11	24D	.50R	--	--	115	--	105	-	1.4	15	--	*	108	12	6120	2050
A4R4S	11	24D	.33R	--	--	115	--	105	-	1.35	13	--	*	104	11	6120	2050
A4R5S	11	24D	.17R	--	--	115	--	105	-	1.4	13	--	*	108	12	6120	2050
A4R6S	11	24D	C/L	--	--	115	--	105	-	1.35	14	--	*	104	11	6120	2050
C11F1	11	2D	C/L	165/95	70	113	102/95	97	280	1.0	140/15	60	*	77	8	4335	1366
C11F2	11	2D	C/L	--	--	-	--	-	280	1.5	135/15	60	*	116	13	6531	2220
C11F3	11	2D	C/L	170/95	75	120	100/90	93	280	2.0	155/20	60	*	155	17	8726	2903
C11F4	11	2D	C/L	195/105	90	135	110/95	100	280	2.5	175/20	60	*	193	21	10866	3587
C11F1S	11	2D	C/L	--	--	115	--	107	-	1.0	67.5	--	*	77	8	4335	1366
C11F2S	11	2D	C/L	--	--	115	--	100	-	2.0	102	--	*	155	17	8726	2903
C11F3S	11	2D	C/L	--	--	133	--	100	-	3.0	122.5	--	*	232	25	13062	4270
C11F4S	11	2D	C/L	--	--	140	--	88	-	4.0	137	--	*	309	34	17397	5807
C12F1	11	10D	C/L	160/100	60	120	110/83	92	280	1.0	53/5	60	*	77	8	4335	1366
C12F2	11	10D	C/L	165/102	63	123	110/85	93	280	1.5	53/4	60	*	116	13	6531	2220
C12F3	11	10D	C/L	170/105	65	127	115/90	98	280	2.0	57/5	60	*	155	17	8726	2903
C12F4	11	10D	C/L	190/112	78	138	113/93	100	280	2.5	63/5	60	*	193	21	10866	3587
C12F1S	11	10D	C/L	--	--	115	--	107	-	1.0	20	--		77	8	4335	1366
C12F2S	11	10D	C/L	--	--	120	--	100	-	2.0	38	--	*	116	13	6531	2220
C12F3S	11	10D	C/L	--	--	135	--	100	-	3.0	47	--		232	25	13062	4270
C12F4S	11	10D	C/L	--	--	150	--	85	-	4.0	53	--		309	34	17397	5807

TABLE IV.1 RUN SEQUENCE SUMMARY DATA TABLE (CONTINUED)

Run Id.	Stenosis Size % Lumen	Prob. Location AX Diam.	Prob. Location Rad. % R	Prox. Sys/Dia. mm Hg	Prox. PP mm Hg	Prox. MN mm Hg	Distal Sys/Dia. mm Hg	Dist. MN mm Hg	Sys Dur ms	Flow Rate l/min	V Max/min cm/sec	HR bpm	Freq Anal	$\bar{V}_o$ cm/sec	$\bar{V}_t$ cm/sec	R_{e_o} d^o	R_{e_t} D^t
C21F1	20	2D	C/L	160/95	65	127	125/100	108	280	1.00	65/12	60		42	8	3226	1366
C21F2	20	2D	C/L	160/105	60	130	120/95	103	280	2.0	65/8	60		83	17	6374	2903
C21F3	20	2D	C/L	165/100	65	133	118/94	102	280	3.0	65/5	60		124	25	9523	4270
C21F4	20	2D	C/L	165/100	75	133	102/90	93	280	3.57	67/3	60		147	30	11290	5124
C21F1S	20	2D	C/L	--	--	118	--	109	-	1.0	12	--		42	8	3226	1366
C21F2S	20	2D	C/L	--	--	122	--	108	-	2.0	33	--		83	17	6374	2903
C21F3S	20	2D	C/L	--	--	125	--	107	-	3.0	42	--		124	25	9523	4270
C21F4S	20	2D	C/L	--	--	130	--	105	-	4.0	45	--		166	34	12749	5807
C22F1	20	10D	C/L	155/100	55	117	110/95	100	280	1.05	58/20	60	*	44	9	3379	1537
C22F2	20	10D	C/L	155/105	50	122	108/99	102	280	2.0	60/15	60	*	83	17	6374	2903
C22F3	20	10D	C/L	165/107	58	126	110/100	103	280	2.9	63/5	60	*	120	24	9216	4099
C22F4	20	10D	C/L	175/110	65	143	105/95	98	280	3.65	66/5	60	*	151	31	11597	5295
C22F1S	20	10D	C/L	--	--	113	--	103	-	1.0	10	--		42	8	3226	1366
C22F2S	20	10D	C/L	--	--	115	--	105	-	2.0	55/7	--	*	83	17	6374	2903
C22F3S	20	10D	C/L	--	--	125	--	108	-	2.9	23	--		120	24	9216	4099
C22F4S	20	10D	C/L	--	--	127	--	103	-	4.0	36	--		166	34	12749	5807
C31F1	30	2D	C/L	135/95	40	109	118/90	99	280	1.3		60		36	11	3391	1879
C31F2	30	2D	C/L	135/95	40	108	118/95	103	280	2.1		60		58	18	5463	3074
C31F3	30	2D	C/L	137/100	37	112	115/95	101	280	3.0		60		83	25	7819	4270
C31F4	30	2D	C/L	150/105	45	120	112/100	104	280	3.95		60		109	33	10268	5636
C31F1S	30	2D	C/L	--	--	112	--	109	-	.95	28	--		26	8	2450	1366
C31F2S	30	2D	C/L	--	--	112	--	106	-	2.0	42	--		55	17	5181	2903
C31F3S	30	2D	C/L	--	--	118	--	110	-	3.0	63	--		83	25	8919	4270
C31F4S	30	2D	C/L	--	--	118	--	106	-	4.0	66	--		110	34	10362	1366
C32F1	30	10D	C/L	140/80	60	100	110/80	90	280	1.0	65/25	60	*	28	8	2638	1366
C32F2	30	10D	C/L	138/82	55	101	108/83	91	280	2.0	65/10	60	*	55	17	5181	2903
C32F3	30	10D	C/L	138/75	63	96	99/80	86	280	3.0	68/5	60	*	83	25	8919	4270
C32F4	30	10D	C/L	140/75	65	97	90/75	80	280	4.0	70/10	60	*	110	34	10362	5807
C32F1S	30	10D	C/L	--	--	105	--	100	-	1.0	13	--		28	8	2638	1366
C32F2S	30	10D	C/L	--	--	110	--	105	-	2.0	22	--		55	17	5181	2903
C32F3S	30	10D	C/L	--	--	112	--	102	-	3.4	34	--	*	94	29	8855	4953
C32F4S	30	10D	C/L	--	--	115	--	107	-	4.0	33	--	*	110	34	10362	5807
C51F1	50	2D	C/L	128/70	58	99	108/80	90	280	1.0		60		17	8	2054	1366
C51F2	50	2D	C/L	135/75	60	95	105/80	88	280	2.0		60		34	17	4107	2903
C51F3	50	2D	C/L	135/90	45	105	110/90	96	280	3.0		60		50	25	6040	4270
C51F4	50	2D	C/L	145/90	55	108	110/90	96	280	3.95		60		66	33	7972	5636

TABLE IV.1 RUN SEQUENCE SUMMARY DATA TABLE (CONTINUED)

Run Id.	Stenosis Size % Lumen	Prob. Location AX Diam.	Prob. Location Rad. % R	Prox. Sys/Dia. mm Hg	Prox. PP mm Hg	Prox. MN mm Hg	Distal Sys/Dia. mm Hg	Dist. MN mm Hg	Sys Dur ms	Flow Rate l/min	V Max/min cm/sec	HR bpm	Freq Anal	$\bar{V}_0$ cm/sec	$\bar{V}_t$ cm/sec	$R_{e_{d^0}}$	$R_{e_{D^t}}$
C51F1S	50	2D	C/L	--	--	100	--	96	-	1.0	16	--		17	8	2054	1366
C51F1S	50	2D	C/L	--	--	104	--	97	-	2.0	30	--		34	17	4107	2903
C51F1S	50	2D	C/L	--	--	112	--	106	-	3.0	38	--		50	25	6040	4270
C51F1S	50	2D	C/L	--	--	117	--	106	-	4.0	47	--		67	34	8094	5807
C52F1	50	10D	C/L	130/84	46	99	102/84	90	280	1.1		60		18	9	2174	1537
C52F2	50	10D	C/L	125/75	50	93	97/81	86	280	2.0		60	*	34	17	4107	2904
C52F3	50	10D	C/L	125/75	50	93	95/78	84	280	3.0		60		50	25	6040	4270
C52F4	50	10D	C/L	125/76	49	92	90/75	80	280	4.0		60		67	34	8094	5807
C52F1S	50	10D	C/L	--	--	105	--	100	-	1.0	12	--		17	8	2054	1366
C52F2S	50	10D	C/L	--	--	110	--	105	-	2.0	23	--		34	17	4107	2903
C52F3S	50	10D	C/L	--	--	115	--	109	-	3.0	29	--		50	25	6040	4270
C52F4S	50	10D	C/L	--	--	120	--	110	-	4.0	34	--	*	67	34	8094	5807
1H50	11	2D	C/L	165/95	70	115	115/100	103	300	1.05		50		81	9	4560	1537
1H65	11	2D	C/L	165/90	75	115	110/92	97	300	1.35		65		104	11	5855	1879
1H80	11	2D	C/L	165/92	73	124	118/93	101	300	1.65		80		127	14	7150	2391
1H95	11	2D	C/L	168/95	73	125	107/90	95	300	2.05		95		158	17	5348	2903
1H110	11	2D	C/L	170/102	68	137	106/98	100	300			110					
3H50	11	10D	C/L	165/93	72	110	110/96	96	300	1.00		50	*	77	8	4335	1366
3H65	11	10D	C/L	168/93	75	115	113/93	95	300	1.3		65	*	101	11	5686	1879
3H80	11	10D	C/L	165/92	73	117	107/93	94	300	1.65		80	*	127	14	7150	2391
3H95	11	10D	C/L	168/93	75	125	94/88	91	300	2.15		95	*	166	18	9346	3074
3H110	11	10D	C/L	170/95	75	125	100/92	92	300	2.25		110	*	174	19	9796	3245
SD200	11	10D	C/L	160/90	70	101	100/86	87	200	1.0		65		77	8	4335	1366
SD250	11	10D	C/L	165/98	67	114	106/98	100	250	1.07		65	*	83	9	4673	1537
SD300	11	10D	C/L	165/93	72	115	115/96	93	300	1.38		65	*	107	12	6024	2050
SD350	11	10D	C/L	170/95	75	120	121/101	110	350	1.60		65	*	124	13	6981	2220
SD400	11	10D	C/L	170/95	75	128	126/103	104	400	1.68		65	*	130	14	7319	2391
SD450	11	10D	C/L	170/95	75	131	126/103	104	450	1.95		65	*	151	16	8501	2733
SD500	11	10D	C/L	160/95	65	135	115/102	108	500	1.90		65	*	147	16	8276	2733

one-third of the pulse period and that the pulse is generally rectangular in shape, therefore:

$$\text{Mean Pressure} = \text{Diastolic Pressure} + \tfrac{1}{3}\,(\text{Systolic Pressure} - \text{Diastolic Pressure}) \quad (4.1)$$

Mean pressures for the pulse wave variation sequences were obtained from an electronic averaging circuit which operated on the pressure outputs during the run. The pulse pressures are merely the difference between the systolic and diastolic values. The flow rate data were obtained by visually interpolating the fluctuations of the flow meter data. Maximum and minimum velocities were recorded signals obtained from the anemometer. The values are applicable for each run sequence group (e.g., geometric and temporal). The mean values of velocity were computed from the continuity equation for incompressible fluid flow using both the orifice and the tube diameters and the flow meter velocity readings. Reynolds numbers were computed from the same data. Frequency analysis was performed on runs which are indicated by a (*) in the table.

The magnitudes of the velocity profile for the steady flow runs are significantly lower than corresponding pulsatile runs. This can also be seen in the comparison between the mean pressures for pulsatile and steady runs. An obvious flow efficiency exists for the steady flow runs as compared to the pulsatile. That is, a greater amount of fluid can flow through the orifice for steady flow than for pulsatile flow for for the same pressure gradient. This is partially explained by the U^2 velocity to pressure gradient relationship, shown in equation 2.27. It describes less efficient turbulent flow as compared to the linear laminar flow velocity to pressure gradient relationship.

4.3 Distal Flow Profiles

Flow profile data are the instantaneous pulsatile velocity measured at a single point and, the point-by-point variations that occur at comparable points in the pulse period for a given axial location. Figure IV.1 shows typical proximal and distal pressure and accompanying velocity histories recorded near the wall and in the jet for the cross section two orifice diameters downstream from the orifice. From the pressure profiles, it can be seen that approximately 100 to 150 milliseconds of delay occurs between the peak pressure in proximal systole compared to distal systole. This agrees wtih Schlant's (1966) physiological observations for severe coarctation type stenoses. The pressure taps in the mock circulation system were approximately one meter apart and hence yield delays comparable to physiological conditions. The pressure wave peak lag results from the wave transmission speed and the loop distensibility. The compliance simulator expands to accept the pulse volume. This capacitive reserve is primarily responsible for the observed delay. Since water is essentially incompressible, the wave transmission delay would go undetected at one meter. The water pulse transmission velocity would result in a time lag of only 0.67 milliseconds; therefore, the capacitive nature of the compliance simualator provides realistic phase delays in agreement with Schlant's observations. It can also be seen from the velocity history records that the flow rate is somewhat constant during most of systole. This relatively constant velocity value indicates the presence of a quasi-steady state phase.

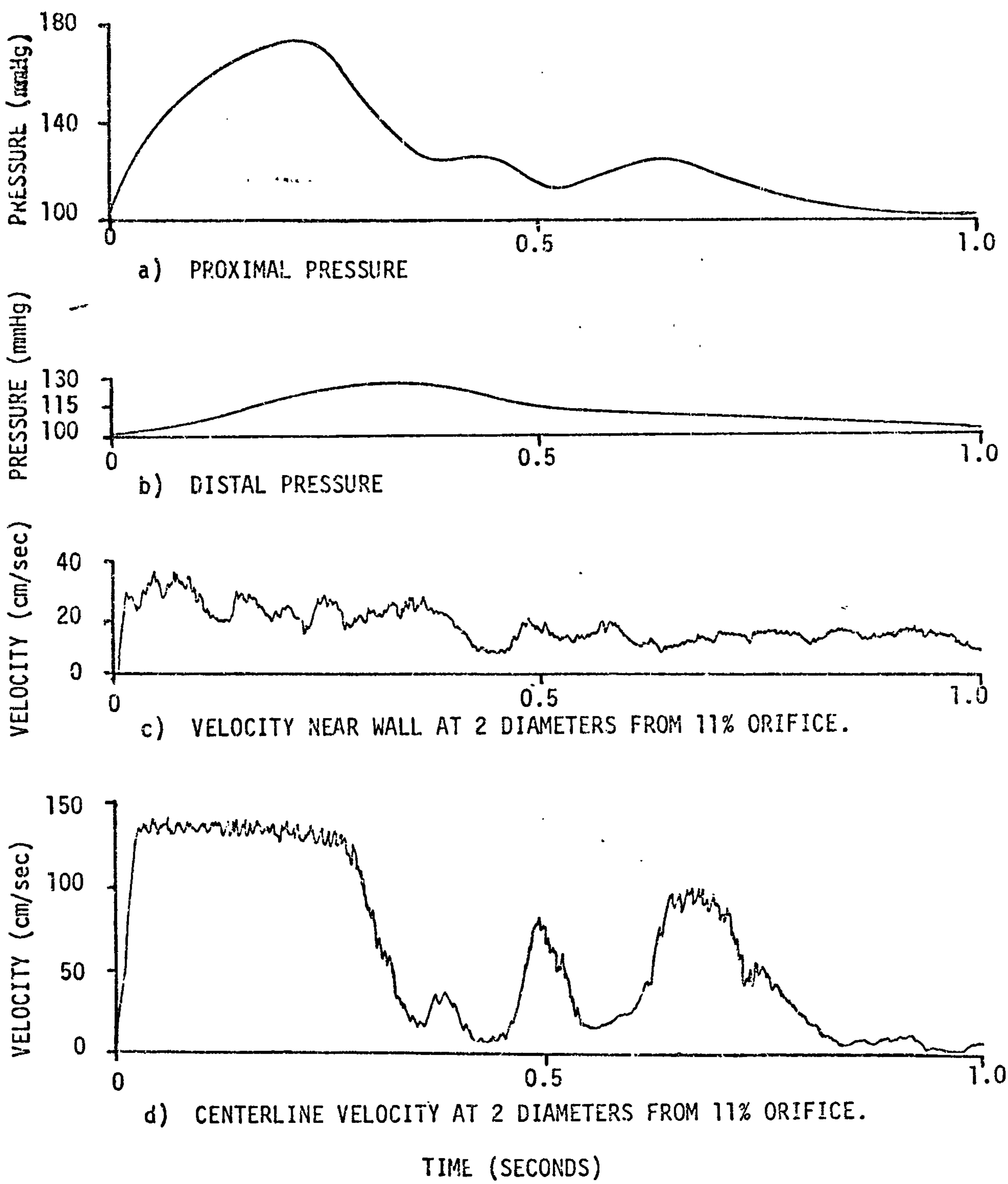

FIGURE IV.1 PRESSURE AND VELOCITY TIME HISTORIES FOR THE AXIAL AND RADIAL LOCATIONS DOWNSTREAM OF THE 11% ORIFICE.

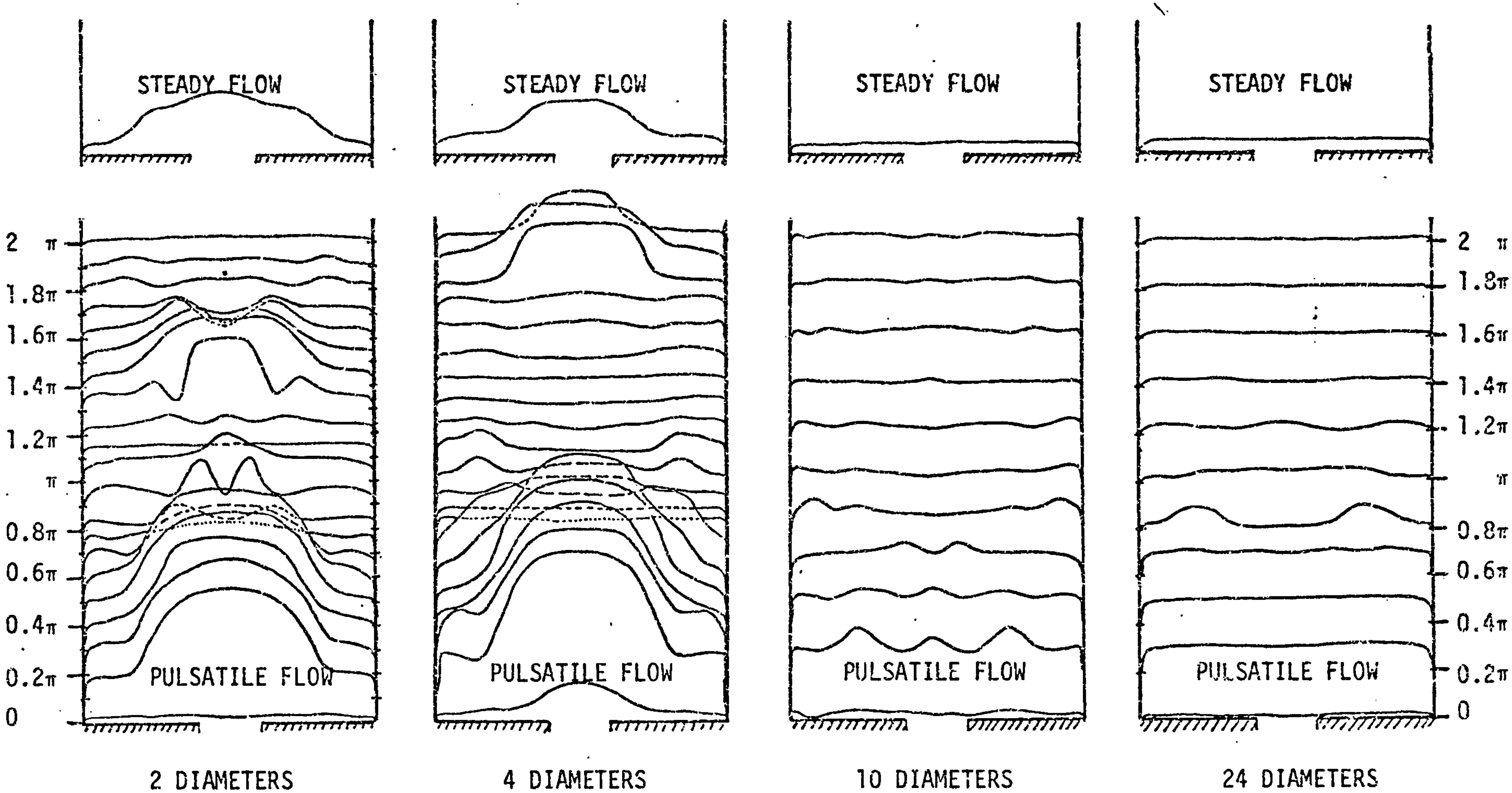

FIGURE IV.1 (e) TEMPORAL VELOCITY PROFILES DOWNSTREAM FROM THE 11% ORIFICE

4.3.1 Velocity Histories at a Select Point in the Flow

In addition to the pressure wave phase lags, there also is a lag associated with the velocity wave. It results from interaction of the jet with the surrounding fluid and from the pressure gradient reflection caused by the compliance simulator. Time delays were measured from the strip chart recordings using the initiation of the systolic pressure pulse as the reference point. Time delays in milliseconds and period phase lag in degrees are given for the velocity pulse measurements taken at the wall, and along the jet flow centerline. These measurements are presented in Table IV.2. These show a slight pulse delay the further the probe is moved downstream. At the two diameter profile, the pulse delay is slightly larger at the wall than at the centerline. This is probably because of a large scale disturbance such as a vortex ring initiated along the wall.

	Wall (ms)	ϕ^o (deg)	Centerline (ms)	ϕ^o (deg)
2 diameters	.9 ms	.32	.5 ms	.18
4 diameters	1.4 ms	.54	1.4 ms	.54
10 diameters	2.0 ms	.72	2.0 ms	.72
24 diameters	2.5 ms	.90	2.5 ms	.90

Table IV.2 Time lag of leading edge of velocity pulse as measured from leading ledge of proximal systolic pressure pulse.

4.3.2 Temporal Profiles

Figure IV.1 (e) shows the the time phased velocity profiles taken at 2, 4, 10, and 24 diameters downstream from the 11% orifice.

The orifice size is shown at the base of each figure. The ordinate is the phase time with 2π radians equal to one pulsatile period. The abscissa is the tube cross-sectional diameter.

4.3.2.1 Overall Observations

The profiles at two and four diameters are similar and show a relatively flat jet or potential core flow. The four diameter centerline velocity value peaks higher than that at two diameters because of the vena contracta which develops just behind the orifice. The velocity pulse width is smaller at four diameters resulting from the vena contracta, or large scale interactions with the quiescent pipe fluid. At the end of the systolic pulse, large scale flow disturbances form as a result of the sharp deceleration instability which occurs at the systolic pulse trailing edge. These large disturbances disappear rapidly as evidenced by the flat profiles beyond 0.8π radians.

4.3.2.2 Vortex Ring Presence

The expected vortex ring, located behind the orifice, does not appear to have sufficient time to develop completely during systole. The profile contours would exhibit significant buckling if the vortex ring had fully developed. The most obvious indication of its partial presence occurs near the end of systole, at four diameters, where the profile contour shows a significant large scale disturbance beyond the potential core. Macagno and Hung (1967) experimentally observed that the characteristic vortex ring does not form if the orifice flow is turbulent or highly disturbed. They observed flows at Reynolds numbers of 4500 which were both undisturbed and intentionally disturbed by a trip wire. Their photographed results suggest vortex ring formation attempts for the undisturbed cases, however, the trip pictures exhibited a highly disturbed flow outside of the jet with very little large scale organization. The Reynolds numbers for the profiles in Figure IV.1 are between 5800 and 6000 based upon orifice diameter. This suggests a very disturbed flow and tends to reduce the chances of vortex ring development in agreement with Macagno and Hung.

4.3.2.3 <u>Secondary Pulse</u>

A large secondary pulse is seen in both the two and four diameter profiles. The four diameter pulse lags the two diameter pulse by nearly $\pi/2$ radians. The secondary pulse is also seen in the proximal pressure profile and is virtually nonexistent in the distal profile. This secondary pulse results from loop simulation characteristics above the blockage. The most probable causes are wave reflection in the proximal compliance and reservoir simulator or ball valve seating characteristics in the pulsatile pump. The large secondary pulse is not seen for the orifice sizes greater than 11%. A compliant aorta exposed to the hypertensive pressures of 165/90 might also exhibit this phenomeon; however, it would be found in the diacrotic notch of the pressure wave. The diacrotic notch is present in all large arteries and results from similar compliant behavior. The pulse delay in the model results from the delayed reservoir response. The pulse occurs later at four diameters because of the low diastolic velocity washing of the disturbed flow and the flow loop reservoir compliance discussed above. Washing is the moving of the local disturbed flow by the mean fluid motion. In this case, the mean motion is the low speed diastolic jet. The washing effect at 10 cm/sec mean flow velocity at a separation of 1.5 cm between measurement stations could yield a $\pi/4$ radian lag.

4.3.2.4 Developed Flow

The velocity profiles at 10 and 24 diameters do not show evidence of the systolic jet or the secondary pulse. They are generally flat but show an order of magnitude increase during systole. The flat profile suggests a well mixed pipe flow rather than laminar behavior. Instantaneous Reynolds numbers for the jet flow are approxiamtely 4-5000 during systole and drop just below 2000 during diastole. The pipe Reynolds numbers remain at or below 2000, therefore, the main motion studied continues to maintain disturbed conditions.

4.3.2.5 Steady Flow

The steady flow profiles show some similarity to the systolic profiles. The steady state centerline velocities are about half of the comparable peak pulsatile flow systolic values. The profiles do show contour buckling which suggests that disturbances of relatively large wave length exist near the wall, however, it cannot be concluded that the vortex ring fully develops even for the steady cases. Reynolds numbers based upon orifice diameter values still exceed the laminar values and hence, the observations of Macogno and Hung are still revelant.

Profiles at 10 and 24 diameters exhibit flat contours as found in the pulsatile flow cases. At four diameters, the jet potential core is still well defined indicating that the steady flow jet may persist beyond the pulsatile jet. The pulsatile jet propogation is limited by the short systolic time interval and subsequent diastolic deceleration phase. These conditions do not occur in steady flow.

4.4 Comparison of the Measured Profiles to Flow Predictions

The measured velocity profiles are compared to the analytical cases reviewed in Chapter II. Discussions are presented for oscillatory pipe flow, steady flows and jet flows.

4.4.1 Oscillating Pipe Flow

The oscillating pipe flow profiles generated from equation 2.24 and those developed by Womerseley (1955b) exhibit significant phase lags and velocity gradient shifts near the wall. The boundary layer thickness varies with the square root of the viscosity and is therefore significantly reduced for water flow. The phase lag is predicted to be small or non-existent (equation 2.25) for low α values and vary inversely with the square root of viscosity for large α . The flow examined is characterized by low values of and hence, little or no phase lag is expected or observed. Velocity profiles based upon oscillatory pipe flow, as described by Uchida (1956) and Womerseley, are redrawn in Figure IV.2. These are compared to Figure IV.1 e). Flow reversal was not observed near the wall in the present work. This confirms Macagno and Hung (1967) observations that disturbed flow shows no vortex ring development for

orifice Reynolds numbers in excess of 4-5000. In the present work, a "positive" pressure gradient was maintained across the orifice at all times and hence a steady mean flow was effectively superimposed upon the velocity profile. Concave velocity profile segments appear at approximately r/4 from the wall of the end of systole and are indicative of an attempted flow reversal. This is also seen along the jet centerline at the end of systole where momentum deceleration occurs first.

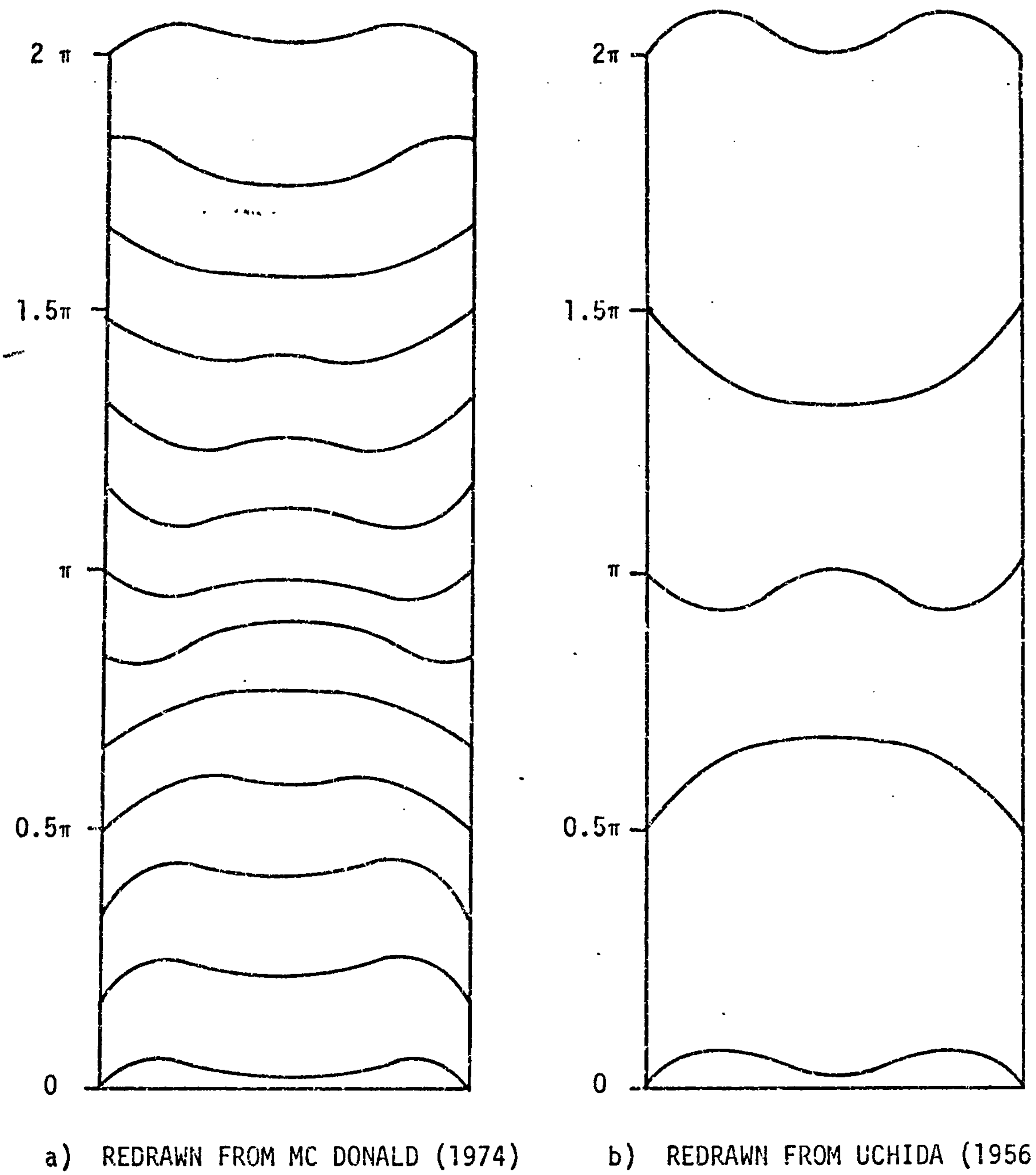

FIGURE IV.2 VELOCITY PROFILE PREDICTIONS FOR OSCILLATORY PIPE FLOW; REDRAWN FOR COMPARISON TO FIGURE IV.1 (e)

Except for the secondary pulse, a loop artifact significant only for the 11% orifice, the velocity profiles appear to behave as two steady flow conditions. The first occurs during the flat velocity phase in systole and the second occurs after the postsystole transient spike and continues through diastole (see Figures IV.1 (d) and IV.6).

4.4.2 Pipe and Orifice Flow

For steady pipe flow of a real fluid, the Bernoulli energy equation (equation 2.8) is usually adapted to describe flow field properties and hydraulic grade line decay. Friction losses can be estimated and orifice losses computed based upon steady flow fitted orifice coefficients. The adapted energy balance can be written as

$$E = \frac{V_1^2}{2g} + \frac{P_1}{\gamma} + h_1 = \frac{V_2^2}{2g} + \frac{P_2}{\gamma} + h_2 + H_o + H_f, \qquad (4.1)$$

where H_o is the head loss because of the presence of the orifice, H_f is the energy loss because of pipe friction, and E is the total energy per unit weight of the fluid in the flow field. The orifice head loss is usually expressed as (Vennard, 1963)

$$H_o = \left[\left(\frac{1}{C_v^2} - 1\right)\left(1 - \frac{A_o^2}{A_1^2}\right)\right] \frac{V_o^2}{2g}, \qquad (4.2)$$

where C_v is an orifice coefficient used to express head loss and is related to the orifice coefficient in equation 2.45 by

$$C = \frac{C_v}{\sqrt{1 - \left(\frac{A_o}{A_1}\right)^2}}. \qquad (4.3)$$

Values of C_v were selected as 0.92, 0.85, 0.89, and 0.85 for the 11, 20, 30, and 50% orifice sizes. The values were determined by fitting the steady flow data to equation 4.1. The values are well within Vennard's (1963) suggested range of 0.8 to 0.98.

The energy loss resulting from pipe friction is usually expressed as,

$$H_f = \lambda \frac{L}{d} \frac{U^2}{2g} , \tag{4.4}$$

where L is the tube length and λ is the friction coefficient. For Reynolds numbers between 1000 and 10,000, the friction coefficient for smooth and rough pipes varies between 0.03 and 0.04. This work assumes a value equal to 0.035. For the loop setup l/d is approximately equal to 60.

To evaluate the friction energy loss, the mean velocity of the tube is used. This is reasonable since the jet effect is negligible beyond 10 orifice diameters downstream. To evaluate the orifice energy loss, the mean velocity through the orifice is also used. The mean velocity of the tube, both before the orifice and beyond ten diameters downstream, can be considered equal based upon the distal velocity profile contours. There is no difference in elevation since all runs were made in the horizontal position. The result of these assumptions is that the contribution of the pressure differential is offset by the orifice and friction losses as

$$E_1 - E_2 = H_o + H_f . \tag{4.5}$$

The hydraulic grade line losses have been computed for selected flow conditions. The results are shown in Figure IV.3 for the 11, 20, 30,and 50% orifices. The energy losses for the steady flow cases appear to account for the energy difference between the pressure measurement points for the steady flow cases. As the velocity increases, the energy loss caused by the orifice increases as the square of the mean orifice velocity. The pulsatile flow cases do not balance energy in the same manner as steady flow. The residual energy value shown on the right hand side of the Figure IV.3 profiles is the loss which is unaccounted by equations 4.1, 4.2, and 4.4. The residual value is probably the result of unaccounted turbulent energy losses and errors in estimating the pulsatile orifice coefficient from the steady flow cases. The steady flow orifice coefficients vary as a function of orifice shape and Reynolds numbers. Small errors in orifice coefficient selection can yield large errors in head loss computations. The friction losses are small for all orifice sizes. The magnitude of the friction loss approximates that of the orifice loss for the larger 30 and 50% orifice sizes.

Most of the energy loss for the small stenosis sizes results from the orifice head losses. These orifices represent the severe stenoses which require surgical correction. If the small friction losses are ignored then the mean pressure differential can be plotted as a function of flow rate for each orifice size (Figure IV.3 (e)). The small orifice curves exhibit a u^2 type behavior. Large orifice flows behave more as a function of wall friction flow as might well be expected.

4.4.3 Jet Flow

Jet flow comparisons are made by relating the measured jet growth and centerline velocity decay profiles to those that would be predicted based either upon recorded experimental data such as Abramovich (1963) or by the relationshp developed in Chapter II for the round jet.

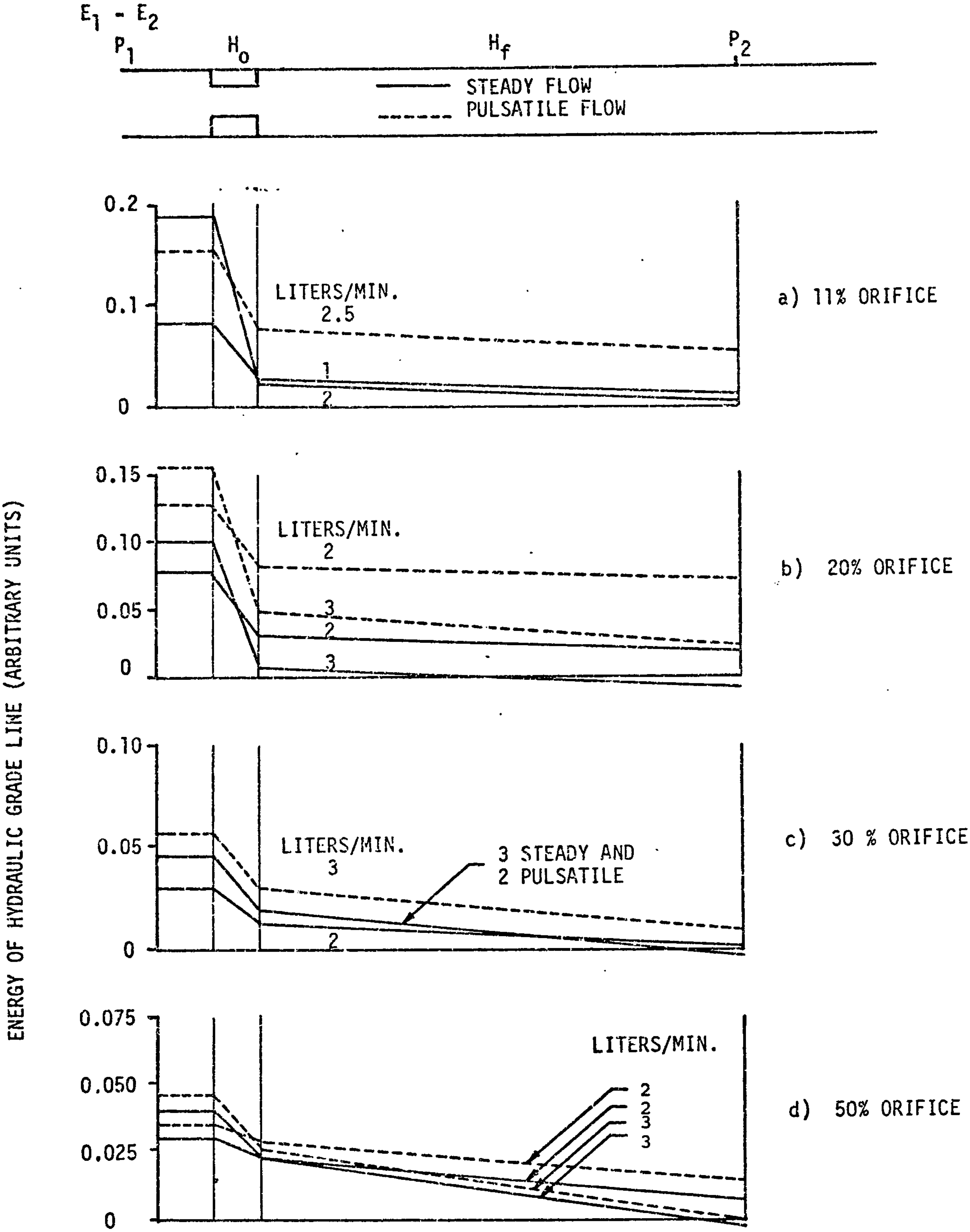

FIGURE IV.3 ENERGY LOSSES CAUSED BY ORIFICE LOSS AND WALL FRICTION FOR 11, 20, 30, and 50% ORIFICES (DATA PLOTTED IN ARBITRARY UNITS) AND DELTA MEAN PRESSURE TO FLOW RATE PROFILES FOR THE SAME ORIFICE SIZES.

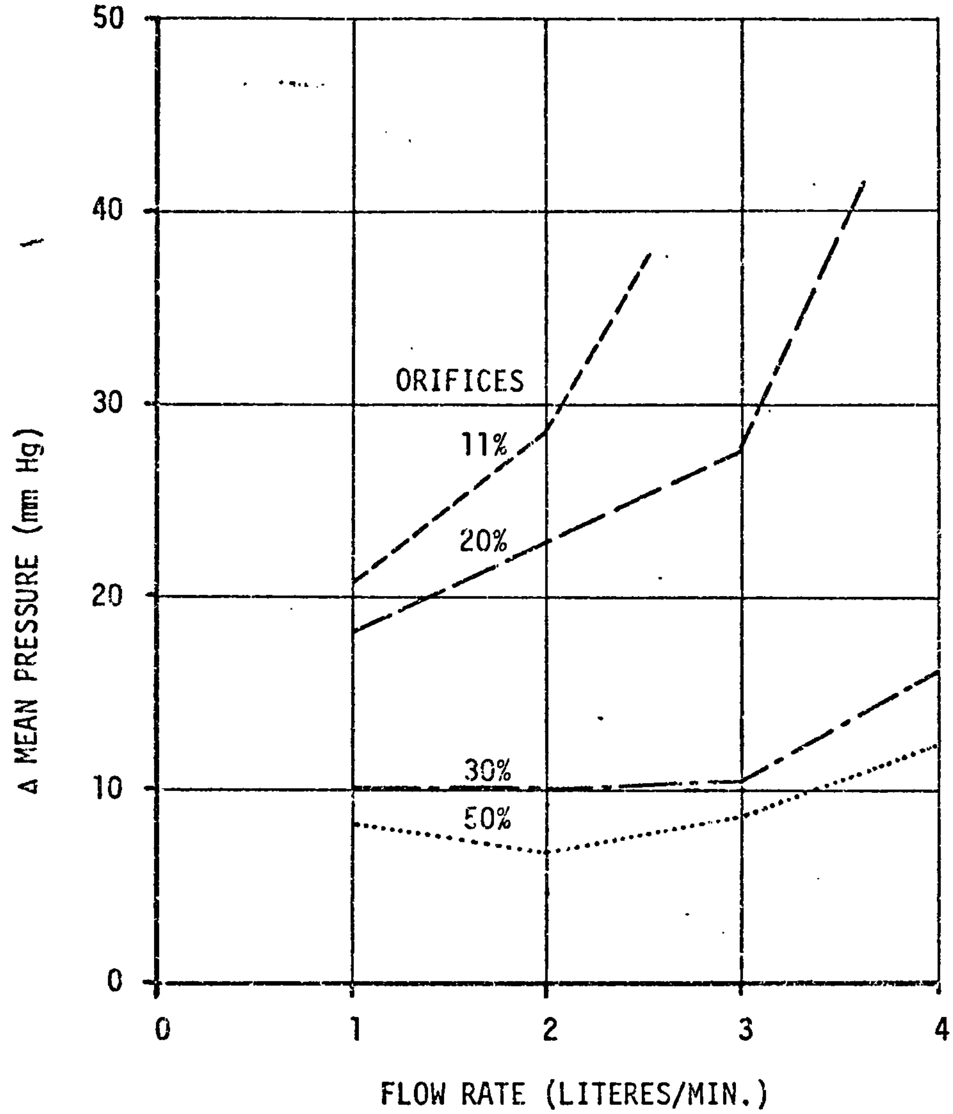

FIGURE IV.3 e) DELTA MEAN PRESSURE VERSUS FLOW RATE FOR 11, 20, 30, AND 50% ORIFICES

The centerline velocity of a submerged jet has been observed to decay inversely with the distance from the jet nozzle or orifice. By regrouping equation 2.42, we obtain

$$u = \frac{K}{x} , \tag{4.6}$$

where $$K = \frac{3J}{8\pi\mu} \frac{1}{(1 + \frac{1}{4} e^2)^{\frac{1}{2}}} . \tag{4.7}$$

All terms in K are assumed constant. It should be noted that e does contain a further dependence upon x, but at r = 0, along the centerline, e = 0, and equation 4.6 applies.

Figure IV.4 shows centerline velocity data, obtained from Table IV.1, plotted as a function of distance from the orifice. The distance has been presented in centimeters, obtained by converting the downstream diameter data with the appropriate orifice diameter correction. The constant K has been evaluated for the 11% orifice. Assuming a mean jet velocity of 100 cm/sec, K is approximately equal to 190 cm^2/sec.

There is a very good relationship between the measured and the pre-predicted decay. This close agreement suggests that during systole, the flow approximates a steady flow jet. The centerline velocity at four diameters from the orifice is elevated. This probably results from the vena contracta effect observed earlier and significant error in use of equation 4.7 to evaluate K. K will actually exhibit a wall dependence as seen in equation 2.42 and 2..44. The decay process initiation point moves downstream at least 2-4 diameters.

Abramovich (1963), in reviewing jet flow data from several authors, has observed that the width of the jet grows linearly with distance from the orifice. Schlichting (1968) deduced the same relationship from order of magnitude arguments and mixing length assumptions. The relationship applies to submerged jet flow. Abromovich developed geometric relationships for the jet profile and shows that the jet boundary should expand at approximately 8^{o} 21' measured from the orifice outside edge with respect to the axial flow direction. Because of the wall effect that is certainly present in pipe flow, it is useful to examine the spread of the velocity profile where the point velocity is equal to one-half of the maximum centerline velocity. This assumption implies that the radial velocity decay is linear for the comparison to be valid. Equations 2.42 and 2.43 show that this is not true. However, the velocities should be relatively large and may be linearly approximated down to 20 or 30 cm/sec with little loss of accuracy. With these assumptions, Figure IV.5 shows the half velocity.

It cannot be concluded that the experimental half velocity jet boundary growth is linear, however, the effect of the presence of the pipe boundary can be observed. The normal submerged jet width would have grown more rapidly. It is normally fed by fluid entrainment from the surroundings. The surroundings in this case are not as cooperative for jet growth, thus fluid entrainment is significantly limited or nonexistant. If entrainment were occurring, significant backflow would have been observed in the distal velocity profiles, which was not the case. The result is that the contained pulsatile systolic jet width grows slower than steady submerged jet width growth. The jet becomes totally involved with the surrounding fluid between four and ten diameters downstream from the orifice. This is intuitively obvious from the temporal profiles, however, and is graphically shown in Figure IV.5.

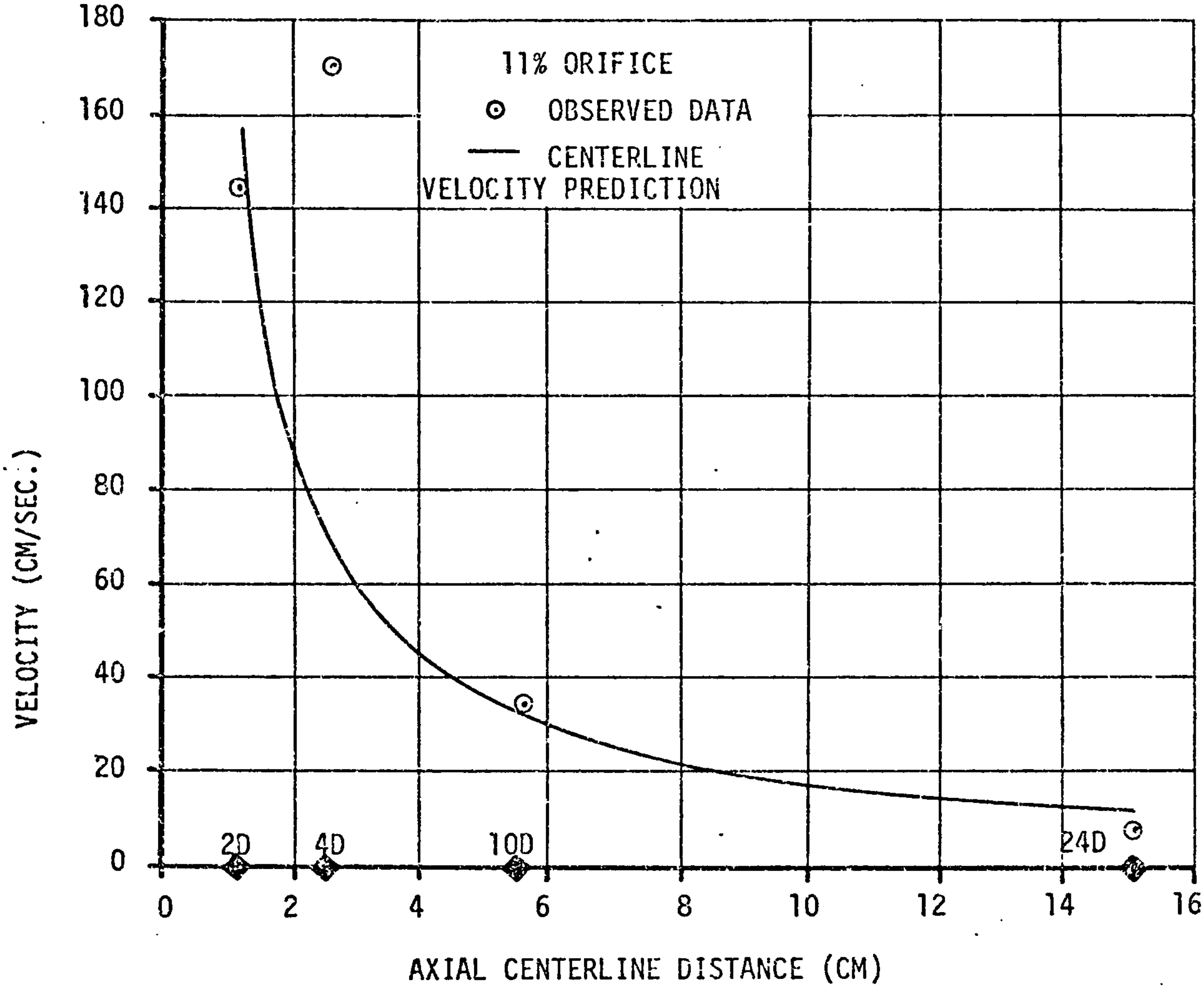

FIGURE IV.4 CENTERLINE VELOCITY COMPARED TO JET PREDICTED DECAY

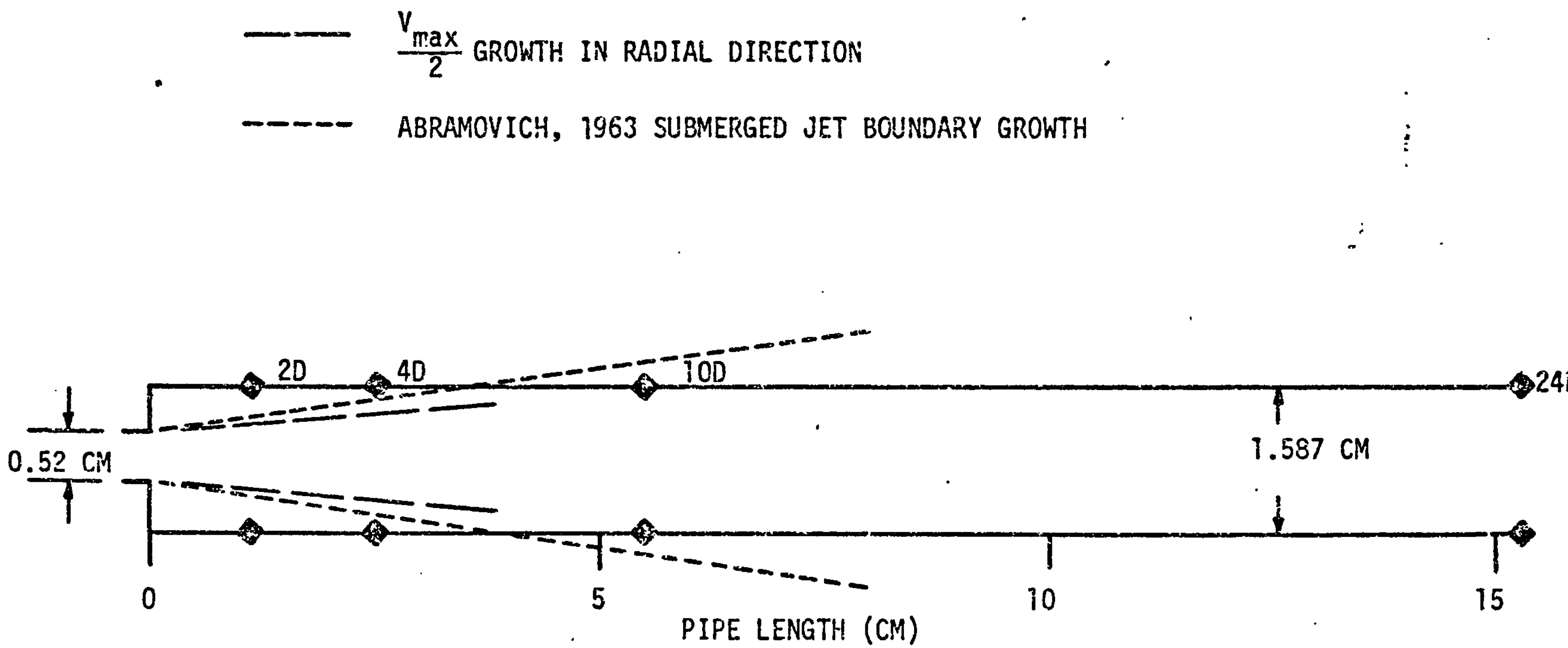

FIGURE IV.5 GROWTH OF PROFILE POINT CORRESPONDING TO $\frac{V_{max}}{2}$ FOR DISTAL STENOSIS FLOW FROM 11% ORIFICE COMPARED TO ABRAMOVICH SUBMERGED JET BOUNDARY GROWTH PREDICTIONS.

4.5 Frequency Analysis

Power spectral densities were computed for selected velocity data segments as indicated in Table IV.1. Only select portions of each run were analyzed. The data selection criteria is discussed below. Observations are made with respect to the power decay laws or observations of -1, -5/3, and -7 ranges discussed in Chapter II.

4.5.1 Data Selection

Runs were selected for frequency analysis to study two basic phenomena: (1) changes to the power spectral density shape resulting from changes in position, phase, and pulse shape and (2) to investigate the Reynolds number Strouhal number relationship for the quasi steady flow cases.

For each pulsatile run, the pulsatile pump repeated the same pressure wave from beat-to-beat. Power spectral density destributions were calculated for several systolic velocity pulses in the same run sequence. The frequency spectrums showed negligible change from pulse-to-pulse. This results from the repetitive nature of the pump electronic control system and would not directly apply to physiological cases where heart rates change easily under many influences.

The velocity history data suggested that two quasi steady state conditions occured during each cycle: (1) a relatively flat systolic pulse phase and (2) a flat diastolic phase. Typical velocity records are shown in Figure IV.6. The frequency content of the transition curve from systole to distole obviously contains many Fourier transform components to describe the short acceleration and deceleration phases. If these transition periods are deleted from the analysis, then it remains only to verify that the two phases do, in fact, take on a quasi

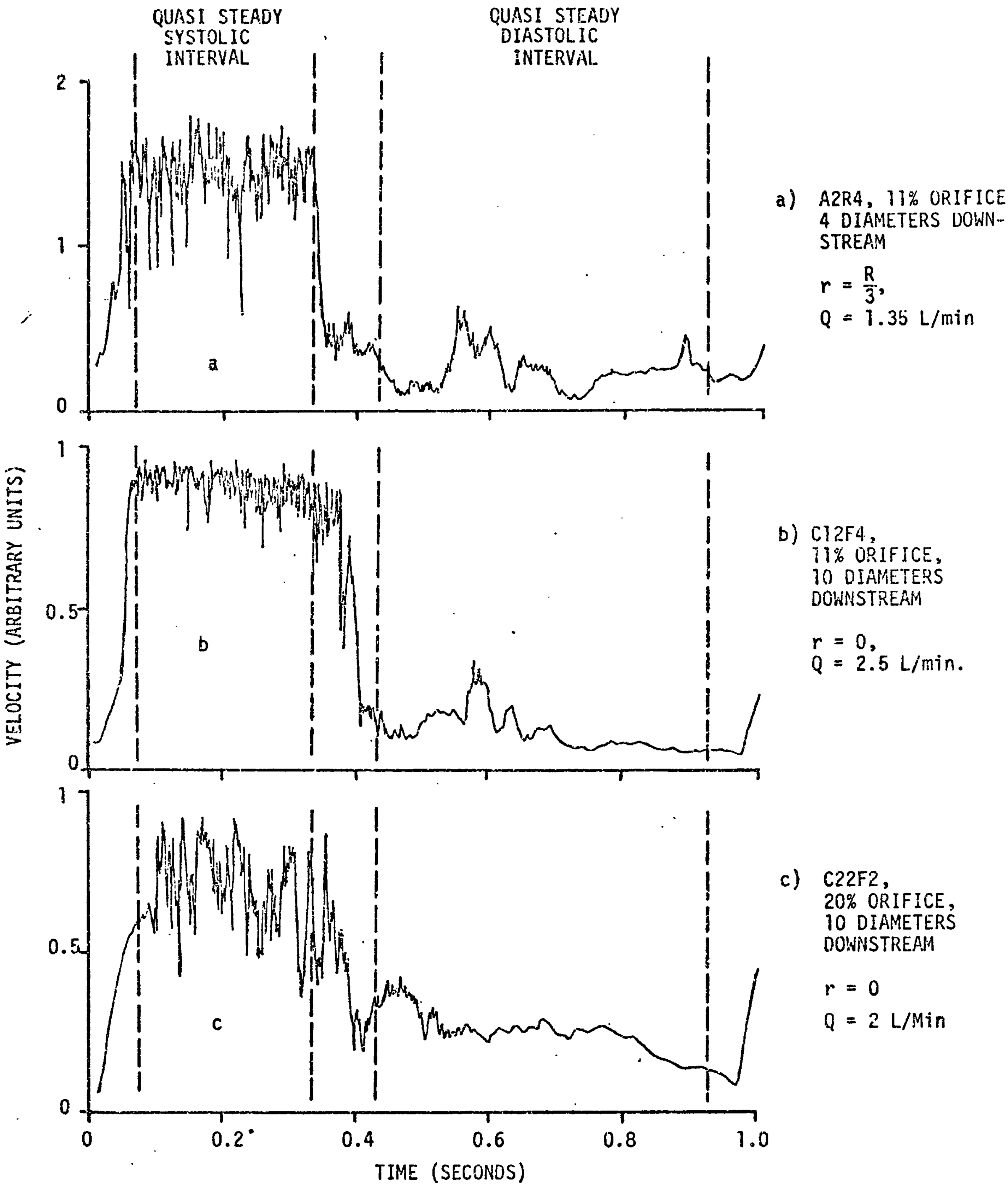

FIGURE IV.6 TYPICAL VELOCITY HISTORY RECORDS SHOWING QUASI STEADY STATE CONDITIONS DURING SYSTOLE AND DIASTOLE.

steady state nature. This comparison was made by slicing the systolic and diastolic intervals of several pulses into five segments and computing their appropriate power spectral densities. Indeed, negligible differences were found in frequency content from one portion of the flat systolic pulse to the next. The same was also found to be true of the diastolic segment. It is possible to conclude that the cycle can be represented by two quasi steady flow conditions. This result is not too surprising if we examine the process which takes place during the quasi steady state times. The selected systolic segment occurs while the pressure pulse value approaches, reaches and passes its peak. The pressure pulse magnitude changes very little during this period, probably less than ten percent, and thus the fluid acceleration and deceleration values are minimal. Hussain and Ramjee (1975, 1976) have also shown that the vortex shedding frequency does not change under small pressure fluctuations. This is confirmed in the observed frequency analysis. There is, however, a very large shift in energy frequency content between systole and disatole which, therefore, shows that Hussian and Ramjee's findings cannot be extrapolated to large pulse variations.

To support these observations, data samples have been included in Figures IV.7 through IV.9. Figure IV.7 shows the phase-to-phase differences for three pulses in the same run sequence. Figure IV.8 shows the power spectral density function for five segments of the same systolic pulse. Figure IV.9 shows power spectral density curves for the systolic and diastolic phases for the same pulse cycle. The power spectral density magnitude and decay slopes are virtually identical in all cases.

4.5.2 Distal Profile Frequency Observations

The power spectral density distribution for the points along the 2 and 4 diameter profiles of the 11% orifice are very similar. The systolic frequency distributions all show a convex profile which falls off rapidly between 100 and 200 Hz. Systolic rolloff starts near the wall and decays rapidly near 200 Hz. The distolic phase, on the other hand, exhibits a constantly decreasing power spectral distribution over the entire frequency range.

The systolic phase exhibits a broad segment of -1 slope indicating large scale vorticity production caused by interaction with the main stream. There are no obvious -7 slopes; however, after the -1 slope segment, all slopes get increasingly steeper which indicates that energy is being transferred to the smaller eddy sizes (-5/3 law) and some form of small scale dissipation is coming into play. Figures IV.10 and IV.11 show the systolic and diastolic changes along the 2 diameter velocity profile. The -1 slope can be seen in the systolic profiles, but is not present in the diastolic profiles. This seems to indicate that dissipation is in progress over a wide frequency or wave length range during diastole.

At 10 and 24 diameters downstream from the orifice, the systolic and diastolic profiles begin to show similarities. The systolic profiles no longer exhibit a significant -1 slope. It appears that energy decays over a broad frequency range during systole. Changes are no longer as pronounced in moving from the wall to the centerline. A viscous dissipation slope, -7, can be seen in the diastolic profiles. Figures IV.12 and IV.13 summarize these observations for the 24 diameter profile.

Steady flow profiles were developed as a comparison to the pulsatile frequency analysis results. The steady flow results do not approximate either the systolic phase or the diastolic phase pulsatile analyses. This is largely because of the wide variation in typical velocity values which occur for each pulse. At 4 diameters, the pulsatile centerline velocity is approximately 170 cm/sec during systole and 15 cm/sec during diastole. The comparable value is approximately 70 cm/sec for the steady flow case. The steady flow profiles do exhibit the -5/3 power law, typical of the inertial subrange. It is concluded that the inertial subrange development requires a finite time to become fully developed. It does not fully develop during most of the pulsatile cycles examined in this work. Figure IV.14 shows the steady flow power spectral density functions for 4 diameters from the orifice. Notice that the jet shape continues to persist as evidenced by the rapid power decay present near the wall.

4.5.3 Orifice Size and Flow Rate Variations

The orifice size and flow rate variations produced systolic phase results that are consistent with steady flow observations and Strouhal number realtionships. As the flow rate increased from one liter per minute to four liters per minute, the knee of the systolic phase power spectral density function moved from left to right, or to higher frequencies, resulting in a wider frequency range of -1 slope. As the orifice size was increased from 11% to 50%, the knee of the curve reversed direction and moved to the left or toward the lower frequency levels. The -1 slope is virtually lost at the large size orifices. Figures IV.14 and IV.15 summarize these observations.

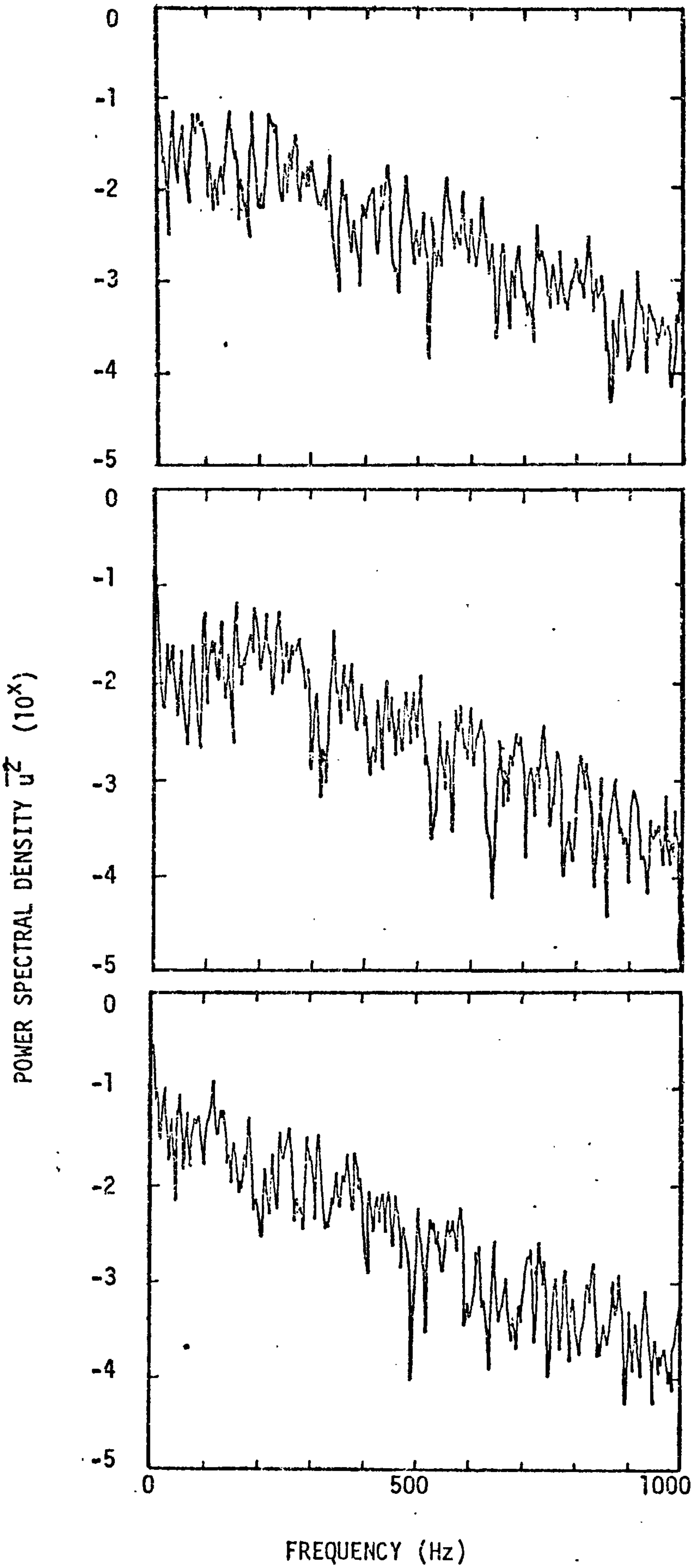

FIGURE IV.7 PULSE-TO-PULSE PHASE COMPARISON FOR THREE PULSES IN THE SAME RUN SEQUENCE (A1R6)

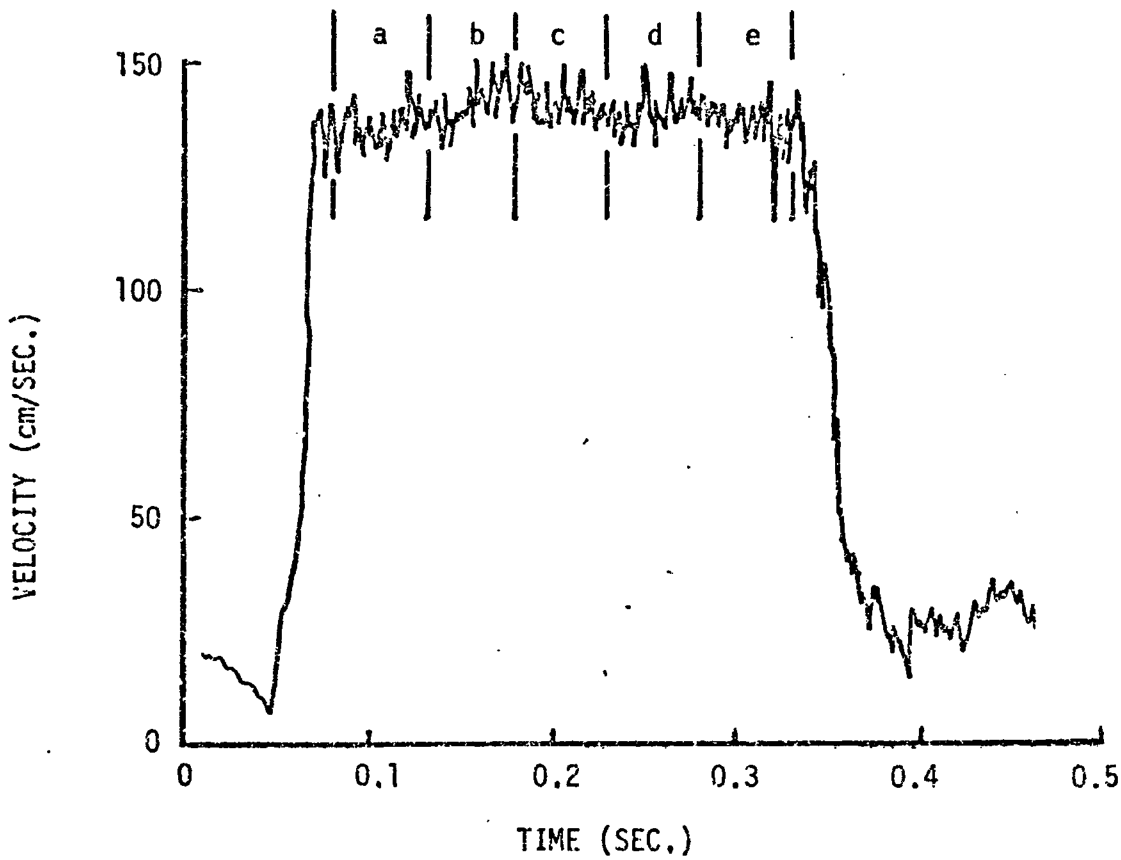

FIGURE IV.8 WITHIN PULSE PHASE COMPARISON OF POWER SPECTRAL DENSITY FUNCTION FOR FIVE CONSECUTIVE SEGMENTS FROM THE SAME SYSTOLIC VELOCITY PULSE.

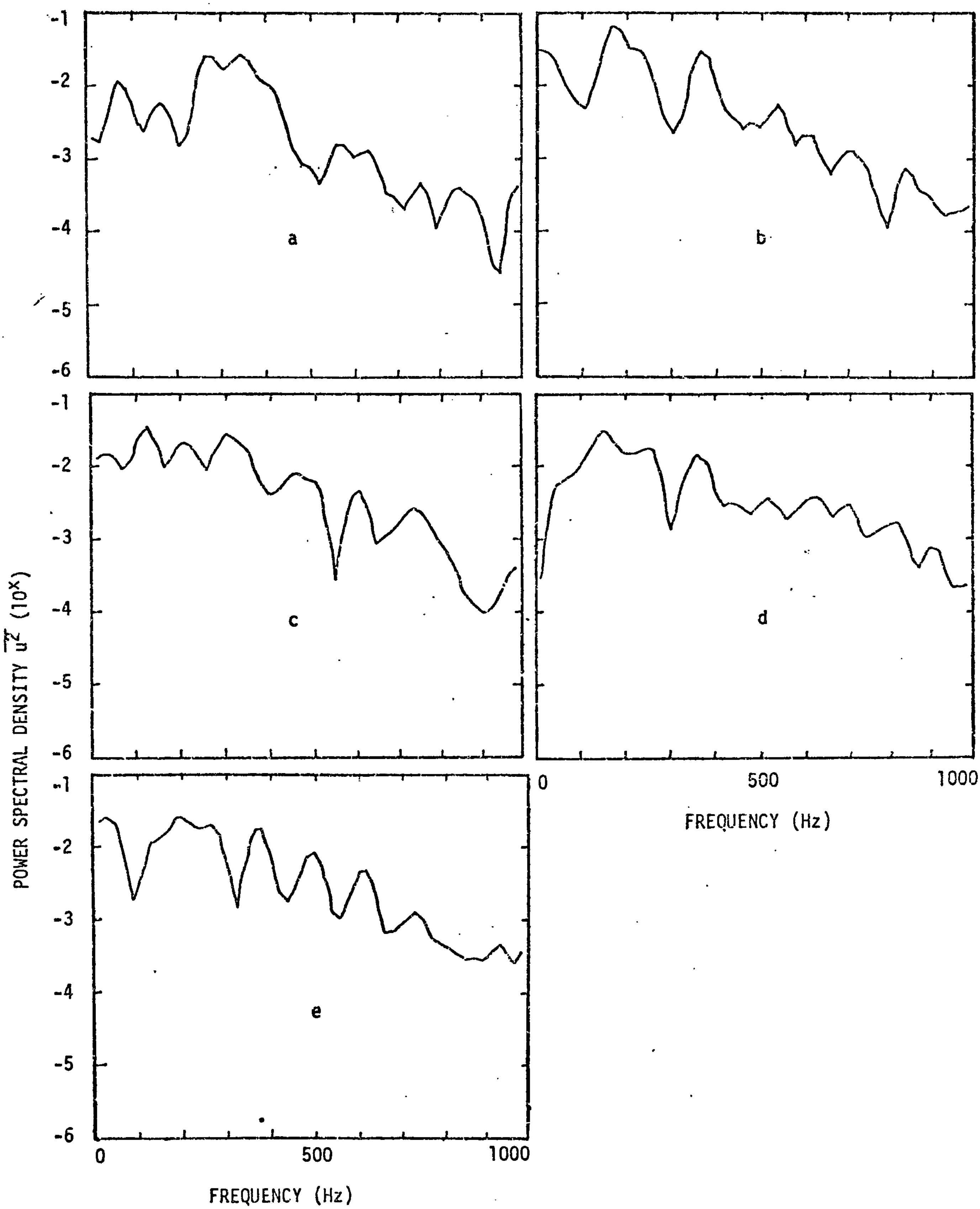

FIGURE IV.8 (CONTINUED)

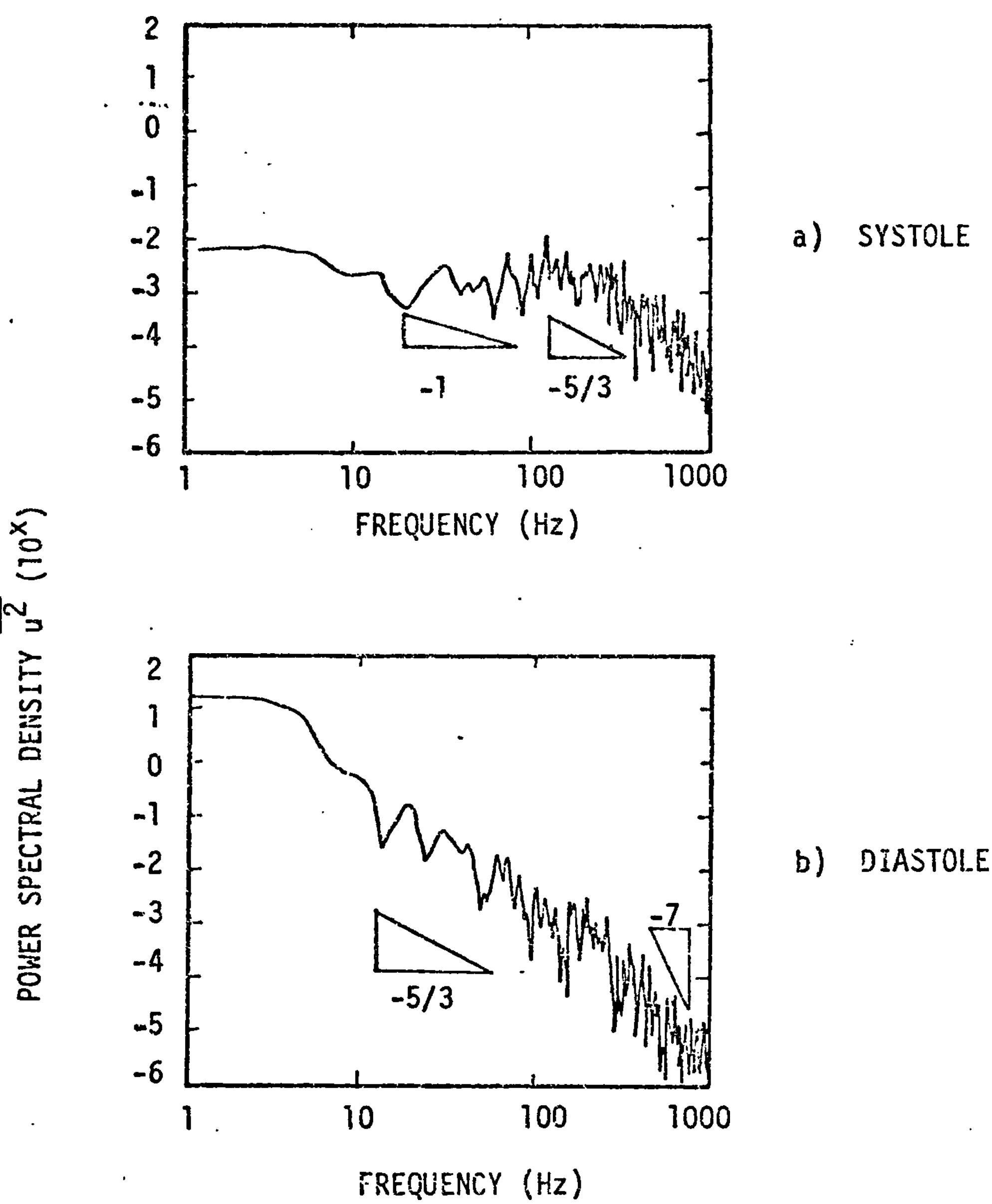

FIGURE IV.9 SYSTOLIC AND DIASTOLIC QUASI STEADY FLOW CONDITIONS FOR 4 DIAMETER CENTERLINE VELOCITY CASE (11% ORIFICE).

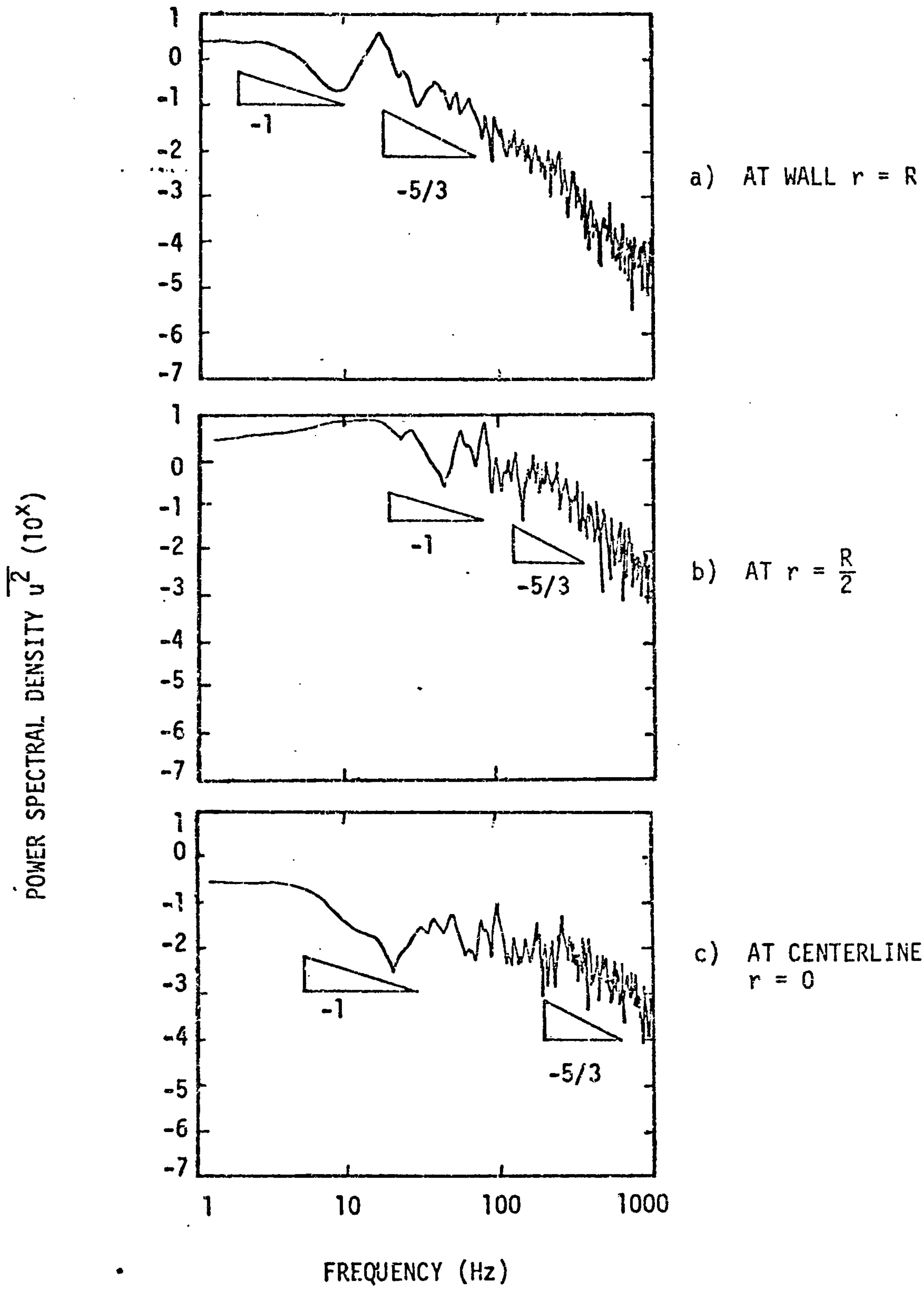

FIGURE IV.10 SYSTOLIC PHASE POWER SPECTRAL DENSITY DISTRIBUTION ALONG THE CROSS SECTION AT 2 DIAMETERS DOWNSTREAM FROM THE 11% ORIFICE.

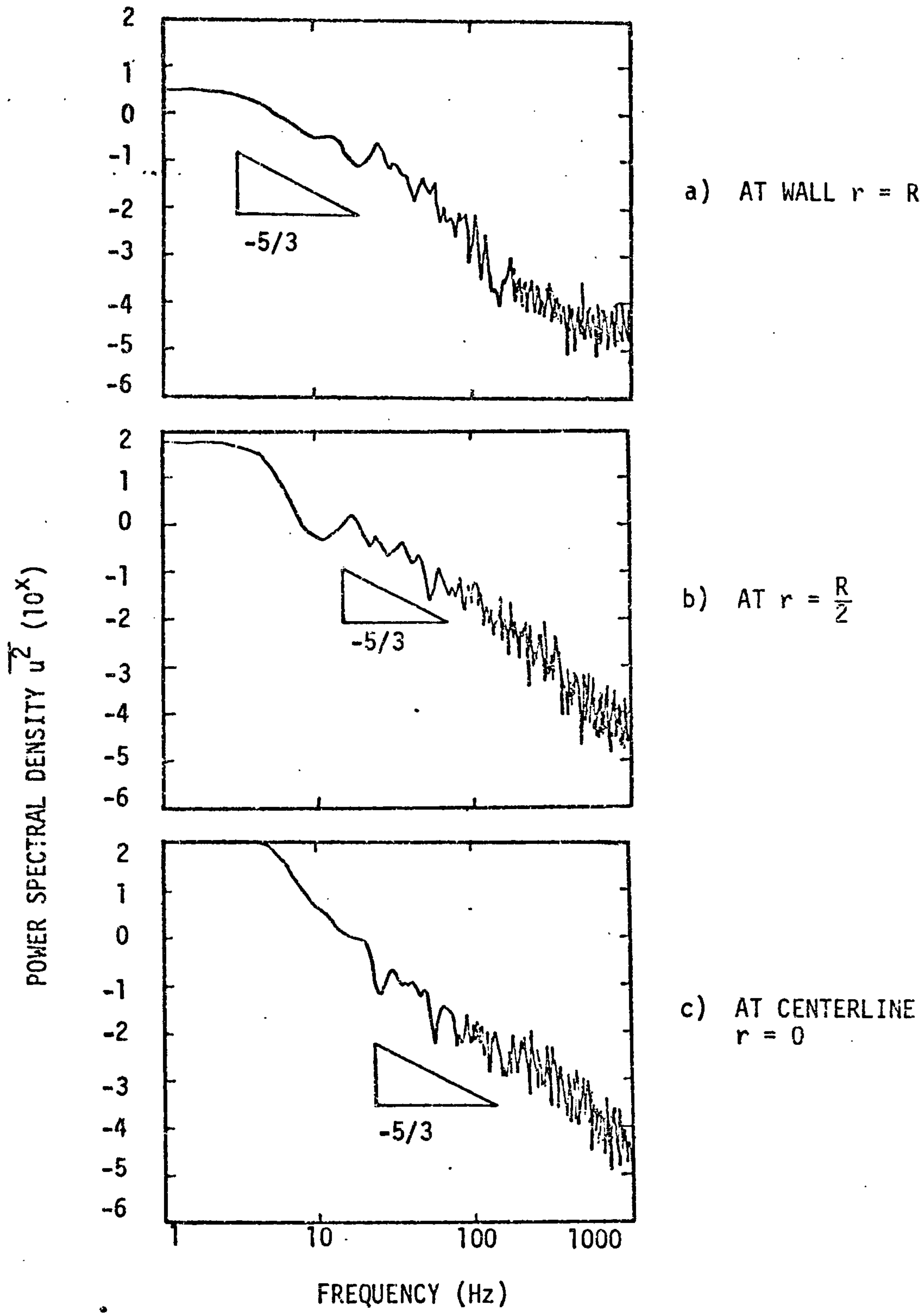

FIGURE IV.11 DIASTOLIC PHASE POWER SPECTRAL DENSITY DISTRIBUTION ALONG THE CROSS SECTION AT 2 DIAMETERS FROM THE 11% ORIFICE.

The Strouhal number, equation 2.50, has been evaluated for orifice flow by Anderson (1956), Beavers and Wilson (1970), and Becker and Massaro (1968). Anderson, and Beavers and Wilson suggest a Strouhal value of .63 and Becker and Massaro suggest a value "near 1/2." The .63 value has been used in Table IV.3 to predict the vortex shedding frequency. According to Anderson's observations, the vortex shedding frequency should correspond to the highest vortex shedding frequency, which is usually measured near the orifice. From the power spectral density functions, this frequency is located by intersecting the -1 slope portion of the profile with the energy cascade slope (-5/3). The decay mechanism may not be entirely clear, but the high frequency end of the -1 slope should be an indication of vorticity production resulting from interaction with the main stream (Tchen, 1947). The agreement in Table IV.3 is very good and again confirms the assumption of a quasi steady flow condition during most of the systolic phase.

Several authors (Bruns, 1959, 1964; Anderson, 1956; Butterworth and Reppert, 1966; Powell, 1964; and Spencer et al, 1958) have postulated and observed that the sound production in a distributed or jet flow is directly related to the frequencies of the shedding vortices. If this is true, then it should be possible to predict the orifice size and jet velocity for flow blockages similar to those studied here. A phonocardiogram recording could be made at or just distal to a stenosis blockage (point of greatest sound intensity). A power spectral density could then be computed for the systolic phase (using the electrocardiogram as a trigger) and the knee frequency could be determined by visual inspection. From the Strouhal relationship, the diameter to velocity ratio could then be found. By entering a set of curves similar to those in Figure IV.3 (e), with the delta mean pressure (which can be obtained from brachial and femoral blood pressure measurements), a value for velocity and orifice diameter can be estimated. The velocity would represent the flow through the blockage and the diameter would be indicative of the mean stenosis lumen diameter.

Orifice Size	Flow Rate	Predicted Max Vorticity Production Freq. (St =.63)	Observerved Max Production Frequency
11%	1.0	93	100
	1.5	139	175
	2.0	186	210
	2.5	232	250
20%	1.0	39	50
	2.0	73	60
	3.0	108	80
	4.0	126	110
30%	1.0	20	30
	2.0	40	40

Table IV.3 Comparisons of maximum frequency characterized by the -1 slope of vorticity production obtained from observed data and Strouhal number predictions.

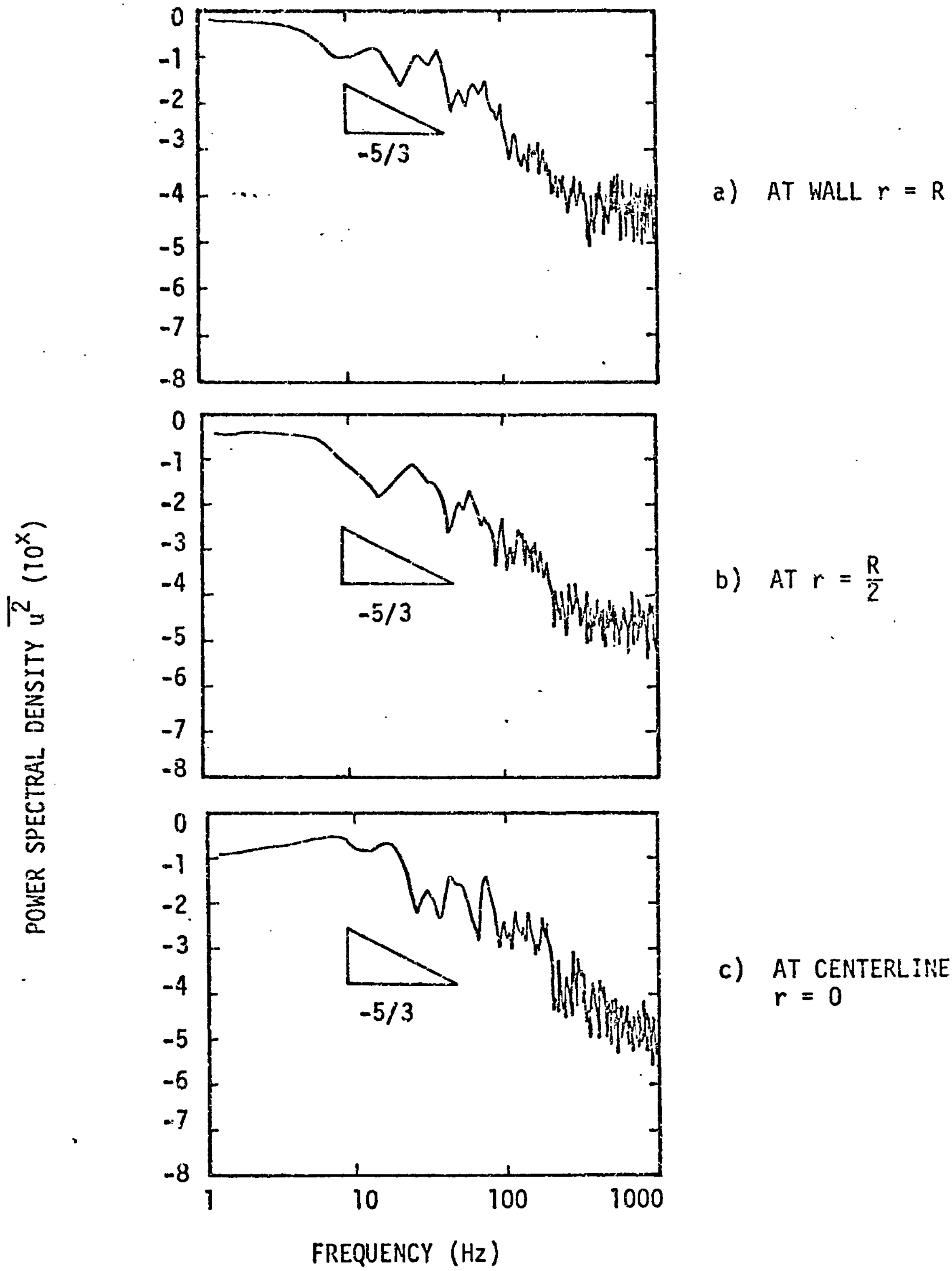

FIGURE IV.12 SYSTOLIC PHASE POWER SPECTRAL DENSITY DISTRIBUTION ALONG A CROSS SECTION AT 24 DIAMETERS FROM THE 11% ORIFICE.

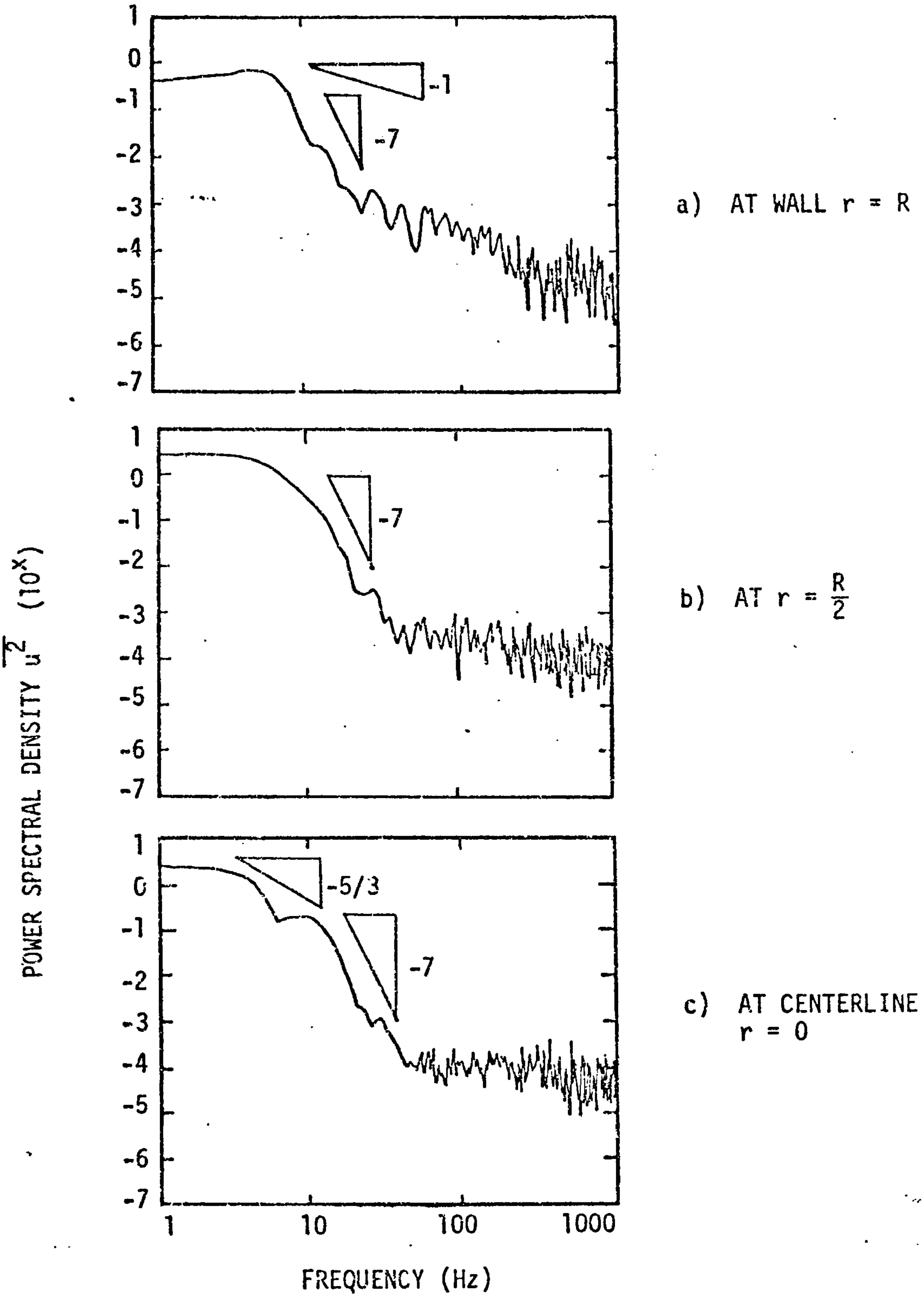

FIGURE IV.13 DIASTOLIC PHASE POWER SPECTRAL DENSITY DISTRIBUTION ALONG A CROSS SECTION AT 24 DIAMETERS FROM THE 11% ORIFICE.

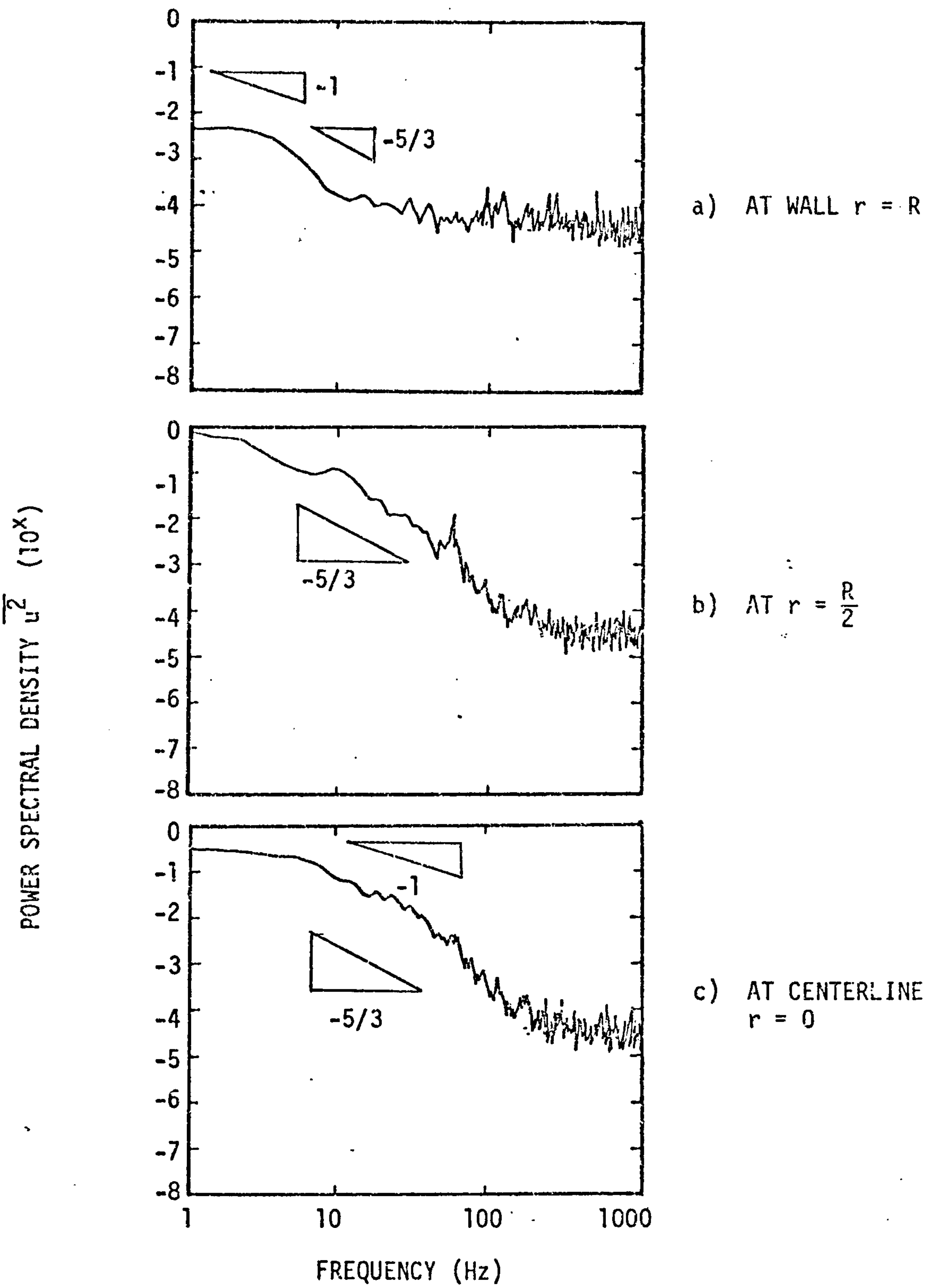

FIGURE IV.14 STEADY FLOW POWER SPECTRAL DENSITY DISTRIBUTION ALONG A CROSS SECTION AT 4 DIAMETERS FROM THE 11% ORIFICE.

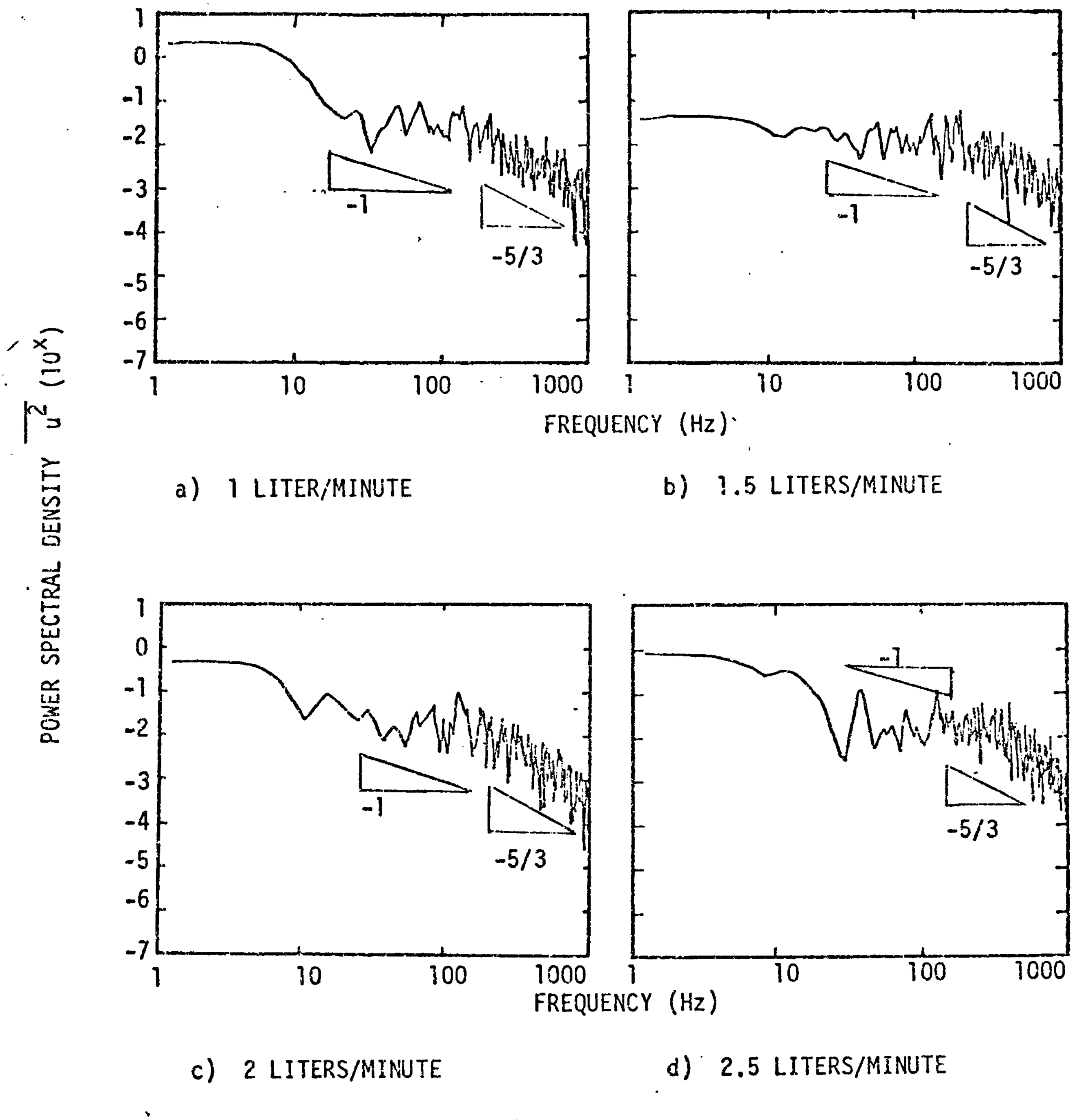

FIGURE IV.15 SYSTOLIC PHASE POWER SPECTRAL DENSITY DISTRIBUTION AT THE CENTERLINE 10 DIAMETERS DOWNSTREAM FROM THE 11% ORIFICE FOR FLOW RATES OF 1, 1.5, 2, AND 2.5 LITERS PER MINUTE.

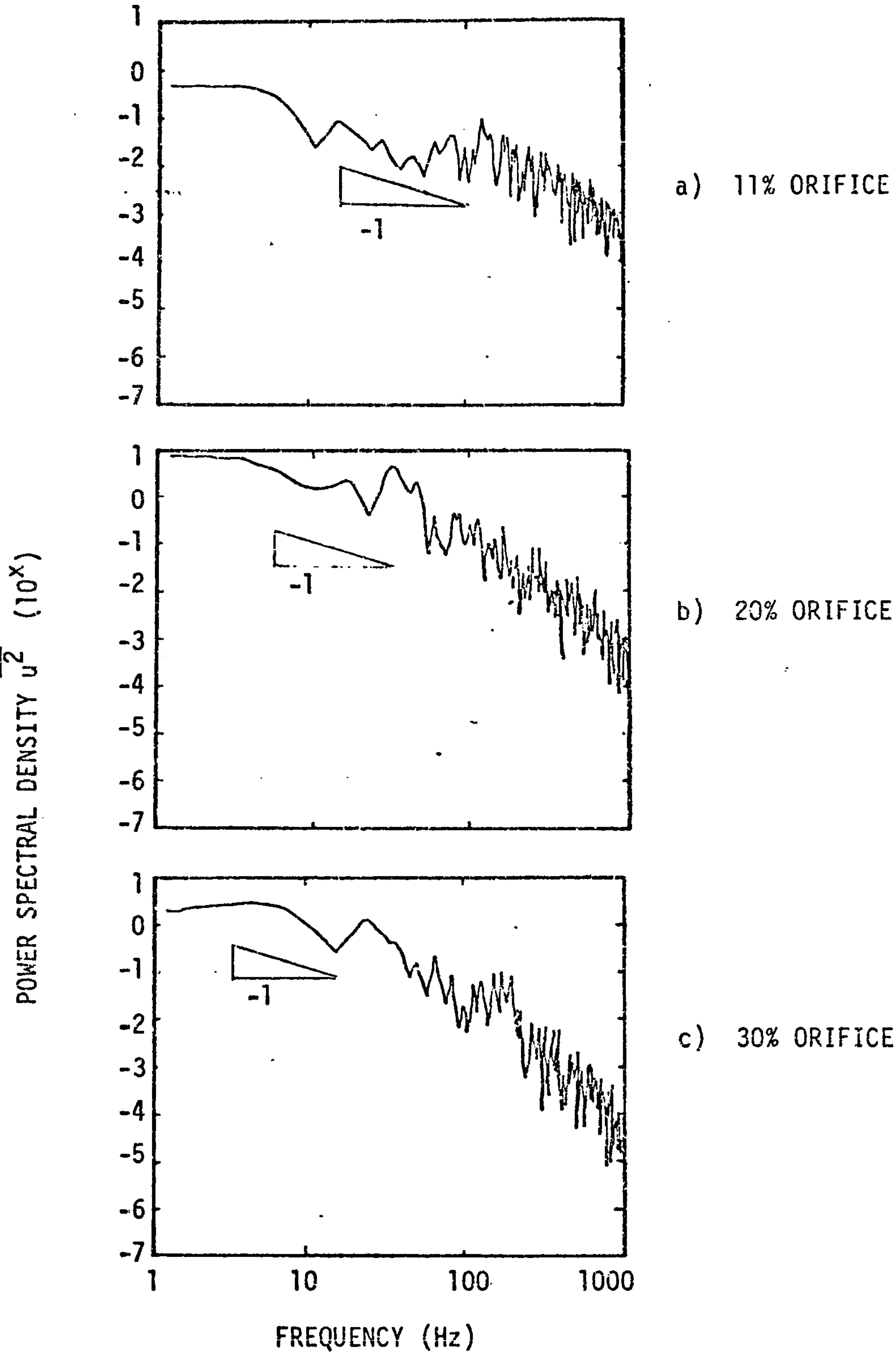

FIGURE IV.16 SYSTOLIC PHASE POWER SPECTRAL DISTRIBUTION AT THE CENTERLINE 10 DIAMETERS FROM THE 11, 20, AND 30% ORIFICES AT 2 LITERS PER MINUTE.

CHAPTER V

SUMMARY AND RECOMMENDATIONS

5.1 Summary and Conclusions

A set of plexiglass arterial stenosis models were placed in a pulsatile mock circulation loop and pressure, velocity, and flow rate measurements were recorded and analyzed. The data were compared to predicted flow conditions that had a possible relation to the distal flow field. The following are conclusions drawn from the observations:

A. The resulting pulsatile flow field that was produced distal to the jet could be treated as two separate systolic and diastolic, quasi steady state flows which compared favorably to steady flow predictions.

B. The systolic phase distal flow field best resembles a submerged flow as indicated by centerline velocity decay and apparent jet width growth; however, jet decay is moved downstream 2-4 diameters owing to the boundary interaction.

C. The pulse wave and jet characteristics are rapidly dissipated after systole. The jet shape does not persist beyond ten diameters downstream from the orifice. The pulsatile effects do persist, but the resulting profiles are flat and not indicative of oscillating flow.

D. The flow field was not fully turbulent nor laminar, but rather it is best described as "disturbed" throughout the entire cycle.

E. The frequency analysis showed significant variation between systole and diastole indicating that the vortex shedding frequency is subject to change over large pressure fluctuations; however, for small pressure fluctation, as during systole, no significant frequency variation occurred.

F. As the stenosis size decreases, the knee of the power spectral density function moves to higher frequencies as related by Strouhal number.

G. The pulsatile nature of the flow distal to the orifice does not allow the production of a fully developed turbulent flowfield as indicated by the absence of the -7 power spectral density decay slope for the systolic phases.

H. A method is proposed to predict orifice size and flow rate if the phonocardiagram recording taken at the point of maximum mumur intensity is available and the delta mean blood pressures are known. The development of this method would require further modeling with suitable blood analog fluids and geometrically accurate stenosis models. Also, the murmur frequency attenuation imposed by the body tissues is left for future analysis.

5.2 Recommendations for Further Study

To better develop a noninvasive stenosis size and blood flow rate prediction technique, stenosis shapes and blood analog fluid improvements should be made over those used in this work. A family of blockage shapes and sizes should be developed based upon a study of excised stenosis prototypes. The blockages simulated should provide small incremental changes between 80% and full occlusion. Data collection runs and frequency analyses, similar to those reported here, should then be developed to correlate pressure gradient/ flow rate relationships and Strouhal relationships to the observed velocity and phonocardiogram frequencies. The technique described here should be tested on potential stenosis or coarctation patients awaiting surgery and the results compared to any excised segments obtained at the time of surgery.

If this technique proves to be effective, then the approach should be extended to other fields of cardiovascular murmur analysis such as stenosed valves and septal defects.

REFERENCES

Abramovich, G. N. 1963. The theory of turbulent jets. M.I.T Press, Cambridge.

Akers, W. W., W. O'Bannon, C. Wm. Hall, and D. Liotta. 1966. Design and operation of a paracorporeal bypass pump. Trans. Am. Soc. for Artificial Int. Organs, v 12: 86-90.

Anderson, A. B. C. 1956. Vortex ring structure transition in a jet emitting discrete acoustic frequencies. J. Acoust. Soc. Amer. 28: 914-921.

Attinger, E. O., H. Sugawara, A. Navarro, and A. Anne'. 1966. Pulsatile flow patterns in distensible tubes. Circ. Res. V XVIII: 447-456.

Becker, H. A. and T. A. Massaro. 1963. Vortex evolution in a round jet. J. Fluid Mech. 31p3: 435-448.

Bendat, J. S. and A. G. Piersol. 1971. Random Data: Analysis and Measurement Procedures. Wiley - Interscience, New York.

Berguer, R., and N. H. C. Hwang. 1974. Critical arterial stenosis: A theoretical and experimental solution. Ann. Surg. 180, 1:39.

Blasius, H. 1913. Das Ahnlichkeitsgesetz bei Reibungsvorgange in lussigkeiten. Forschg. Arb. Ing. Wes. No. 131, Berlin.

Bradshaw, P. 1971. An Introduction to Turbulence and its Measurement. Pergamon Press, Oxford.

Brech, R. and B. J. Bellhouse. 1973. Flow in branching vessels. Cardiovasc. Res. 7: 593-600.

Bruns, D. L. 1959. A general theory of the causes of murmurs in the cardiovascular system. Amer. J. of Med. V27: 360-374.

Burns, D. L. 1964. The probable mechanism of the production of murmurs, in B. L. Sigal. The Theory and Practice of Auscultation. F. A. Davis, Co., Philadelphia.

Butterworth, J. S. and E. H. Reppert. 1966. Auscultation of the heart in J. W. Hurst and R. B. Logue. The Heart. McGraw-Hill, New York.

Clark, C. 1967. A local thermodilution flow meter for the measurement of venous blood flow in man. Med. Bio., Eng. 6: 133.

Corrsin, S. and M. S. Uberoi. 1949. Tech. Note No. 1865. N. A. C. A.

Crow, S. C. and F. H. Champagne. 1971. Orderly structure in jet turbulence. J. Fluid Mech. 48: 547-591

DeBakey, M. E. 1966. Surgical treatment of disease of the aorta and major arteries. In J. W. Hurst and R. B. Logue, The Heart. McGraw-Hill, New York.

Delman, A. J. 1967. Hemodynamic correlates of cardiovascular sounds. Ann. Rev. of Med. V18: 139-158.

Eliot, R. S. and J. E. Edwards. 1966. Pathology of congenital heart disease. In J. W. Hurst and R. B. Logue, The Heart. McGraw-Hill, New York.

Fruehan, C. T. 1962. On the aeolian theory of cardiovascular murmur generation. The New Physician, V11: 37-42.

Galambos. 1966. Vascular disease of the abdominal viscera. In J. W. Hurst and R. B. Logue, The Heart. McGraw-Hill, New York.

Hagen, G. 1839. Uber die bewegung des wassers in engen zylindrischen rohren. Pogg. Ann. V46: 423-442.

Herman, R. 1930. Experimentelle unterschungen zum wuderstabdsesetz des kreisrohes bei hohen reynoldsschen zahlen und groben anlauflangen. Diss. Leipzig, Akad. Veragsgesellschaft, Leipzig.

Hinze, J. O. 1959. Turbulence: an introduction to its mechanism and theory. McGraw-Hill, New York.

Hung, T. K. 1968. Vortices in Pulsatile Flaws. In proceedings of the Fifth International Congress on Rheology, October 7-11, Vol. 2.

Hussain, A. K. M. F. 1977. Mechanics of pulsatile flows in N. H. C. Hang and N. A. Norman. Cardiovascular Flow Dynamics and Measurements. University Park Press, Baltimore.

Hussain, A. K. M. F. and V. Ramjee. 1975. Vortex shedding from a circular cylinder in the presence of free steam disturbances. Proc. Fifth Canad. Congr. Appl. Mech.: 485-486.

Hussain, A. K. M. F. and V. Ramjee. 1976. Periodic wake behind a circular cylinder at low Reynolds numbers. Aero. Quart. 27: 123-142.

Hwang, N. H. C. and J. C. Chao. 1974. Applications of the Hydraulic Transmission Line Equations in Model Analogy of the Circulatory System. In D. Grisheta (ed.), Prospectives of Biomedical Engineering II. Madras, India.

Karnal, J. 1968. Coarctation of the aorta. Circ. Vols. XXXVII and XXXVIII, Supl. V.

Kline, J. L, J. L. Gimenez, and R. J. Maloney. 1962. Post-stenotic vascular dilation: confirmation of an old hypothesis by a new method. J. of Thoracic and Cardiovascular Surgery, V44: 738-748.

Kuchar, N. R. and S. Ostrach. 1966. Flows in the Entrance Regions of Circular Elastic Tubes. In ASME Biomedical Fluid Mechanics Symposium. Denver, Colorado.

Lauriden, P. 1968. Blood flow measurements by means of an electromagnetic flow meter during operation for coarctation of the aorta. Danish Med. Bull., V15, No. 7.

Lea, F. C. 1938. Hydraulics, Edward Arnold and Co., 6th Ed., p87.

Lighthill, M. J. 1972. Physiological fluid dynamics: a survey. J. Fluid Mech. 52: 475-497.

Lighthill, M. J. 1975. Mathematical Biofluid Dynamics. Society for Industrial and Applied Mathematics. Philadelphia.

Macagno, E. O. and T. K. Hung. 1967. Computational and experimental study of a captive annular eddy. J. Fluid. Mech. V28, pl: 43-64.

Maxworthy, T. 1972. The structure and stability of vortex rings. J. Fluid Mech. 51, pl: 15-32.

McDonald, D. A. 1974. Blood Flow in Arteries. Second edition. Williams and Wilkins, Baltimore.

Merrill, E. W. and A. Pelletier. 1967. Viscosity of human blood. Transition from Newtonian to non-Newtonian. J. Appl. Phys. 23,2:178.

Mills, R. D. 1968. J. Mech. Eng. Sci. V10, No. 2: 133-140.

Nikuradse, J. 1932. Gesetz mabigkeit der turbulenten strogmung in glatten rohren. Forsch. Arb. Ing. Wes. No. 356.

Nikuradse, J. 1933. Stromungsgesetze in rauhen rohen. Forsch. Arb. Ing. Wes. No. 361.

Noon, G. P. 1977. Flow-related problems in cardiovascular surgery. In N. H. C. Hwang and N. A. Norman, Cardiovascular Flow Dynamics and Measurements. University Park Press, Baltimore.

Nusselt, W. 1910. Warmeubergang in Ruhrleitungen. Forschg. Arb. Ing. Wes. 98, Berlin.

Olson, R. E. 1966. Etiology of coronary atherosclerosis. In J. W. Hurst and R. B. Logue, The Heart. McGraw-Hill, New York.

Onat, T. and E. Zeren. 1969. Coarctation of the abdominal aorta, review of 91 cases. Cardiologia 54: 140-157.

Poiseuille, J. 1840. Recherches experimentelles sur le mouvement des liquides dans les tubes de tres petits diameters. Computes Rendus V11: 961-1041.

Powell, A. 1964. The theory of vortex sound. J of Acoustical Soc. of Amer. Vol. 36, No. 1: 177-195.

Prandtl, L. 1926. Proc. second Int. Cong. Appl. Mech., Zurich: 62-75.

Prandtl, L. 1935. W. F. Durand, Aerodynamic theory. Vol. III: 142.

Reichardt, H. 1942. Vol. Forschungsh. 414.

Riemenschneider, T. A., G. C. Emmanouilides, F. Hirose, and L. M. Linde. 1969. Coarctation of the abdominal aorta in children: report of three cases and review of the literature. Pediatrics, V44, No. 5, Part 1. November 1969.

Roach, M. R. 1977. The effects of bifurcations and stenoses on arterial disease. In N. H. C. Hwang and N. A. Norman, Cardiovascular Flow Dynamics and Measurements. University Park Press, Baltimore.

Rockwell, D. O. and W. O. Niccolls. 1972. Natural breakdown of planar jets. Trans. of the ASME. J. of Basic Eng.: 720-730.

Rushmer, R. F. 1970. Cardiovascular Dynamics. Saunders, Philadelphia.

Schlant, R. S. 1966. Altered cardiac function in congenital heart disease. In J. W. Hurst and R. B. Logue, The Heart. McGraw-Hill, New York.

Schlichting, H. 1968. Boundary Layer Theory. McGraw-Hill, New York.

Schwartz, C. J. and J. R. A. Mitchell. 1962. Observations of localization of arterial plaques. Circ. Res. 11: 63-73.

Sexl, T. 1930. Uber den von E. G. Richardson entdeckten Annulareffekt Z. Phys. 61: 349.

Simpson, J. 1972. Personal conversations and case history reviews with surgical staff from Driscol Foundation Hospital, Corpus Christi, Texas.

Spencer, M. P., R. F. Johnston, A. B. Denison, Jr. 1958. Dynamics of the normal aorta: "inertia" and "compliance" of the arterial system which transforms the cardiac ejection pulse. Circ. Res., V VI, July 1958.

Stanton, T. E. 1911. The mechanical viscosity of fluids. Proc. Roy. Soc. London A85: 366.

Stokes, G. G. 1845. On the theories of internal friction of fluids in motion. Trans. Cambr. Phil. Soc. 8: 287-305.

Stokes, G. G. 1851. On the effect of the internal friction of fluids on the motion of pendulums. Camb. Phil. Trans. IX, V8. Math and Phys. Papers, V III: 1-141, Cambridge. 1901.

Symanski, F. 1932. Quelques solutions exactes des equations de l'hydrodynamique de fluide visqueux dans le cas d'un tube cylindrique. J. de Math. pures et appliquees, Series 9, Vol 11: 67.

Taylor, G. I. 1935. Statistical theory of turbulence proc. of the Royal Soc. of London. Series A. V151: 421.

Taylor, G. I. 1938. The spectrum of turbulence. Proc. of the Royal Soc. of London. Series A, V264: 476.

Tchen, C. M. 1953. On the spectrum of energy in turbulent shear flow. Res. paper RP 2388. J. Res. Nat. Bur. Standards, V50, No. 1: 51-62.

Tennekes, H. and J. L. Lumley. 1972. A First Course in Turbulence. Mi. I. T. Press, Cambridge.

Tuve, G. L. and R. E. Sprenkle. 1933. Orifice discharge coefficients for viscous liquids. Instruments, Vol. 6: 201.

Uchida, S. 1956. The pulsating viscous flow superposed on the steady laminar motion of incompressible fluid in a circular pipe. ZAMP, Vol. 7: 403-422.

Vennard, J. K. 1963. Elementry Fluid Mechanics. Fourth Edition. John Wiley and Sons. New York.

von Basch, S. 1904-5. Ehrfahrungen uber den venendruck des menschen. Arch. Biol. Navk., Vol 11, (Suppl.), 117.

White, F. M. 1974. Viscous Fluid Flow. McGraw-Hill, New York.

Wieting, D. W. 1966. Design and Evaluatoin of System Suitable for Analyzing Flow Behavior of Prostehtic Human Heart Valves. MS Thesis. University of Texas, Austin.

Womersley, J. R. 1955b. Method for calculation of velocity, rate of flow and viscous drag in arteries when the pressure gradient is known. J. Physiol. V127: 553-563.

Yellin, E. L. 1966. Hydraulic noise in submerged and bounded liquid jets. ASME Biomedical Fluid Mechanics Symposium, 1966: 209-221.